

# Stabilizing Deep Tomographic Reconstruction Networks

Weiwen Wu<sup>1,5</sup>, Dianlin Hu<sup>2</sup>, Wenxiang Cong<sup>1</sup>, Hongming Shan<sup>1,3</sup>, Shaoyu Wang<sup>4</sup>,  
Chuang Niu<sup>1</sup>, Pingkun Yan<sup>1</sup>, Hengyong Yu<sup>4,\*</sup>, Varut Vardhanabhuti<sup>5,\*</sup>, Ge Wang<sup>1,\*</sup>

<sup>1</sup>Biomedical Imaging Center, Center for Biotechnology and Interdisciplinary Studies,  
Department of Biomedical Engineering, Rensselaer Polytechnic Institute, Troy, NY,  
USA

<sup>2</sup>The Laboratory of Image Science and Technology, Southeast University, Nanjing, China

<sup>3</sup>Institute of Science and Technology for Brain-inspired Intelligence, Fudan University,  
Shanghai, China

<sup>4</sup>Department of Electrical & Computer Engineering, University of Massachusetts Lowell,  
Lowell, MA, USA

<sup>5</sup>Department of Diagnostic Radiology, Li Ka Shing Faculty of Medicine, The University  
of Hong Kong, Hong Kong SAR, China

**Abstract: Tomographic image reconstruction with deep learning (DL) is an emerging field of applied artificial intelligence, but a recent landmark study reveals that several deep reconstruction networks are unstable for computed tomography (CT) and magnetic resonance imaging (MRI). Specifically, three kinds of instabilities were identified: (1) strong output artefacts from tiny perturbation, (2) small features undetectable, and (3) increased input data damaging performance. On the other hand, sparsity-regularized reconstruction methods do not suffer these instabilities, due to kernel awareness. Since deep reconstruction is now a mainstream approach to achieve better tomographic image quality, stabilizing deep networks is an urgent challenge. Here we propose an Analytic Compressive Iterative Deep (ACID) framework to address this challenge. Instead of only using DL or compressed sensing, ACID consists of four modules: deep learning, compressed sensing-inspired sparsity promotion, analytic mapping, and iterative refinement. This paper shows the convergence and stability of ACID under a bounded error norm condition (a special case of the Lipschitz continuity), improves deep reconstruction quality by stabilizing an unstable deep reconstruction network in the ACID framework, and demonstrates the power of ACID in both stabilizing an unstable network and being resilient against adversarial attacks to the whole ACID workflow. In our experiments, ACID eliminated all three kinds of instabilities and significantly improved image quality in the context of the aforementioned study on the instabilities, demonstrating that data-driven reconstruction can be stabilized to outperform reconstruction using sparsity-regularized reconstruction alone. The mechanism of ACID is to synergize a deep reconstruction network trained on big data, compressed sensing-based improvement with kernel awareness, and iterative refinement to eliminate any data residual inconsistent with real data. We anticipate that this integrative closed-loop data-driven approach helps advance deep tomographic image reconstruction methods into clinical applications.**

## Introduction

There are about 100 million computed tomography (CT) scans and 40 million magnetic resonance imaging (MRI) scans performed yearly in the USA alone [1, 2]. In a well-known survey on medical innovations, over 200 leading experts scored on the relative importance of these innovations and voted that “*the most important innovation by a considerable margin is magnetic resonance imaging (MRI) and computed tomography (CT)*” [3]. Over the past several years, deep learning has attracted major attention. Since 2016, deep learning has been rapidly adapted for tomographic imaging, known as deep tomographic imaging [4-6]. Traditionally, tomographic reconstruction algorithms are either analytic (i.e., closed-form formulation) or iterative (i.e. based on statistical and/or sparsity models). More recently with deep tomographic imaging, reconstruction algorithms can be deep neural networks, which are data-driven [7]. This new brand of reconstruction algorithms has generated tremendous excitement and encouraging results in many studies. Some examples are included in a recent review article [6].

While many researchers are devoted to catching this new wave of tomographic imaging research, there are concerns on deep tomographic reconstruction as well, with the landmark paper by Antun *et al.* [8] as the primary example. Specifically, Antun *et al.* [8] performed a systematic study to reveal the instabilities of a number of representative deep tomographic reconstruction networks, including the AUTOMAP [9]. Their study demonstrates three kinds of network-based reconstruction vulnerabilities. (1) Tiny perturbation on input resulting in strong output artefacts (potentially, false positivity); (2) small structural features going undetected (false negativity): The study found that small structural changes, for example, a small tumor, may not be captured in the images reconstructed by the deep neural networks, even though standard sparsity-regularized methods can capture it. It is worth noting that the issue of missing tiny details, e.g. pathologies, was one of the main concerns raised by radiologists in the Fast MRI challenge in 2019 [10]; and (3) increased input data leading to decreased imaging performance. These critical findings are serious warnings and at the same time present great opportunities for deep tomographic imaging research.

From a historical perspective, a debate, challenge, or crisis always inspires theoretical and methodological development, especially so during a paradigm shift. In the case of tomographic imaging, there are several such examples. For analytic reconstruction, there was a critique that given a finite number of measurements, the tomographic reconstruction is not uniquely determined, meaning that ghost structures can be reconstructed that do not show in reality but are consistent with measured data [11]. Then, this problem was addressed by regularization, such as enforcing the band-limitedness of underlying signals [12]. When iterative reconstruction algorithms were initially developed, it was observed that a reconstructed image was strongly influenced by the penalty term; in other words, what you obtain could be what you want to see [13]. After selecting appropriate regularization terms and fine-tuning hyper-parameters, the benefits of iterative algorithms outweigh the potential shortcomings. Hence, such algorithms were made into commercial scanners [11, 14]. As far as compressed sensing is concerned, the validity of results assumes restricted isometry or robust null space properties. A sparse solution may not

always be correct. However, in reality, it works “*with an overwhelming probability*” [15]. In practice, the sparsity constraint can be either too strong, smearing features, or too weak, admitting artifacts. For example, a tumor-like structure is introduced, or pathological vessels might be filtered out if total variation is overly minimized [16]. Despite the aforementioned limitations, multiple sparsity-promoting reconstruction algorithms were implemented on commercial scanners due to their excellent performance.

Now, we are facing a similar situation, where emerging deep tomographic imaging methods in some published forms encounter challenges, as reported in [8]. In addition to extensive numerical and experimental data showing the instabilities of several deep reconstruction networks, the authors of [8] pointed out that these instabilities are fundamentally associated with the lack of “*kernel awareness*” [17] and are “*nontrivial to overcome*” [8]. On the other hand, compressed sensing inspired reconstruction algorithms worked stably in their experiments under the same conditions [8], since compressed sensing based algorithms use sparse regularization which has “*at its heart a notion of kernel awareness*” [17].

This article focuses on the feasibility and principle that deep reconstruction networks can be stabilized in a hybrid model, allowing it to be superior to compressed sensing based reconstruction. To overcome the instabilities of the deep reconstruction networks selected in [8], here we propose an Analytic Compressive Iterative Deep (ACID) framework shown in Figure 1(a). Given a deep reconstruction network  $\Phi$  and measurement data  $\mathbf{p}^{(0)}$ , an image can first be reconstructed but it may compromise fine details and introduce artifacts. Second, a compressed sensing inspired module  $\Theta$  is used to enforce sparsity in the image domain [18, 19], with the loss function covering both data fidelity and sparsity (such as total variation [20], low-rank [21], dictionary learning [22], *etc.*). Third, the forward imaging model projects an intermediately reconstructed image to the raw data domain to estimate tomographic data, which generally differ from the original data  $\mathbf{p}^{(0)}$ . The discrepancy is a data residual that cannot be explained by the current image. From this data residual, an incremental image is reconstructed with the module  $\Phi$  to update the current image through the module  $\Theta$ . This process can be repeated to prevent losing or falsifying features. In summary, ACID consists of three key modules: deep reconstruction for data-driven priors (namely, “deep”), compressed sensing inspired sparsity promotion (briefly, “compressive”), and analytic mapping to estimate data (i.e., “analytic”). This iterative workflow cycling through these three modules represents a meta-iterative scheme and targets a feasible solution in the intersection of the space of data-driven solutions, the space of sparse solutions, and the space of solutions subject to data constraints, as illustrated in Figure 1(b). In this way, ACID would give a better solution than the sparsity-regularized reconstruction; for details, see the Methods section.

An important question is if the ACID network will converge to a desirable solution in the above-described intersection of the three spaces (Fig. 1(b)). First of all, a deep learning network represents a non-convex optimization problem, which remains an open problem in general; see more details in the latest review [23]. The non-convex optimization problem in a general setting is of non-deterministic polynomial-time hardness (NP-hardness). To solve such a problem with guaranteed convergence, practical assumptions must be made in almost all cases. These assumptions include changing a nonconvex formulation into a

convex one under certain conditions, leveraging problem-specific structure, or only seeking a local optimal solution. Specifically, the Polyak–Łojasiewicz condition and the Lipschitz continuity are two typical conditions used to ease nonconvex optimization tasks; for example, see [24, 25].

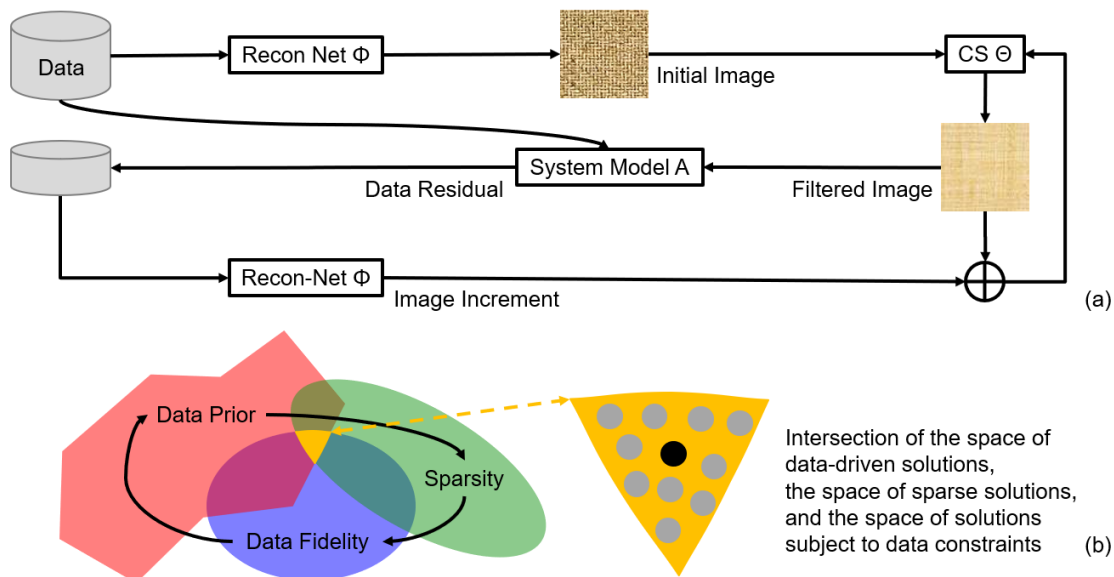


**Figure 1. ACID architecture for stabilizing deep tomographic image reconstruction.** Initially, the measurement data  $\mathbf{p}^{(0)}$  is reconstructed by the reconstruction network  $\Phi$ . The current image is sparsified by the CS-inspired sparsity promotion module  $\Theta$  (briefly, CS module). Tomographic data are then computed based on the sparsified image according to the system model  $A$ , and compared to the measurement data  $\mathbf{p}^{(0)}$  to find residual data. The residual data is processed by the modules  $\Phi$  and  $\Theta$  to update the current image.

Given the status of the non-convex optimization field, to justify our heuristically designed ACID system in terms of its convergence, we assume that a well-designed and well-trained network, referred to as a “proper” network, satisfies a bounded error norm (BEN) property, which is a special case of the Lipschitz continuity; see the **Methods** section and Supplementary Information (**SI**) for details. Importantly, assuming the BEN property of a deep reconstruction network, the convergence of the ACID is guaranteed; again see the **Methods** section and **SI** for details. Note that, in a recent paper [26] a two-step deep learning strategy was analyzed for tomographic imaging, where a classical method is followed by a deep-network-based refinement to “close the gap between practice and theory” for this particular reconstruction workflow. The key idea is to use the null space network for data-driven regularization, achieving convergence also based on the Lipschitz smoothness. It is underlined that our analysis of the convergence of ACID is in the same spirit.

While the details are in the **SI**, here we outline the key idea of our analysis on the convergence of the ACID iterative workflow. In reference to Figure 1, we assume the BEN property of a proper reconstruction network, as characterized by the ratio being less than 1 between the norm of the reconstruction error and the norm of the corresponding ground

truth; that is, the error component of the initial image reconstructed by the deep network  $\Phi$  is less than the ground truth image in the  $L_2$  norm sense. This error consists of two components: sparse and non-sparse. The non-sparse component is then effectively suppressed by the CS inspired sparsity promotion module  $\Theta$ . The sparse errors are either observable or unobservable. The un-observable error is in the null space of the system matrix  $A$ , and should be small relative to the null space component of the ground truth image because a proper reconstruction network is intended to recover the null space component well in the data-driven fashion. ACID can eliminate the observable error iteratively, thanks to the BEN property. Specifically, the output of the module  $\Theta$  is re-projected by the system matrix  $A$ , and then the estimated data are compared with the measured data. The difference is the data residual due to the observable error component. To suppress this error component, we use the network  $\Phi$  to reconstruct an incremental image and update the current image with the module  $\Theta$ . In this correction step, the desirable incremental image is the new ground truth image, and the BEN property holds to make sure that this step is a contraction mapping; in other words, the associated new observable error is less than the previous observable error, thanks to the BEN property. Repeating this process many times, the observable error component will diminish geometrically (the ratio less than 1), so that the ACID solution will simultaneously incorporate data-driven knowledge, sparsity preference, and measurement data consistency. This verbal explanation will be mathematically clarified in the **SI**.

## Results

Given the importance of the recent study on instabilities of some representative deep reconstruction networks [8], the main motivation of our work was to stabilize deep tomographic reconstruction. Hence, our experimental setup systematically mirrored what was described in [8], including datasets and their names, selected reconstruction networks, compressed sensing-based minimization benchmarks, and image quality metrics. As a result, the Ell-50 and DAGAN were picked up for CT and MRI (details in the **Methods** section and **SI**), which were subjected to the instabilities found in [8]. Then, beyond the genuine systematic comparison, we also performed an ablation study on ACID and investigated its own stability in the cases of adversarial attacks. For more details, please refer to the **SI** and the relevant parts in [8]. The detailed explanation of the original cases of C1-C6 and M1-M12 are in **SI**. Furthermore, the source codes, trained networks, test datasets and reconstruction results can be found on Zenodo (<https://zenodo.org/record/4540511>).

### (1) Stability with Small Structural Changes

We first demonstrated the robust performance of the ACID network with small structural changes. The Ell-50 was employed, as a specified FBPCovNet [27]. Fig. 2 shows representative results in two CT cases; i.e., C1 and C2 (details in **SI**). To examine the degrees of small image structure recovery allowed by all reconstruction methods, some words, a bird, and their mixture were used to simulate the structural changes in CT images. It can be observed in Fig. 2a-h that the proposed ACID provides a superior performance thanks to the synergistic fusion of deep learning, compressed sensing, and refinement iteration. In this case, the Ell-50 served as the deep network for data-driven image

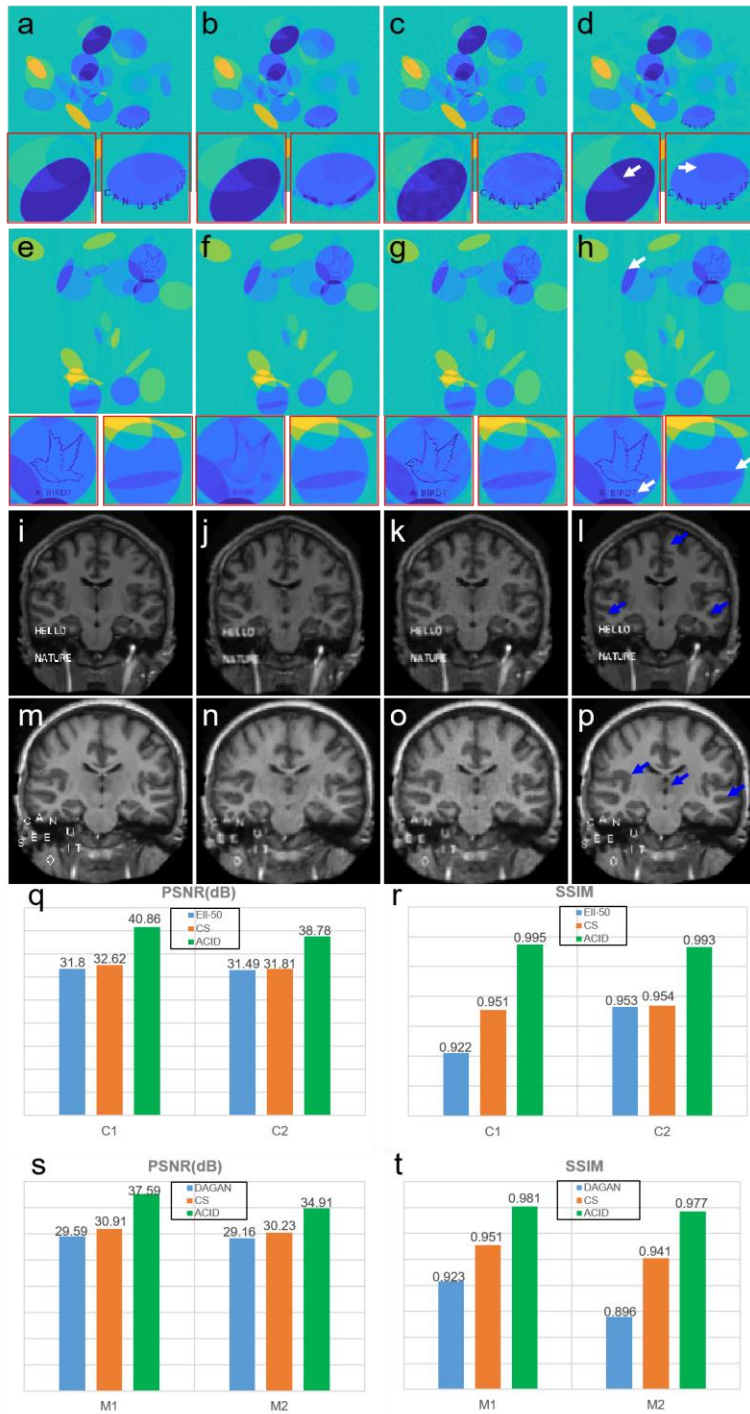


**Figure 2. Performance of ACID with small structural changes in the CT and MRI cases.** Four phantoms with structural changes are reconstructed by ACID and competing techniques; **a**, **e**, **i** and **m** are the original images. **b** and **f**, **j** and **n** are the results with EII-50 and DAGAN for CT and MRI respectively; **c**, **g**, **k** and **o** are the corresponding CS results; **d**, **h**, **l** and **p** are the ACID counterparts. For CT, the dataset contains 50 projections. For MRI, the subsampling rate is 10%. The quantitative results are in **q-r** and **s-t** for CT and MRI respectively. The windows for C1 and C2 are  $[-150\ 150]$ HU and  $[-200\ 200]$ HU, respectively, and M1 and M2 results are normalized to  $[0\ 1]$ .

estimation. It was observed in Fig. 2a-h that compressed sensing inspired reconstructions can give better results than the Ell-50 network. This was consistent with the results reported in [8]. Because the compressed sensing-based method performed conventional unsupervised, model-based and sparsified reconstruction, structural changes were within the sparsity constraint and were kept in the reconstruction. However, we cannot clearly see the text and the bird in the Ell-50 results, while the compromised versions of the text and the bird were still identifiable with the compressed sensing method. In contrast, the text “CAN U SEE IT” and the bird were well recovered using our ACID network, while the contour of the bird can be identified in the CS reconstructions among the artifacts due to the under-sampled data [28]. In terms of image edge preservation, the Ell-50 reconstruction contains clearer edges than those in the CS reconstruction. Compared to the Ell-50 prediction, ACID corrected structural distortion by avoiding the projection distortion via iterative refinement. This point is evidenced by the structure indicated by the white arrow in Fig. 2a-h.

After testing ACID with CT data, a similar study was performed on MRI with small structural changes, as shown in Fig. 2i-p. DAGAN [29] chosen as one representative network in [8] was implemented (more details in **SI**). The symbols were added to brain MRI slices (details about M1 and M2 are in **SI**). Figure 2i-l are the M1 results reconstructed from data subsampled at a rate of 10%. It can be seen that the phrase “HELLO NATURE” was severely corrupted by DAGAN, which makes it difficult to recognize the structures. The structures were effectively recovered by the CS method but there are still artifacts due to the low subsampling rate. In addition, the edges of “HELLO NATURE” were severely blurred and difficult to read. On the other hand, our ACID network produced excellent results with clearly visible texts. To further show the power of ACID with small structural changes, another example (M2) in [8] was also reproduced as Fig. 2m-p. The text “CAN U SEE IT” was corrupted by both DAGAN and CS, rendering the insert hard to be read. Again, the text was easily seen in the reconstruction by ACID. Indeed, compared with the DAGAN and CS results, the ACID reconstruction keeps sharp image edges and subtle features of the text. The reconstructed results from M2 (similar to the DAGAN results in [8] but with a different subsampling rate and sampling pattern) further confirm the superior performance of ACID.

In brief, ACID exhibited superior stability with structural changes over the competitors, as quantified by the two metrics including the peak image signal-to-noise ratio (PSNR), and structural similarity (SSIM) (Fig. 2q-t). In all these results, ACID always obtained the greatest PSNR and the highest SSIM.

## **(2) Stability against Adversarial Attacks**

It was pointed out that a tiny perturbation can fool a deep neural network to make a highly undesirable prediction [8]. To show the capability of the ACID approach against adversarial perturbations, the CT (cases C3 and C4) and MRI (cases M3 and M4) reconstruction results are given in Fig. 3. As far as the CT results are concerned, in Fig. 3a-d, the edges obtained using Ell-50 indicated by the arrows were distorted by perturbation. Although the CS reconstruction had a stable performance against tiny perturbations, these distortions could not be fully corrected in the corresponding results due to the subsampling

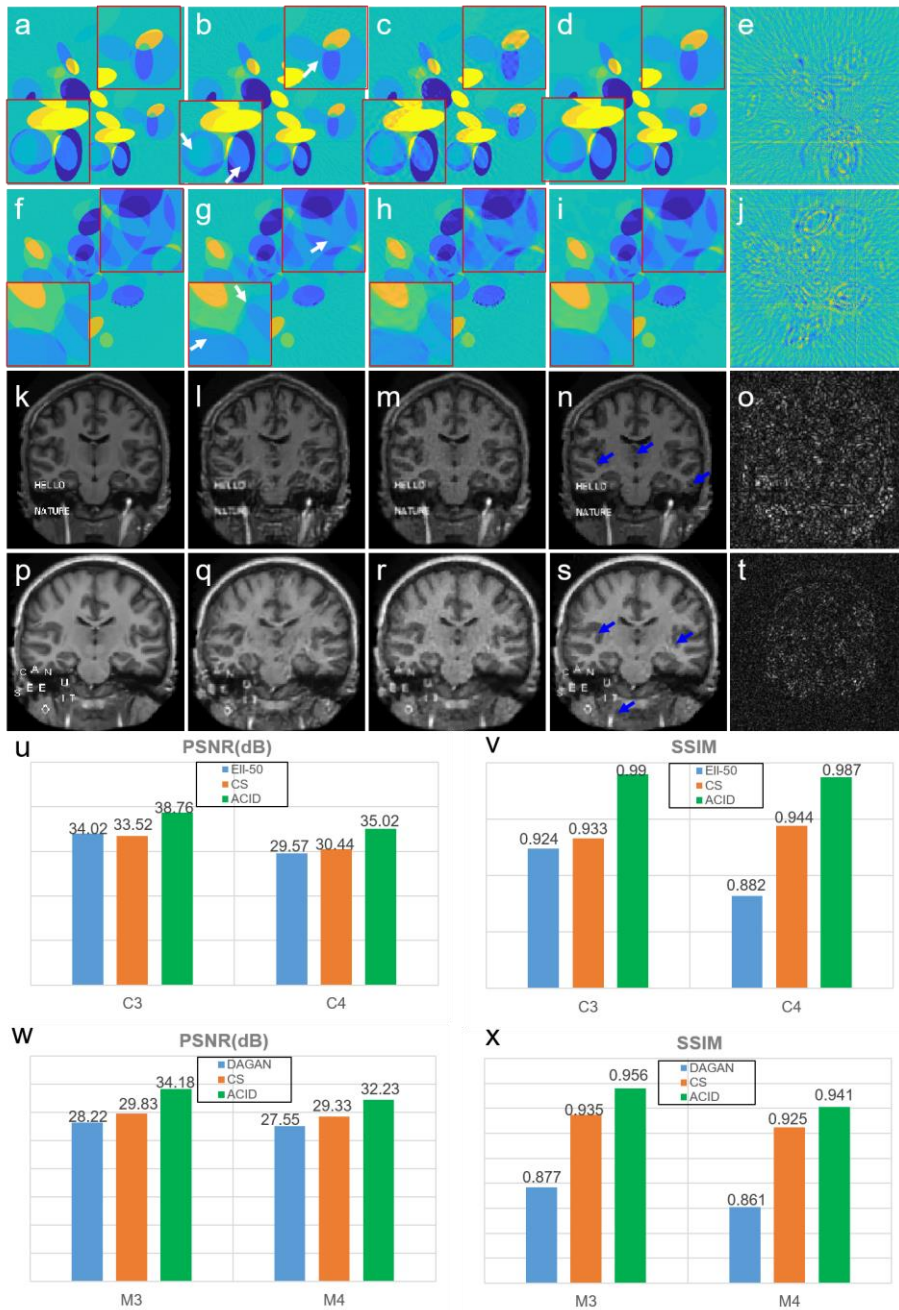


**Figure 3. Performance of ACID against adversarial attacks coupled with structural changes in the CT and MRI cases.** **a, f, k, and p** are the perturbed original images. **a, b, c and d** are the ground truth image, Ell-50, CS and ACID reconstructions in the C3 case (window [-80 80]HU); **f, g, h and i** are the counterparts in the C4 case (window [-150 150]HU); **k, l, m and n** are the ground truth image, DAGAN, CS and ACID reconstructions in the M3 case (normalized to [0, 1]); **p, q, r and s** are the counterparts in the M4 case (also normalized to [0 1]); and **e, j, o and t** show the adversarial samples. The quantitative CT and MRI results are in **u-v** and **w-x**. The display window for **e** and **j** is [-5 5]HU, and that for **o** and **t** is [-0.05 0.05].

artefacts. However, this defect was well corrected by ACID. It was observed in Fig. 3f-i that the artifacts marked by the arrows induced by perturbation destroy the image edges in

the Ell-50 reconstruction. This potentially results in a wrong clinical interpretation in practice. Although such artefacts were eliminated in the CS reconstruction, the artifacts from subsampling were clearly introduced. In contrast, the corresponding edges and shapes were reproduced by ACID without any significant artefacts. In addition, the text “CAN YOU SEE IT” was completely lost in the Ell-50 reconstruction, and severe artifacts were induced by the CS method. In contrast, our ACID results preserved the edges and letters faithfully. Regarding the MRI results, the worst predictions from tiny perturbations were evident in Fig. 3l and q. Clearly, DAGAN failed upon adversarial attacks. Compared with DAGAN, the CS-based reconstruction provided higher accuracy but still failed to preserve all the details such as edges from subsampled data, as shown in Fig. 3m and r. On the other hand, our ACID network worked without these weaknesses. To quantify the superiority of ACID, the image quality metrics were included in Fig. 3u-v and w-x, showing that ACID achieved the best performance.

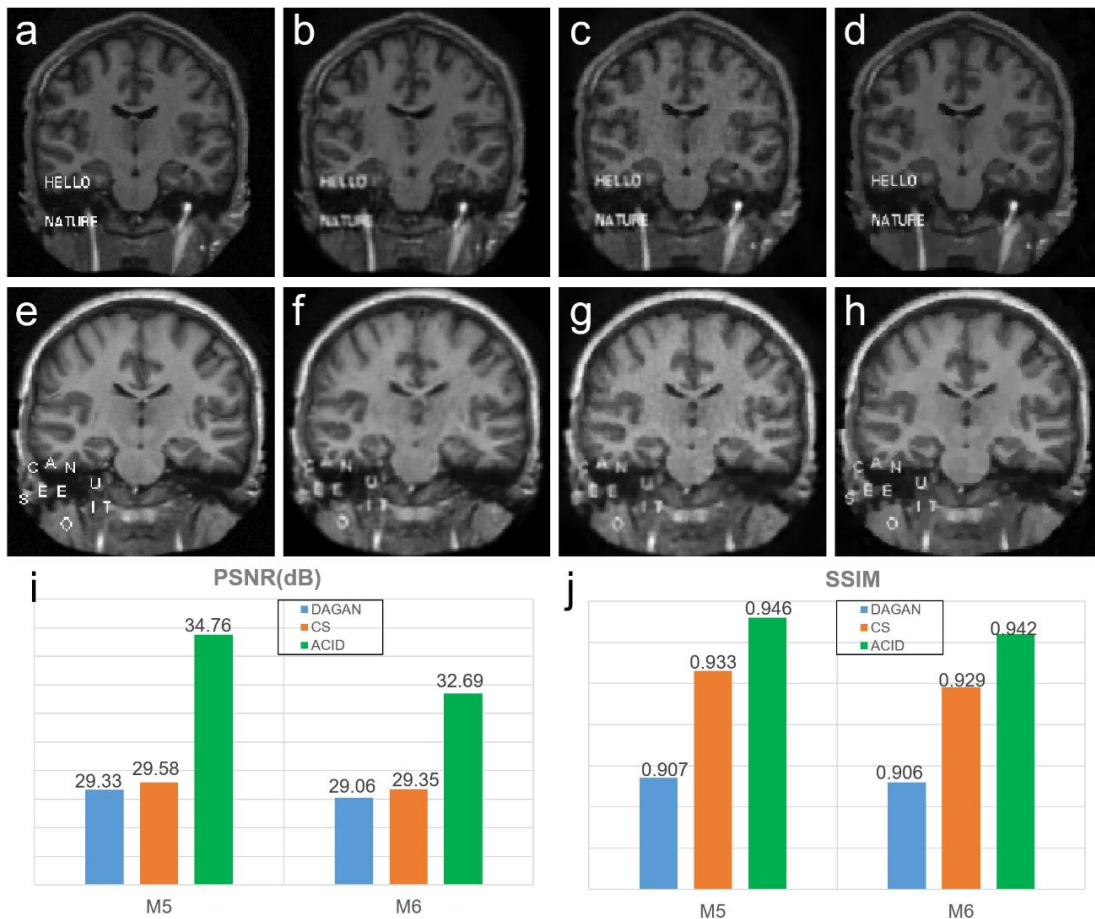


**Figure 4. Quantitative results in the M5 and M6 cases in terms of SSIM and PSNR. a-d and e-h** represent the ground truth, DAGAN, CS and ACID results on M5 and M6 respectively. **i and j** give the PSNR and SSIM results on M5 and M6 respectively.

The reconstruction results were also obtained in the M5 and M6 cases, generated by adding random noise to M1 and M2. In this situation, the performance of all the methods

was corrupted by noise. With DAGAN and CS, the image edges and other features were notably further blurred. In contrast, all the features including the embedded words were nicely and consistently recovered by ACID; see Fig. 4. It was observed that ACID provided better quantitative results than the competitors. Specifically, ACID suppressed elevated image noise more effectively than the CS-based reconstruction method, even if the network had not been trained on the noisy datasets.

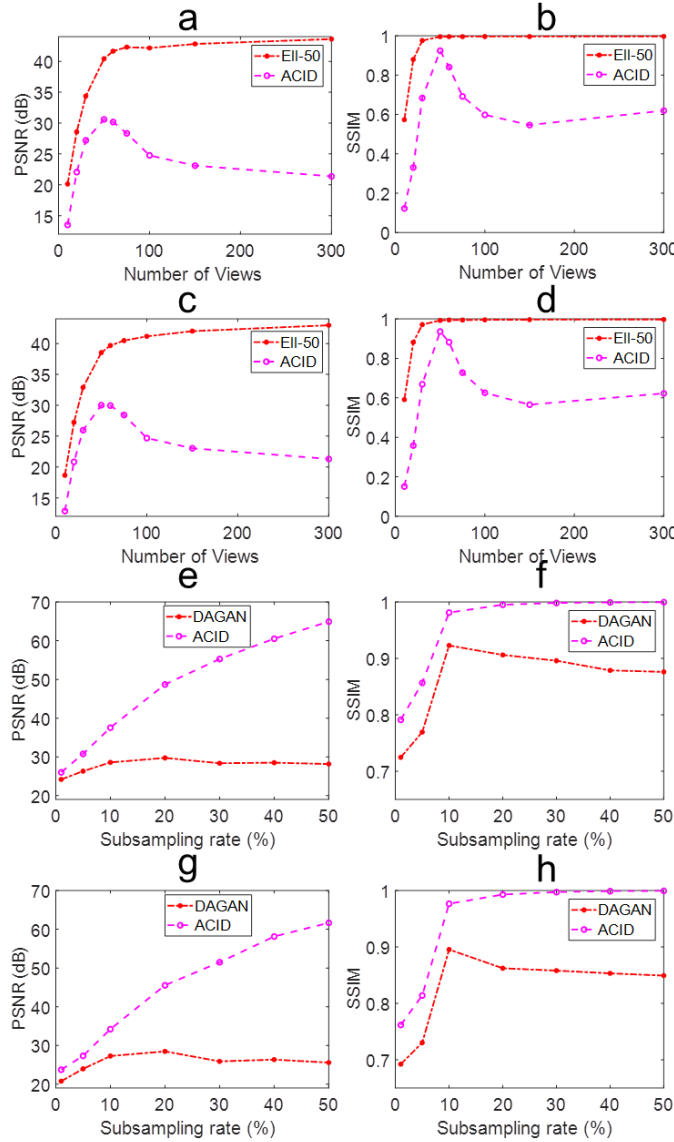


**Figure 5. Performance of ACID with more input data.** a-b and c-d plot the PSNR and SSIM curves with respect to the number of views in Cases C1 and C2, respectively; e-f and g-h are similar curves with respect to different subsampling rates in Cases M1 and M2, respectively.

### (3) Stability for More Input Data

The performance of ACID increased monotonically as more input data were made available, which was certainly expected of a well-designed reconstruction scheme. With

Ell-50 and DAGAN as examples, it was pointed out in [8] that the performance of deep reconstruction networks was degraded with more input data, which is counter-intuitive and highly undesirable. To evaluate the performance of ACID with more input data, Cases C1 and C2, M1 and M2 were analyzed. The number of views in the CT case was set to 10, 20, 30, 50, 60, 75, 100, 150 and 300, and in the MRI case the subsampling rate set to 1%, 5%, 10%, 20%, 30%, 40% and 50% respectively. It was observed in Fig. 5 that the performances of Ell-50 was compromised with more projections, being consistent with the observation in [8]. In contrast, ACID performed better with more views in terms of PSNR and SSIM. Similarly, the performance of DAGAN was decreased at sampling rates higher than that used for training DAGAN, which was the same conclusion on DAGAN reported in [8], and ACID produced better reconstruction quality in terms of PSNR and SSIM. It was easily seen in Fig. 5e-h that the performance of ACID was substantially improved with more input data. This indicated that our ACID generalized well to use more data, similar to compressed sensing methods.

#### **(4) Ablation Study on ACID**

ACID involves deep reconstruction, compressed sensing, analytic mapping, and iterative refinement. To understand the synergistic interactions of these algorithmic ingredients, we evaluated their relative contributions to the image quality. Specifically, we obtained the results reconstructed using three simplified versions of ACID by removing/replacing individual key components. Specifically, these three versions were obtained by only improving the initial deep reconstruction with compressed sensing without iteration, replacing deep reconstruction with a conventional reconstruction method, and abandoning the compressed sensing constraint, respectively. Fig. 6 demonstrated that each simplified ACID variant compromises the ACID performance significantly.

#### **(5) Comparison with Classic Iteration Networks**

The use of deep learning as a post-processor or an image-domain data-driven regularizer in a classic iterative reconstruction algorithm, as we suggested in [4], is inferior to ACID, because the classic iterative reconstruction cannot take full advantages of data-driven prior, even if a deep learning image denoiser is used, such as in ADMM-net [30]. Different from other iteration-unrolled reconstruction networks that only use deep learning to refine an intermediate image already reconstructed using a classic iterative algorithm, ACID reconstructs an intermediate image using a deep network trained on big data. To highlight the merits of ACID, the classic ADMM-net was chosen for comparison [30]. The ADMM-net was trained on 20% subsampled data, with a radial sampling mask while the other settings being the same as that in [30]. It was observed in Fig. 7a-c that ACID achieved the best reconstructed image quality, followed by ADMM and DAGAN. With DAGAN, the phrase “HELLO NATURE” was still blurred, and it became clearer in the ADMM-net reconstruction. Unfortunately, the artefacts due to subsampling remain evident. In Fig. 8d-f, there were strong artifacts in the reconstructed image by DAGAN. On the other hand, the ADMM-net image quality, such as edge sharpness, was better DAGAN. The image edges and features were the best with the ACID results in Fig. 7. To qualify the performance of these techniques, the PSNR and SSIM measures were computed, as shown in Fig. 7g-h.

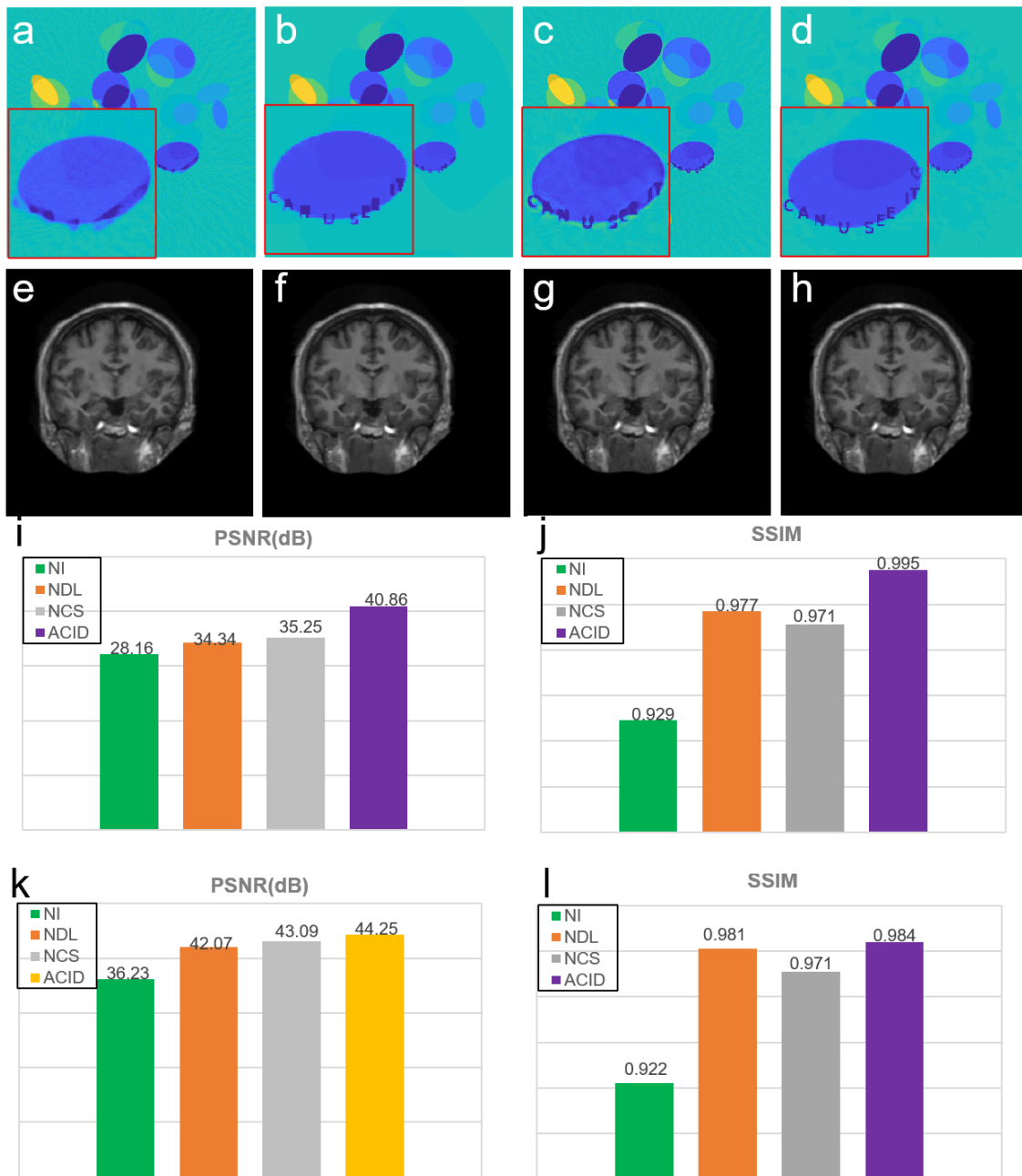


**Figure 6. ACID ablation study in terms of visual inspection and quantitative metrics in the C1 and M7 cases, where NI denotes the reconstructed results by ACID without further iterations (K=1). NDL and NCS denote ACID without deeply learned prior and compressed sensing-based improvement respectively. a-d represent the reconstructed results by NI, NDL, NCS and ACID in the C1 case. e-h are the reconstructed results by NI, NDL, NCS and ACID in the M7 case. i-l are the PSNR and SSIM results in these cases respectively.**

The ACID flowchart can be unfolded into the feedforward architecture. However, such an unfolded reconstruction network was still subject to adversarial attacks, similar to MRI-VN [31] in [8], *etc.*, since there was no kernel awareness from a compressed sensing

module. Given the current GPU memory limit, it was not practical to unfold the whole ACID (up to 100 iterations or more) into a single network.

There were at least three differences between ACID and the unrolled reconstruction networks. First, large-scale trained networks, such as DAGAN [29] and Ell-50 [27], could be incorporated into the ACID framework as we have demonstrated in this study. However, only small sub-networks could be used as basic units to unroll the iterative ACID procedure; *i.e.*, an unrolled ACID network could only use relatively light networks as building blocks such as 3Layer-CNNs [32]. Second, the size of reconstructed images in the unrolled networks was usually very small, and the resolution was low. For example, the input image size was only 256x256 pixels for ADMM-net [30], LEARN [32], and AirNet [33], limited by the memory size of GPU. The reconstructed low resolution results could not satisfy the requirement of clinical applications, especially in CT imaging tasks. Third, the unrolled networks were commonly designed for 2D imaging geometry, and they were difficult to be employed in 3D imaging geometry. More importantly, it was impractical to incorporate the theoretically-grounded sparsity regularization module in such an unrolled architecture, since the derivative and other needed operations (for example, the image gradient  $L_0$ -norm [34]) could not be effectively implemented with compact feed-forward networks which demanded big data and could not be easily trained.

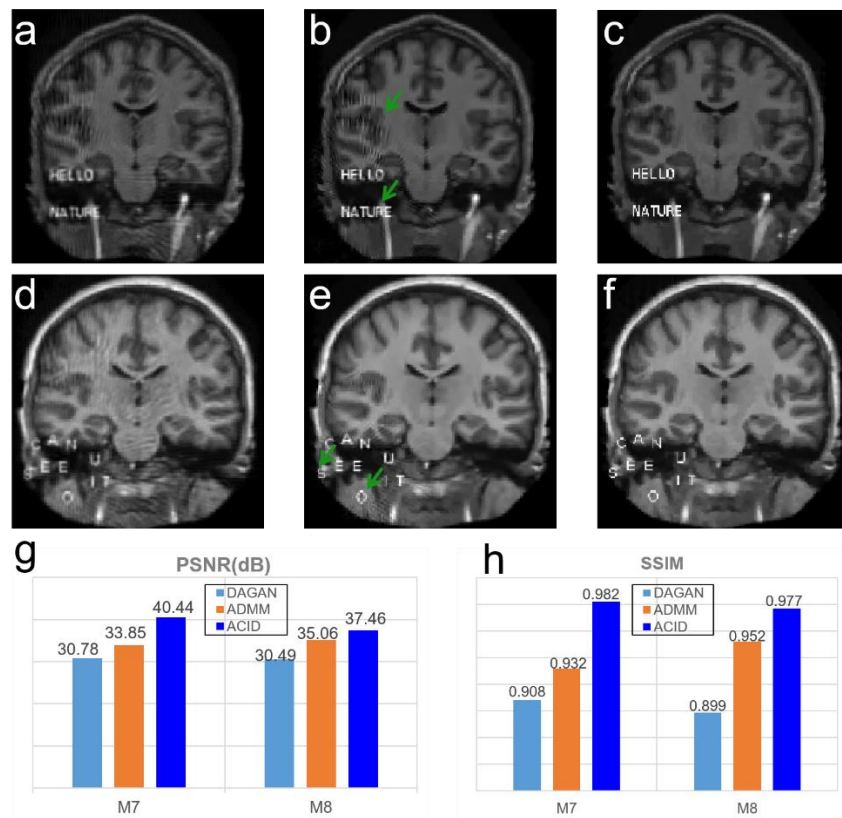


**Figure 7. Comparison of reconstruction performance relative to the ADMM-net. a-c and d-f represent the results reconstructed by DAGAN, ADMM-net and ACID. g-h show the quantitative results in the M8 and M9 cases in terms of PSNR and SSIM.**

## (6) Adversarial Attacks to the ACID System

As demonstrated above, ACID stabilizes an unstable network successfully. Then, a natural question is if the ACID system itself is stable or unstable? To evaluate the stability of ACID in its entirety, we generated adversarial samples to attack the entire ACID workflow, with representative results in Fig. 8. Because ACID involves both deep reconstruction and sparsity minimization in the iterative framework, the adversarial attack mechanism is more complicated for ACID than that for a feed-forward neural network. Please see our **SI** for details on the equivalent adversarial method we used to attack ACID. Using this adversarial attacking method, C5, C6, M10-M12 images were perturbed to various degrees, being even greater than that used in the single neural network against adversarial attack cases in terms of the  $L_2$ -norm. Our ACID reconstruction results showed that the inserted texts were still clearly observable in the ACID reconstructions, and the structure and edges were not significantly corrupted. Consistently, after the adversarial attacks, our ACID still produced decent quantitative results in terms of PSNR and SSIM.

## Discussions and Conclusion

The “*kernel awareness*” [17] is important to avoid the so-called “*cardinal sin*”. Suppose that two images  $f$  and  $f'$  correspond to two datasets  $Af$  and  $Af'$  respectively, if the datasets are very close to each other while the corresponding images significantly differ and yet these images are accurately reconstructed using a continuous algorithm, then the algorithm will be intrinsically vulnerable, suffering from false-positive and false-negative errors; for mathematical rigor, please see Theorem 3.1 in [17]. For this reason, the deep tomographic networks were successfully attacked in [8]. On the other hand, sparsity-promoting algorithms were designed with kernel awareness, leading to accurate and stable recovery of underlying images, as also shown in [8]. As demonstrated by our work, in addition to leveraging data-driven priors, the kernel awareness has been embedded in the ACID network through both the compressed sensing-based sparsity constraint and the iterative refinement so that ACID has a robust performance against noise, under adversarial attacks, and when input data are increased relative to what was assumed in the network training.

It is important to understand how a compressed sensing-based image recovery algorithm implements the kernel awareness. Basically, the sparsity-constrained solution is iteratively obtained so that the search for the solution is within a low-dimensional manifold. That is, prior knowledge known as sparsity helps narrow down the solution space. Indeed, natural and medical images allow low-dimensional manifold representations [35]. It is critical to emphasize that a deep neural network is data-driven, and the resultant data-driven prior is rather powerful to constrain the solution space further for tomographic imaging. While sparsity prior is just one or a few mathematical expressions, deep prior is in a network format and extracted from big data. These two kinds of priors are actually combined in our ACID network to have the merits from both sides, and we have fundamental reasons to expect that ACID or similar networks would output classic algorithms including CS-inspired sparsity-promoting methods. Indeed, with a deep reconstruction capability, ACID outperforms the state-of-the-art CS-based method for image reconstruction, including dictionary learning reconstruction methods (details in **SI**).

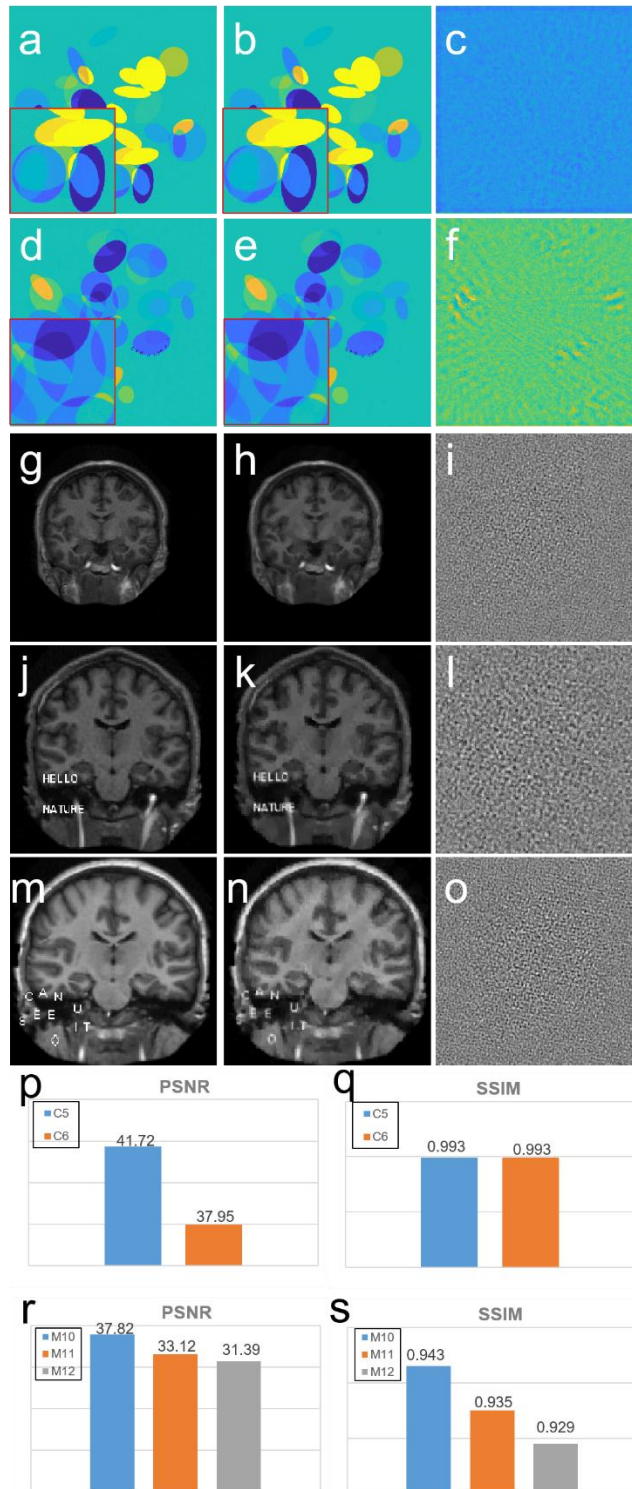


**Figure 8. ACID being resilient against adversarial attacks.** a-c, d-f, g-i, j-l and m-o are ACID results in C5, C6, and M10-12 cases. The 1<sup>st</sup> -3<sup>rd</sup> columns represent the ground truth plus tiny perturbation, reconstructed images, and corresponding perturbations. p-q and r-s show the quantitative results in the C5, C6, and M10-12 cases in terms of PSNR and SSIM.

Unlike the establishment of the instabilities, a number of positive experimental results are not sufficient to claim the general applicability of ACID, and a theoretical analysis is needed on the convergence of ACID. In this regard, we have assumed the BEN property of the reconstruction network, which is a special case of the Lipschitz continuity that is widely used in the field of non-convex optimization to establish various converging properties [24, 25]. As a result, the convergence of ACID is established, as long as the relative error is under a reasonable control.

In conclusion, our ACID network synergizes key elements of deep reconstruction, CS-based sparsity regularization, analytic mapping, and iterative refinement, and as such have systematically fixed the instabilities of the deep reconstruction networks selected in [8] and consistently produced better results than the state-of-the-art CS-based algorithms used in [8]. Furthermore, based on an assumed Lipschitz property, referred to as BEN, of the reconstruction network, the converging behavior and solution characteristics of ACID have been described. It is emphasized that ACID is only an example, and other deep reconstruction networks of this type can be developed for different tasks, and accelerated for fast turnaround time. There are other good strategies as well to stabilize and optimize deep tomographic networks [36, 37]. Since adversarial attack and proactive defense is just like the arms race, the research of this type will stimulate development of deep reconstruction networks for tomographic medical imaging.

## Methods

### (1) Interpretation of the ACID Scheme by Minimizing an Overall Objective Function

Here we interpret our proposed ACID iterative algorithm by casting it as the iterative solution that minimizes an overall objective function. This formulation will help improve our understanding of our initially heuristically-derived ACID scheme. It is underlined that given the nonconvex nature of this complicated optimization problem, a closed-form solution is impossible, approximations are appropriate to derive computationally efficient iterative formulas, and the errors due to the approximations will be suppressed via ACID iterations so that the ACID algorithm will converge to a desirable solution in the intersection of the space constrained by measured data, the space of sparse solutions, and the space of deep priors.

In the imaging field, we often assume that the measurement  $\mathbf{p}^{(0)} = \mathbf{A}\mathbf{f}^* + \mathbf{e}$ , where  $\mathbf{A} \in \mathbb{R}^{m \times N}$  is a measurement matrix (for example,  $\mathbf{A}$  is the Radon transform for CT [38] and the Fourier transform for MRI [39]),  $\mathbf{p}^{(0)} \in \mathbb{R}^m$  is an original dataset,  $\mathbf{f}^* \in \mathbb{R}^m$  is the ground truth image,  $\mathbf{e} \in \mathbb{R}^m$  is data noise,  $\|\mathbf{e}\|_2 \leq \eta$  for some  $\eta \geq 0$ , and most relevantly  $m < N$ , meaning that the inverse problem is underdetermined. In the under-deterministic case, additional prior knowledge must be introduced to uniquely and stably recover the original image. Without loss of generality, we assume that  $\mathbf{H} \in \mathbb{R}^{N \times N}$  is unitary,  $\mathbf{H}^*$  is the adjoint of  $\mathbf{H}$ , and  $\mathbf{H}^*$  is equal to the inverse of  $\mathbf{H}$ .  $\mathbf{A}$  satisfies the RIP of order  $s$ , and  $\mathbf{H}\mathbf{f}^*$  is  $s$ -sparse. We further assume that the function  $\Phi(\cdot)$  models a well-trained neural network, and it continuously maps measurement data to an image. Although  $\Phi(\cdot)$  is to solve the problem  $\mathbf{A}\mathbf{f} = \mathbf{p}$ , we can only approximately have  $\mathbf{A}\Phi(\mathbf{p}) \cong \mathbf{p}$  in some sense such as satisfying the bounded error norm to be explained below, there is not only any guarantee

that  $\Phi(\mathbf{A}\mathbf{f}) = \mathbf{f}$  but also a realistic risk that  $\Phi(\cdot)$  is unstable. This is because the system matrix  $\mathbf{A}$  is underdetermined and the neural network is venerable and may generate an artifact image so that  $\Phi(\mathbf{A}\mathbf{f}) = \mathbf{f} + \mathbf{f}^{ob} + \mathbf{f}^{nl}$ , where  $\mathbf{f}^{ob}$  is s-sparse and observable and  $\mathbf{f}^{nl}$  is in the null space of  $\mathbf{A}$ .  $\mathbf{f}^{nl}$  satisfies  $\mathbf{A}\mathbf{f}^{nl} = 0$ , and  $\|\mathbf{A}\mathbf{f}^{ob}\| \neq 0$  if  $\|\mathbf{f}^{ob}\| \neq 0$ .

In this work, our goal is to design an iterative framework to stabilize an unstable neural network aided by a CS-based sparsity-promoting module. As an idealized setting to show the essential idea, we assume that the input to the neural network is a noise-free dataset  $\mathbf{p}^{(0)} - \mathbf{e}$ , and the output of the CS-module is  $\mathbf{f}$  (more involved analyses including noise are given in the **SI**).

Let us introduce a residual error correction mechanism in the projection domain and assume the residual error is  $\mathbf{p}$ . Then, we want to minimize the following objective function:

$$\operatorname{argmin}_{\mathbf{p}, \mathbf{f}, \mathbf{e}} \frac{1}{2} \|\Phi(\mathbf{p}^{(0)} - \mathbf{e}) - \mathbf{f}\|_2^2 + \frac{\lambda}{2} \|\mathbf{e}\|_2^2 + \frac{\mu}{2} \|\mathbf{p}\|_2^2 + \xi \|\mathbf{H}\mathbf{f}\|_1 \quad s. t. \quad \mathbf{p}^{(0)} - \mathbf{A}\mathbf{f} - \mathbf{p} - \mathbf{e} = \mathbf{0}, \quad (1)$$

where  $\lambda > 0$ ,  $\mu \geq 0$  and  $\xi > 0$  are hyperparameters, the first term is the difference between the outputs of the neural network and the CS-based sparsifying module, the second term is the measured noise energy, the third term is the residual error energy also in the projection domain, and the last term is to enforce the sparsity of the output image of the CS module, which is subject to the data-fidelity constraint in the projection domain.

By substituting  $\mathbf{e} = \mathbf{p}^{(0)} - \mathbf{A}\mathbf{f} - \mathbf{p}$  from the constraint into (1), the objective function can be converted to:

$$\operatorname{argmin}_{\mathbf{p}, \mathbf{f}} \frac{1}{2} \|\Phi(\mathbf{A}\mathbf{f} + \mathbf{p}) - \mathbf{f}\|_2^2 + \frac{\lambda}{2} \|\mathbf{p}^{(0)} - \mathbf{A}\mathbf{f} - \mathbf{p}\|_2^2 + \frac{\mu}{2} \|\mathbf{p}\|_2^2 + \xi \|\mathbf{H}\mathbf{f}\|_1. \quad (2)$$

Let us define

$$L(\mathbf{p}, \mathbf{f}) := \frac{1}{2} \|\Phi(\mathbf{A}\mathbf{f} + \mathbf{p}) - \mathbf{f}\|_2^2 + \frac{\lambda}{2} \|\mathbf{p}^{(0)} - \mathbf{A}\mathbf{f} - \mathbf{p}\|_2^2 + \frac{\mu}{2} \|\mathbf{p}\|_2^2 + \xi \|\mathbf{H}\mathbf{f}\|_1. \quad (3)$$

Then, we can use the block coordinate descent method [40] to optimize (3) as follows:

$$\begin{cases} \mathbf{p}^{(k+1)} = \operatorname{argmin}_{\mathbf{p}} L(\mathbf{p}, \mathbf{f}^{(k)}) \\ \mathbf{f}^{(k+1)} = \operatorname{argmin}_{\mathbf{f}} L(\mathbf{p}^{(k+1)}, \mathbf{f}) \end{cases} \quad (4)$$

To update  $\mathbf{p}$ , we need to solve the following problem:

$$\mathbf{p}^{(k+1)} = \operatorname{argmin}_{\mathbf{p}} \left( \frac{1}{2} \|\Phi(\mathbf{A}\mathbf{f}^{(k)} + \mathbf{p}) - \mathbf{f}^{(k)}\|_2^2 + \frac{\lambda}{2} \|\mathbf{p}^{(0)} - \mathbf{A}\mathbf{f}^{(k)} - \mathbf{p}\|_2^2 \right) + \frac{\mu}{2} \|\mathbf{p}\|_2^2. \quad (5)$$

Computing the partial derivative of the right side of (5), we have

$$\left(\frac{\partial\Phi(\mathbf{A}\mathbf{f}^{(k)}+\mathbf{p})}{\partial(\mathbf{A}\mathbf{f}^{(k)}+\mathbf{p})}\right)^T (\Phi(\mathbf{A}\mathbf{f}^{(k)}+\mathbf{p})-\mathbf{f}^{(k)})+\lambda(\mathbf{A}\mathbf{f}^{(k)}+\mathbf{p}-\mathbf{p}^{(0)})+\mu\mathbf{p}=0. \quad (6)$$

Because the neural network is well-trained to solve the problem  $\mathbf{A}\mathbf{f}=\mathbf{p}$ ,  $\left(\frac{\partial\Phi(\mathbf{A}\mathbf{f}^{(k)}+\mathbf{p})}{\partial(\mathbf{A}\mathbf{f}^{(k)}+\mathbf{p})}\right)^T$  is the backpropagation operator transforming a reconstructed image into measurements. This process is approximately treated as  $\mathbf{A}$ . By ignoring the observable artifact image from the neural network (since in the iterative correction, the artifact image will be gradually reduced; see the next subsection for justification), we assume that  $\mathbf{A}\Phi(\mathbf{A}\mathbf{f}^{(k)}+\mathbf{p})\cong\mathbf{A}\mathbf{f}^{(k)}+\mathbf{p}$ . Therefore, we arrive at

$$\mathbf{p}^{(k+1)}=\frac{\lambda(\mathbf{p}^{(0)}-\mathbf{A}\mathbf{f}^{(k)})}{1+\lambda+\mu}. \quad (7)$$

To update  $\mathbf{f}$ , we solve the following problem:

$$\mathbf{f}^{(k+1)}=\operatorname{argmin}_f\left(\frac{1}{2}\|\Phi(\mathbf{A}\mathbf{f}+\mathbf{p}^{(k+1)})-\mathbf{f}\|_2^2+\frac{\lambda}{2}\|\mathbf{p}^{(0)}-\mathbf{A}\mathbf{f}-\mathbf{p}^{(k+1)}\|_2^2+\xi\|\mathbf{H}\mathbf{f}\|_1\right). \quad (8)$$

With  $\bar{\mathbf{f}}=\mathbf{H}\mathbf{f}$  and  $\mathbf{f}=\mathbf{H}^*\bar{\mathbf{f}}$ , (8) is rewritten as follows:

$$\bar{\mathbf{f}}^{(k+1)}=\operatorname{argmin}_{\bar{\mathbf{f}}}\left(\frac{1}{2}\|\Phi(\mathbf{A}\mathbf{H}^*\bar{\mathbf{f}}+\mathbf{p}^{(k+1)})-\mathbf{H}^*\bar{\mathbf{f}}\|_2^2+\frac{\lambda}{2}\|\mathbf{p}^{(0)}-\mathbf{A}\mathbf{H}^*\bar{\mathbf{f}}-\mathbf{p}^{(k+1)}\|_2^2+\xi\|\bar{\mathbf{f}}\|_1\right). \quad (9)$$

Computing the partial derivative of the right side of (9), we have

$$\left(\mathbf{H}\mathbf{A}^T\left(\frac{\partial\Phi(\mathbf{A}\mathbf{H}^*\bar{\mathbf{f}}+\mathbf{p}^{(k+1)})}{\partial(\mathbf{A}\mathbf{H}^*\bar{\mathbf{f}}+\mathbf{p}^{(k+1)})}\right)^T-\mathbf{H}\right)(\Phi(\mathbf{A}\mathbf{H}^*\bar{\mathbf{f}}+\mathbf{p}^{(k+1)})-\mathbf{H}^*\bar{\mathbf{f}})+\lambda\mathbf{H}\mathbf{A}^T(\mathbf{p}^{(k+1)}-\mathbf{p}^{(0)})+\xi\operatorname{sgn}(\bar{\mathbf{f}})=0. \quad (10)$$

Similarly treating  $\left(\frac{\partial\Phi(\mathbf{A}\mathbf{H}^*\bar{\mathbf{f}}+\mathbf{p}^{(k+1)})}{\partial(\mathbf{A}\mathbf{H}^*\bar{\mathbf{f}}+\mathbf{p}^{(k+1)})}\right)^T$  as  $\mathbf{A}$  and approximately treating  $\mathbf{A}^T\mathbf{A}\cong\rho\mathbf{I}$  with  $\mathbf{I}$  being the identity matrix, (10) can be simplified as

$$(1+\lambda\rho-\rho)\bar{\mathbf{f}}+(\rho-1)\mathbf{H}\Phi(\mathbf{A}\mathbf{H}^*\bar{\mathbf{f}}+\mathbf{p}^{(k+1)})+\lambda\mathbf{H}\mathbf{A}^T(\mathbf{p}^{(k+1)}-\mathbf{p}^{(0)})+\xi\operatorname{sgn}(\bar{\mathbf{f}})=0. \quad (11)$$

From (7), we have

$$\mathbf{p}^{(0)}=\frac{(1+\lambda+\mu)\mathbf{p}^{(k+1)}}{\lambda}+\mathbf{A}\mathbf{f}^{(k)}. \quad (12)$$

By substituting (12) into (11), we have

$$(1 + \lambda\rho - \rho)\bar{\mathbf{f}} + (\rho - 1)\mathbf{H}\Phi(\mathbf{A}\mathbf{H}^*\bar{\mathbf{f}} + \mathbf{p}^{(k+1)}) - \lambda\rho\mathbf{H}\mathbf{f}^{(k)} - (1 + \mu)\mathbf{H}\mathbf{A}^T\mathbf{p}^{(k+1)} + \xi\text{sgn}(\bar{\mathbf{f}}) = 0. \quad (13)$$

Noting that

$$\mathbf{A}\mathbf{H}^*\bar{\mathbf{f}} + \mathbf{p}^{(k+1)} = \mathbf{A}\left(\mathbf{H}^*\bar{\mathbf{f}} + \Phi(\mathbf{p}^{(k+1)})\right), \quad (14)$$

and approximating  $\Phi(\mathbf{A}\mathbf{H}^*\bar{\mathbf{f}} + \mathbf{p}^{(k+1)})$  as  $\left(\mathbf{H}^*\bar{\mathbf{f}} + \Phi(\mathbf{p}^{(k+1)})\right)$ , (13) can be reformulated as

$$\lambda\rho\bar{\mathbf{f}} + (\rho - 1)\left(\mathbf{H}\Phi(\mathbf{p}^{(k+1)})\right) - \lambda\rho\mathbf{H}\mathbf{f}^{(k)} - (1 + \mu)\mathbf{H}\mathbf{A}^T\mathbf{p}^{(k+1)} + \xi\text{sgn}(\bar{\mathbf{f}}) = 0. \quad (15)$$

Since  $\mathbf{A}\Phi(\mathbf{p}) \cong \mathbf{p}$ , we can approximately change (15) to

$$\lambda\rho\bar{\mathbf{f}} = \lambda\rho\mathbf{H}\mathbf{f}^{(k)} + (1 + \mu\rho)\mathbf{H}\Phi(\mathbf{p}^{(k+1)}) - \xi\text{sgn}(\bar{\mathbf{f}}). \quad (16)$$

Therefore,  $\mathbf{f}^{(k+1)}$  can be obtained via soft-threshold filtering:

$$\mathbf{f}^{(k+1)} = \mathbf{H}^* \mathbf{S}_{\frac{\xi}{\lambda\rho}} \left( \mathbf{H} \left( \mathbf{f}^{(k)} + \frac{1+\mu\rho}{\lambda\rho} \Phi(\mathbf{p}^{(k+1)}) \right) \right). \quad (17)$$

where the soft-thresholding kernel is defined as

$$\mathbf{S}_\varepsilon(x) = \begin{cases} 0, & |x| < \varepsilon \\ x - \text{sgn}(x)\varepsilon & \text{otherwise} \end{cases}. \quad (18)$$

Combining Eqs.(7) and (17), we obtain a set of formulas:

$$\begin{cases} \mathbf{p}^{(k+1)} = \frac{\lambda(\mathbf{p}^{(0)} - \mathbf{A}\mathbf{f}^{(k)})}{1 + \lambda + \mu} \\ \mathbf{f}^{(k+1)} = \mathbf{H}^* \mathbf{S}_{\frac{\xi}{\lambda\rho}} \left( \mathbf{H} \left( \mathbf{f}^{(k)} + \frac{1+\mu\rho}{\lambda\rho} \Phi(\mathbf{p}^{(k+1)}) \right) \right) \end{cases}. \quad (19)$$

Let us denote  $\frac{\xi}{\lambda\rho} = \varepsilon$  and simplify (19) as

$$\begin{cases} \mathbf{p}^{(k+1)} = \frac{\lambda(\mathbf{p}^{(0)} - \mathbf{A}\mathbf{f}^{(k)})}{1 + \lambda + \mu} \\ \mathbf{f}^{(k+1)} = \mathbf{H}^* \mathbf{S}_\varepsilon \left( \mathbf{H} \left( \mathbf{f}^{(k)} + \frac{1+\mu\rho}{\lambda\rho} \Phi(\mathbf{p}^{(k+1)}) \right) \right) \end{cases}. \quad (20)$$

Clearly, (20) agrees with our heuristically-derived ACID network. In other words, ACID is a special case of (20) after the weighting parameters are properly selected.

Particularly, the term  $\|\mathbf{H}\mathbf{f}\|_1$  in our objective function (2) is specialized as a discrete graduate function  $g(\mathbf{f})$ :

$$g(\mathbf{f}) = \sum_{i_w=2}^{I_w} \sum_{i_h=2}^{I_h} (|\mathbf{f}(i_w, i_h) - \mathbf{f}(i_w - 1, i_h)| + |\mathbf{f}(i_w, i_h) - \mathbf{f}(i_w, i_h - 1)|), \quad (21)$$

where  $I_w$  and  $I_h$  represent the width and height of a reconstructed image, and the gradients on the image border are assumed to be zero. An FFT-based algorithm, FTVd [41], is employed to find the sparse solution for  $\mathbf{f}$ . Note that the generic TV favors piecewise constant regions, while high-order TV encourages piecewise polynomials [42]. Here, the input to the CS-based sparsifying module is normalized to  $[0, 1]$  to facilitate the selection of the regularized parameters, which requires de-normalization of the output of the CS module. In the CS framework, the robust null space property ensures the stability of sparse regularized recovery [43, 44]. Ideally, the sparse transform  $\mathbf{H}$  is unitary, as is the case of the orthogonal wavelet decomposition. Similar results can be also obtained in important non-unitary cases; in particular, the TV minimization [45] as used in this study.

Under practically reasonable conditions such as noisy and insufficient data, the ACID iteration will converge to a feasible solution subject to an uncertain range proportional to the noise level (see the **SI** for more details).

## (2) Selected Unstable Networks Stabilized in the ACID Framework

The Ell-50 and DAGAN networks are two examples of unstable deep reconstruction networks to validate the effectiveness of ACID, both of which were used in [8] and suffered from the three kinds of instabilities. Ell-50 and DAGAN are for CT and MRI reconstruction respectively (more details in **SI**).

The projection data for Ell-50-based CT reconstruction were generated using the *radon* function in MATLAB R2017b, where 50 means the number of projections. For fairness, we only used the trained networks in [27], which were the same as those used in [8]. The test data for Case C1 was provided by the authors of [8], which can be downloaded from the related website [8]. Case C2 with the bird icon and the text ‘‘A BIRD?’’ was provided by the authors of [17] and downloaded from the website specified in [8]. The test images consisted of  $512 \times 512$  pixels and contained structural features without tiny perturbation. To generate adversarial attacks, the proposed method in [8] was employed to compute adversarial samples. Then, we obtained C3 and C4 images by adding tiny perturbations to C1 and C2 images respectively. Furthermore, the adversarial attacks were performed on the whole ACID by perturbing C1 and C2 images to C5 and C6 images. More details on the datasets and implementations details are in the **SI**.

To evaluate ACID in the MRI case, the DAGAN network was employed [29], which was proposed for single-coil MRI reconstruction. The sub-sampling rates in DAGAN can be freely selected. In this study, we set the subsampling rate to 10% and subsampled these images with the 2D Gaussian sampling pattern. Also, the DAGAN network was re-trained, with the parameters and the training datasets being kept the same as that used in [29]. The test images were a series of brain images, each of which consisted of  $256 \times 256$  pixels. Case M1 was randomly chosen from the test dataset [29], then the phrase ‘‘HELLO NATURE’’ was introduced into the image as structural changes. Case M2 was the same as that given

in [8], where the sentence “CAN U SEE IT” and “◇” were added to the original image. Also, we adopted the same technique used in [8] to generate adversarial attacks. The resultant tiny perturbations were added to M1 and M2 images to obtain M3 and M4 images [8]. Furthermore, the uniform noise with zero mean and 15 deviations over the pixel value range [0, 255] was superimposed to Cases M1 and M2 to obtain M5 and M6 images respectively. AUTOMAP [9] was employed, since it is popular and was used in [8]. M7 was randomly chosen from the DAGAN test dataset, which can be freely downloaded [29]. Additionally, Cases M8 and M9 were generated putting a radial mask of a 20% subsampling rate on the M1 and M2 images, which were used to compare ACID with ADMM-net [30]. Cases M10 and M12 were generated via direct perturbation to the entire ACID system. More details are also included in the **SI**.

### (3) Image Quality Assessment

To quantitatively compare the results obtained with different reconstruction methods, the peak signal-to-noise ratio (PSNR) was employed to measure the difference between reconstructed images and the corresponding ground truths. Also, the structural similarity (SSIM) was used to assess the similarity between images. For qualitative analysis, the reconstructed results were visually inspected of structural changes (i.e., the inserted text, bird, and patterns) and artifacts induced by perturbation. In this context, we mainly focused on details such as edges and integrity such as overall appearance.

To highlight the merits and stability of ACID, the state-of-the-art CS-based methods served as the reference. For CT, the sparsity-regularized method combining X-lets (shearlets) and TV was the benchmark [46], which was consistent with the selection in [8]. For MRI, the total generalized variation (TGV) method served as the baseline [47]. All the parameters including the number of iterations for these CS methods were optimized for a fair comparison.

### (4) Numerical Verification of Convergence

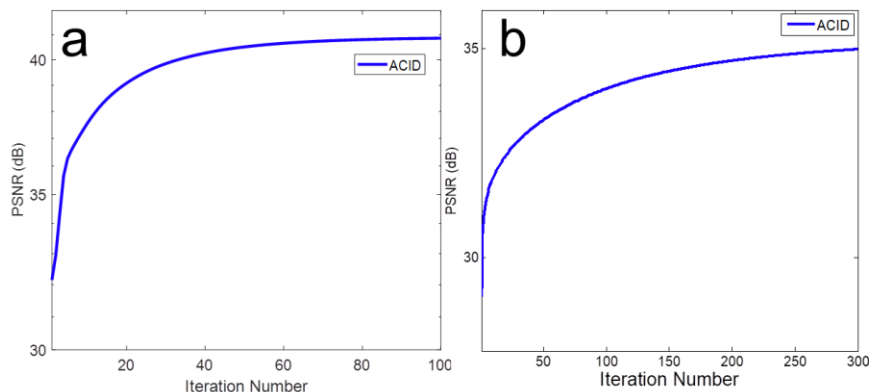


**Figure 9. The convergence of ACID in terms of PSNR in the C1 and M2 cases. a and b show the convergence curves for C1 and M2, respectively.**

To verify our theoretical analysis on the convergence of ACID, we numerically investigated the convergence rate and computational cost. We used PSNR as the metric to reflect the convergence of ACID (Fig. 9). It could be seen that ACID converged after about

30 iterations for CT, and it became stable after 250 iterations for MRI. Therefore, in this study we set the number of iterations to 100 and 300 for CT and MRI, respectively.

### (5) ACID Parameterization

The ACID method mainly involves two parameters:  $\lambda$  and  $\xi$  ( $\mu = 0$ ). These parameters were optimized by comparing quantitative and qualitative results, as summarized in Table 1.

**Table 1. Parameters used in the main experiments.**

Variables	C1	C2	C3	C4	C5	C6	M1	M2	M3
$\xi(10^{-3})$	0.700	0.700	0.500	1.100	0.100	0.700	0.333	0.333	0.500
$\lambda$	0.76	0.76	14	2.4	3.0	0.76	0.1	0.1	0.01
Variables	M4	M5	M6	M7	M8	M9	M10	M11	M12
$\xi(10^{-3})$	0.500	0.667	0.667	0.333	0.500	0.500	0.100	0.100	0.100
$\lambda$	0.01	0.01	0.01	0.1	0.01	0.01	0.01	0.01	0.01

**Acknowledgement:** W. Wu is supported by NIH grants U01EB017140 and the Li Ka Shing Medical Foundation. V. Vardhanabhuti is partially supported by the Li Ka Shing Medical Foundation. H. Yu, H. Shan, W. Cong, C. Niu, and G. Wang are partially supported by NIH grants U01EB017140, R01CA237267, R01CA233888, and R01EB026646.

**Corresponding Authors:** Hengyong Yu, Varut Vardhanabhuti and Ge Wang

### Author Contributions:

G. Wang initiated the project, and supervised the team in collaboration with H. Yu and V. Vardhanabhuti;

W. Wu, H. Yu, G. Wang designed the ACID network;

W. Wu and D. Hu conducted the experiments;

H. Yu, W. Cong, G. Wang established the mathematical model and performed the theoretical analysis;

W. Wu, H. Yu and G. Wang drafted the manuscript;

W. Wu, D. Hu and H. Shan worked on user-friendly codes/data sharing; and all co-authors participated discussions, contributed technical points, and revised the manuscript iteratively.

**Data and code availability:** The source codes, trained networks and all test datasets used in this study are publicly available on the website: <https://zenodo.org/record/4533291>.

### References

1. *Number of magnetic resonance imaging (MRI) units in selected countries as of 2019.* 2020: Health, Pharma & Medtech, Medical Technology.

2. *Over 75 Million CT Scans Are Performed Each Year and Growing Despite Radiation Concerns*. 2020.
3. V.R. Fuchs and H.C. Sox Jr, *Physicians' views of the relative importance of thirty medical innovations*. Health Affairs, 2001. **20**(5): p. 30-42.
4. G. Wang, *A Perspective on Deep Imaging*. IEEE Access, 2016. **4**: p. 8914-8924.
5. G. Wang, J.C. Ye, K. Mueller, and J.A. Fessler, *Image Reconstruction is a New Frontier of Machine Learning*. IEEE Trans Med Imaging, 2018. **37**(6): p. 1289-1296.
6. G. Wang, J.C. Ye, and B. De Man, *Deep learning for tomographic image reconstruction* Nat Mach Intell, 2020. **2**(6): p. 737-748.
7. G. Wang, Y. Zhang, X.J. Ye, and X.Q. Mou, *Machine learning for tomographic imaging*. 2019: IOP Publishing. 410.
8. V. Antun, F. Renna, C. Poon, B. Adcock, and A.C. Hansen, *On instabilities of deep learning in image reconstruction and the potential costs of AI*. Proceedings of the National Academy of Sciences, 2020.
9. B. Zhu, J.Z. Liu, S.F. Cauley, B.R. Rosen, and M.S. Rosen, *Image reconstruction by domain-transform manifold learning*. Nature, 2018. **555**(7697): p. 487-492.
10. F. Knoll, T. Murrell, A. Sriram, N. Yakubova, J. Zbontar, M. Rabbat, A. Defazio, M.J. Muckley, D.K. Sodickson, and C.L. Zitnick, *Advancing machine learning for MR image reconstruction with an open competition: Overview of the 2019 fastMRI challenge*. Magnetic resonance in medicine, 2020. **84**(6): p. 3054-3070.
11. F. Natterer, *The mathematics of computerized tomography*. 2001: SIAM.
12. A.C. Kak, M. Slaney, and IEEE Engineering in Medicine and Biology Society., *Principles of computerized tomographic imaging*. 1988, New York: IEEE Press. x, 329 p.
13. R.A. Vogel, D. Kirch, M. LeFree, and P. Steele, *A new method of multiplanar emission tomography using a seven pinhole collimator and an Anger scintillation camera*. J Nucl Med, 1978. **19**(6): p. 648-54.
14. J. Nuyts, B. De Man, J.A. Fessler, W. Zbijewski, and F.J. Beekman, *Modelling the physics in the iterative reconstruction for transmission computed tomography*. Physics in medicine and biology, 2013. **58**(12): p. R63.
15. E.J. Candes and T. Tao, *Near-optimal signal recovery from random projections: Universal encoding strategies?* IEEE transactions on information theory, 2006. **52**(12): p. 5406-5425.
16. G.T. Herman and R. Davidi, *Image reconstruction from a small number of projections*. Inverse problems, 2008. **24**(4): p. 045011.
17. N.M. Gottschling, V. Antun, B. Adcock, and A.C. Hansen, *The troublesome kernel: why deep learning for inverse problems is typically unstable*. arXiv preprint arXiv:2001.01258, 2020.
18. R.G. Baraniuk, *Compressive sensing [lecture notes]*. IEEE signal processing magazine, 2007. **24**(4): p. 118-121.
19. G.H. Chen, J. Tang, and S. Leng, *Prior image constrained compressed sensing (PICCS): a method to accurately reconstruct dynamic CT images from highly undersampled projection data sets*. Medical physics, 2008. **35**(2): p. 660-663.
20. L.I. Rudin, S. Osher, and E. Fatemi, *Nonlinear total variation based noise removal algorithms*. Physica D: nonlinear phenomena, 1992. **60**(1-4): p. 259-268.

21. G. Liu, Z. Lin, S. Yan, J. Sun, Y. Yu, and Y. Ma, *Robust recovery of subspace structures by low-rank representation*. IEEE transactions on pattern analysis and machine intelligence, 2012. **35**(1): p. 171-184.
22. I. Tomic and P. Frossard, *Dictionary learning*. IEEE Signal Processing Magazine, 2011. **28**(2): p. 27-38.
23. M. Danilova, P. Dvurechensky, A. Gasnikov, E. Gorbunov, S. Guminov, D. Kamzolov, and I. Shibaev, *Recent Theoretical Advances in Non-Convex Optimization*. arXiv preprint <https://arxiv.org/abs/2012.06188>, 2020.
24. X. Wang, J. Yan, B. Jin, and W. Li, *Distributed and Parallel ADMM for Structured Nonconvex Optimization Problem*. IEEE Trans Cybern, 2019.
25. R.F. Barber and E.Y. Sidky, *MOCCA: Mirrored Convex/Concave Optimization for Nonconvex Composite Functions*. J Mach Learn Res, 2016. **17**(144): p. 1-51.
26. J. Schwab, S. Antholzer, and M. Haltmeier, *Deep null space learning for inverse problems: convergence analysis and rates*. Inverse Problems, 2019. **35**: p. 025008 (13 pages).
27. K.H. Jin, M.T. McCann, E. Froustey, and M. Unser, *Deep convolutional neural network for inverse problems in imaging*. IEEE Transactions on Image Processing, 2017. **26**(9): p. 4509-4522.
28. H. Yu and G. Wang, *Compressed sensing based interior tomography*. Physics in medicine and biology, 2009. **54**(9): p. 2791.
29. G. Yang, S. Yu, H. Dong, G. Slabaugh, P.L. Dragotti, X. Ye, F. Liu, S. Arridge, J. Keegan, and Y. Guo, *DAGAN: Deep de-aliasing generative adversarial networks for fast compressed sensing MRI reconstruction*. IEEE transactions on medical imaging, 2018. **37**(6): p. 1310-1321.
30. J. Sun, H. Li, and Z. Xu. *Deep ADMM-Net for compressive sensing MRI*. in *Advances in neural information processing systems*. 2016.
31. K. Hammernik, T. Klatzer, E. Kobler, M.P. Recht, D.K. Sodickson, T. Pock, and F. Knoll, *Learning a variational network for reconstruction of accelerated MRI data*. Magnetic resonance in medicine, 2018. **79**(6): p. 3055-3071.
32. H. Chen, Y. Zhang, Y. Chen, J. Zhang, W. Zhang, H. Sun, Y. Lv, P. Liao, J. Zhou, and G. Wang, *LEARN: Learned experts' assessment-based reconstruction network for sparse-data CT*. IEEE transactions on medical imaging, 2018. **37**(6): p. 1333-1347.
33. G. Chen, X. Hong, Q. Ding, Y. Zhang, H. Chen, S. Fu, Y. Zhao, X. Zhang, H. Ji, and G. Wang, *AirNet: Fused analytical and iterative reconstruction with deep neural network regularization for sparse-data CT*. Medical physics, 2020. **47**(7): p. 2916-2930.
34. L. Xu, C. Lu, Y. Xu, and J. Jia. *Image smoothing via L<sub>0</sub> gradient minimization*. in *Proceedings of the 2011 SIGGRAPH Asia Conference*. 2011.
35. W. Cong, G. Wang, Q. Yang, J. Li, J. Hsieh, and R. Lai, *CT image reconstruction on a low dimensional manifold*. Inverse Problems and Imaging, 2019. **13**(3).
36. M.J. Colbrook, V. Antun, and A.C. Hansen, *On the existence of stable and accurate neural networks for image reconstruction*.
37. V. Antun, M.J. Colbrook, and A.C. Hansen, *Can stable and accurate neural networks be computed?--On the barriers of deep learning and Smale's 18th problem*. arXiv preprint arXiv:2101.08286, 2021.
38. A. Katsevich, *Analysis of an exact inversion algorithm for spiral cone-beam CT*. Physics in Medicine and Biology, 2002. **47**(15): p. 2583.

39. L. Axel, R. Summers, H. Kressel, and C. Charles, *Respiratory effects in two-dimensional Fourier transform MR imaging*. *Radiology*, 1986. **160**(3): p. 795-801.
40. P. Tseng, *Convergence of a Block Coordinate Descent Method for Nondifferentiable Minimization*. *Journal of Optimization Theory and Applications*, 2001. **109**(3): p. 475–494.
41. Y. Ye, H. Yu, and G. Wang, *Exact interior reconstruction with cone-beam CT*. *International journal of biomedical imaging*, 2007. **2007**.
42. Y. Wang, J. Yang, W. Yin, and Y. Zhang, *A new alternating minimization algorithm for total variation image reconstruction*. *SIAM Journal on Imaging Sciences*, 2008. **1**(3): p. 248-272.
43. S. Foucart and H. Rauhut, *A mathematical introduction to compressive sensing* 2013, Birkhäuser, New York, NY.
44. N.M. Gottschling, V. Antun, B. Adcock, and A.C. Hansen, *The troublesome kernel: why deep learning for inverse problems is typically unstable*. 2020.
45. C. Poon, *On the Role of Total Variation in Compressed Sensing*. *SIAM Journal on Imaging Sciences*, 2015. **8**(1): p. 682-720.
46. J. Ma and M. März, *A multilevel based reweighting algorithm with joint regularizers for sparse recovery*. arXiv preprint arXiv:06941, 2016.
47. F. Knoll, C. Clason, K. Bredies, M. Uecker, and R. Stollberger, *Parallel imaging with nonlinear reconstruction using variational penalties*. *Magnetic resonance in medicine*, 2012. **67**(1): p. 34-41.

# Supplementary Information for “Stabilizing Deep Tomographic Reconstruction Networks”

Weiwen Wu<sup>1,5</sup>, Dianlin Hu<sup>2</sup>, Wenxiang Cong<sup>1</sup>, Hongming Shan<sup>1,3</sup>, Shaoyu Wang<sup>4</sup>,  
Chuang Niu<sup>1</sup>, Pingkun Yan<sup>1</sup>, Hengyong Yu<sup>4,\*</sup>, Varut Vardhanabhuti<sup>5,\*</sup>, Ge Wang<sup>1,\*</sup>

<sup>1</sup>Biomedical Imaging Center, Center for Biotechnology and Interdisciplinary Studies,  
Department of Biomedical Engineering, Rensselaer Polytechnic Institute, Troy, NY,  
USA

<sup>2</sup>The Laboratory of Image Science and Technology, Southeast University, Nanjing,  
China

<sup>3</sup>Institute of Science and Technology for Brain-inspired Intelligence, Fudan University,  
Shanghai, China

<sup>4</sup>Department of Electrical & Computer Engineering, University of Massachusetts  
Lowell, Lowell, MA, USA

<sup>5</sup>Department of Diagnostic Radiology, Li Ka Shing Faculty of Medicine, The  
University of Hong Kong, Hong Kong SAR, China

**Corresponding Authors:** Hengyong\_yu@uml.edu, varv@hku.hk, and  
wangg6@rpi.edu

# ***Table of Contents***

<b>I. Deep Networks &amp; Datasets</b> .....	<b>1</b>
A. EII-50 Network.....	1
B. DAGAN Network.....	4
C. AUTOMAP Network.....	7
D. ADMM-net.....	10
<b>II. CS Based Reconstruction Methods</b> .....	<b>12</b>
A. CS-inspired Reconstruction.....	12
B. Dictionary Learning Based Reconstruction.....	14
<b>III. ACID Architecture &amp; Adversarial Attacks</b> .....	<b>19</b>
A. ACID Implementation.....	19
B. Adversarial Attacks.....	20
<b>IV. Theoretical Analyses on the ACID Workflow</b> .....	<b>28</b>
A. Theoretical Background.....	28
B. Bounded Error Norm (BEN) Property.....	31
C. Convergence Analysis.....	35
<b>References</b> .....	<b>37</b>

# I. Deep Networks & Datasets

## A. EII-50 Network

**A.1. Overall.** EII-50 is a special form of FBPCConvNet, which is a classic neural network for CT imaging proposed in [1]. The FBPCConvNet with multiple-solution decomposition and residual learning [2] was proposed to remove sparse-data artifacts and preserve image features and structures. The reconstruction performance of the FBPCConvNet network was validated, outperforming the total variation-regularized based iterative reconstruction using the realistic phantoms. Besides, it is very fast to reconstruct an image on GPU. In this study, the training dataset mainly contains ellipses with different intensity, size and locations. The network is named EII-50, indicating that the measurements were collected from 50 different views. This network was trained by the authors of [1], which can be freely downloaded (<https://github.com/panakino/FBPCConvNet>).

**A.2. Network Architecture.** The EII 50 was trained to reconstruct  $f$  from measurements  $p = Af$ , where  $A$  represents a subsampling system matrix, with which only 50 uniformly spaced radial lines are collected. Because the FBPCConvNet is an image post-processing network, it is trained from filtered back-projection reconstruction images rather than directly learning a mapping from  $p$  to  $f$ . The network first employs filtered backprojection to convert  $p$  to  $\hat{f} = A^+p$  where  $A^+$  represents the filtered backprojection, and it is considered the first layer of the neural network.

The FBPCConvNet is a useful model based on U-net [3], which is considered as an encoder-decoder pair. The main features of U-net based FBPCConvNet are summarized as the following three features: Multilevel decomposition, multichannel filtering, and residual learning. The network input is an image with  $512 \times 512$  pixels, it is first down-sampled 5 times for encoding, and then the achieved low-dimensional image features are up-sampled to  $512 \times 512$  pixels. Besides, the skip concatenation operator is employed in this network. The EII-50 network consists of convolutional and deconvolutional layers, and each convolutional and deconvolutional layers are followed by a batch normalization (BN) and ReLU layers. For the EII-50 network training, the sizes of filters and stride were set to  $3 \times 3$  and 1 respectively. Moreover, the EII-50 network details are shown in Fig. S1.

**A.3. Network Training.** The few-view and full-view FBP images are treated as the input and output of the EII-50 respectively. In this study, the network was implemented using the MatConvNet [4] toolbox with a slight modification to train and evaluate the performance. To prevent the divergence of the cost

function,

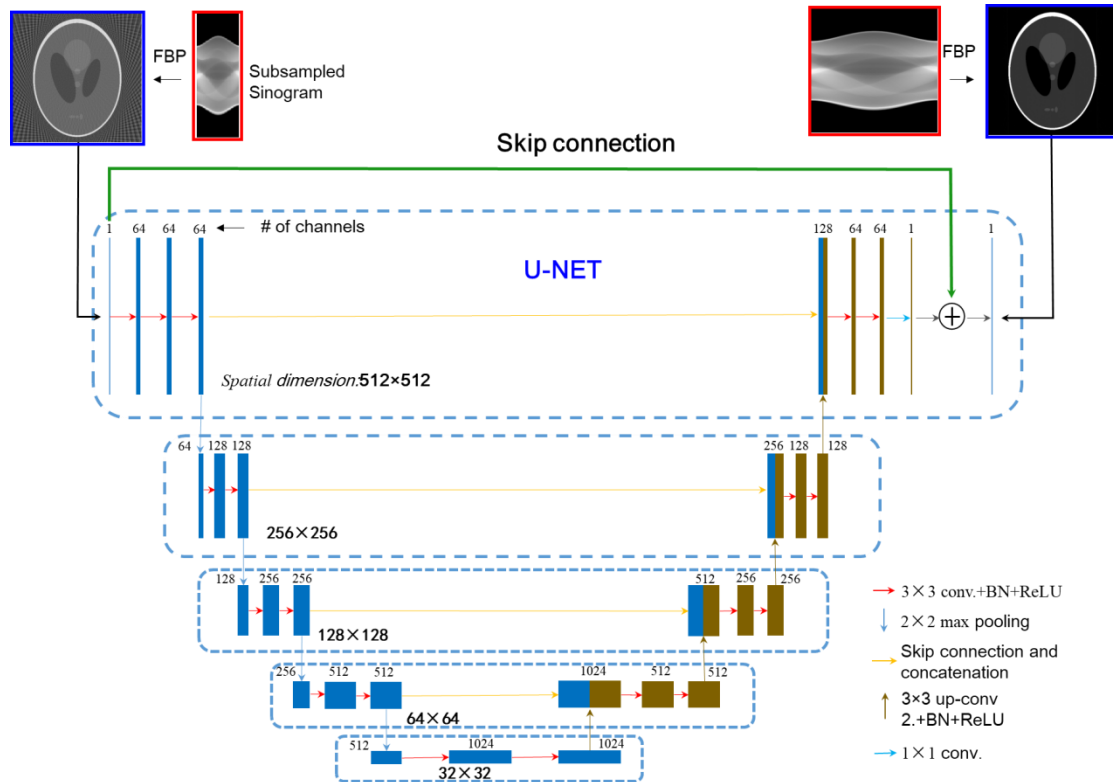


Fig. S1. Architecture for EII-50.

the MatConvNet [4] toolbox was slightly modified by clipping the computed gradients to a fixed range [5]. In this study, we just used the trained network weights of [1] downloaded from GitHub (<https://github.com/panakino/FBPConvNet>). Such a configuration is consistent with the literature [6]. The loss function plays an important role in controlling the image quality, and the mean square error (MSE) between the network output and the corresponding label is considered in EII-50. Since the employed network was performed on a TITAN Black GPU graphic processor (NVIDIA Corporation), the total training time took about 15 hours with 101 epochs [6]. Regarding the learning rate, it was decreased logarithmically from 0.01 to 0.001. Besides, the batch size, momentum and clipping value were set as 1, 0.99 and  $10^{-2}$ , respectively.

**A.4. Training Data.** Regarding the training dataset, the total number of training images is 475, and the number of test images is 25. The training images were reconstructed via filtered backprojection with sparse-view measurement. The dynamic range of the reconstructed images was controlled to the range of  $[-500, 500]$ . Since only ellipses with different sizes, locations and intensities were simulated, the projections were accurately analytically computed [7]. The scanning geometry was set to produce parallel beams [8]. The number of full projections and the number of detector units were set as 1,000 and 729. Especially, the functions of *radon* and *iradon* in MATLAB were employed to realize the projection and backprojection operations. For sparse-data

reconstruction, only 50 views were extracted from full projections, and then they were input to the selected networks in this paper. This case is one of typical sparse views reconstruction [9-11]. The ground truths are FBP images from fully projections (i.e., 1000 views).

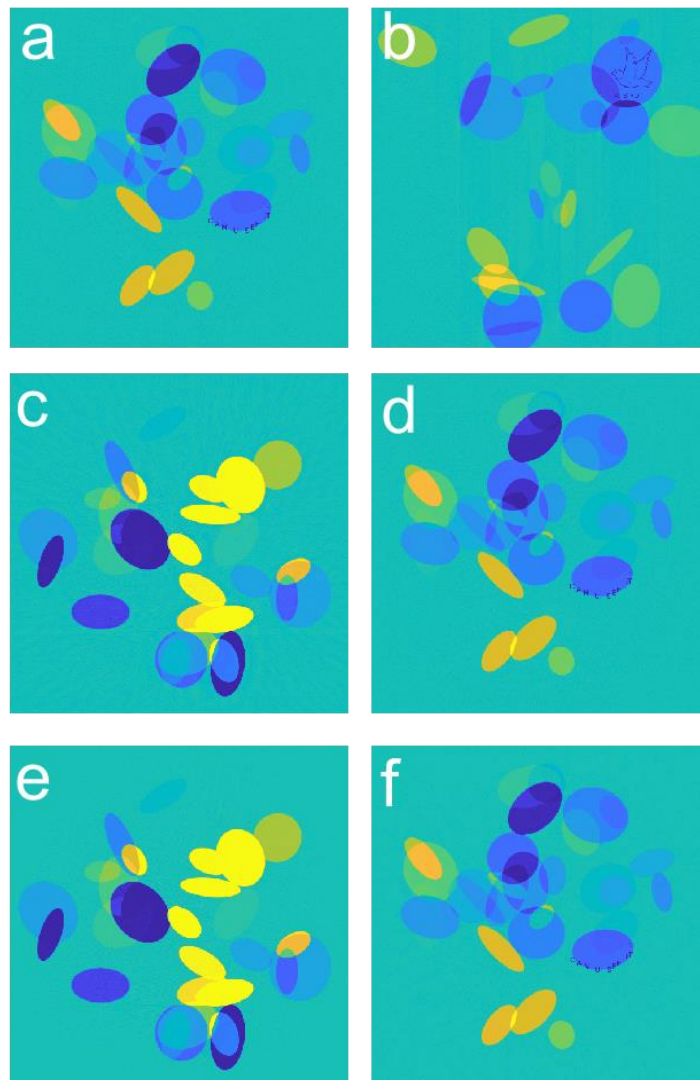


Fig. S2. Test images for CT study in terms of CT imaging. **a-f** represent C1-C6 cases.

**A.5. Test Data.** To demonstrate the instability of neural network (i.e., EII-50), the additional symbol “♡” and the text “CAN YOU SEE IT” were first embedded in the original image, which was provided by the authors of [6]. These artificial features were to mimic the structure changes and further validate the instability of the neural network in this case (see Fig. S2). In this study, this image phantom was also treated as Case C1 to validate the instability of EII-50 and the stability of our proposed ACID method. Besides, a slightly complicated phantom with inserted the logo of a bird and the symbol “A BIRD?” were provided by the authors of [12] and downloaded from [6], which is defined as Case C2. The test image consists of 512×512 pixels, and it contains structural features without tiny perturbation. To generate adversarial attacks, the proposed method in [6] was employed to induce tiny perturbations. The original image of case C3 was randomly selected from the test datasets of

<https://github.com/panakino/FBPConvNet>, which contains no perturbation. Here, the tiny perturbation is added to the original image with the same technique used in [6], and then we obtained Case C3. Regarding Case C4, the same technique used in [6] was employed to generate the tiny perturbation and then embedded into Case 1 to obtain C4. To validate the ability of ACID against adversarial attacks, the adversarial samples (see section III in this supplementary information for details) for the whole ACID were generated and added into the C3 and C1 images respectively to obtain the cases of C5 and C6. The searched adversarial attacks in the whole ACID flowchart is greater than those used in a single neural network (i.e., EII-50) in terms of  $L_2$ -norm. For the EII-50 network, it was implemented in MATLAB with the MatConvNet platform based on the Window 10 system with one NVIDIA TITAN XP graphics processing units (GPUs) installed on a PC (16 CPUs @3.70GHz, 32.0GB RAM and 8.0GB VRAM).

## B. DAGAN Network

**B.1. Overall.** The DAGAN architecture is a network to reduce aliasing artifacts with the U-Net [3] based generator [13]. To enhance the ability of the reconstruction method in preserving image texture and edges, DAGAN incorporates an innovative content loss in the adversarial loss. Besides, it also introduces frequency-domain features to encourage coherence in image and frequency domains. Compared with the traditional CS-based and some other deep learning methods [14-16], the DAGAN method achieved superior performance in retaining image details. Besides, as one of the post-processing methods, the speed of DAGAN reconstruction is very fast. In this study, the DAGAN network was tested on a single-coil MRI with 10% and 20% subsampling rates. The trained weights are not available online, however, but the authors of [13] provide the implementation details of DAGAN. With this help, we retrained the DAGAN with different subsampling rates and masks. The architecture, training parameters, and test data are summarized in the following subsections.

**B.2. Network Architecture.** The DAGAN [13] network was proposed for fast MRI reconstruction from subsampled measurement data. In the case of DAGAN, the measurement data is  $\mathbf{p} = \mathbf{A}\mathbf{f}$ , where  $\mathbf{A}$  is the subsampled discrete Fourier transform. The aim of DAGAN is to recovery  $\hat{\mathbf{f}}$  from degraded image  $\mathbf{f}$  that is reconstructed directly via inverse Fourier transform from the zero-filled measurement data.

To restore high-quality MR images from measurement, DAGAN adopted a conditional generative adversarial network (GAN) [17-19] model. It consists of two modules: generator and discriminator. The generator is to recover the image and the discriminator aims to make the recovered image more realistic. The authors in [13] provided three variants of DAGAN, and we selected the full model version (Pixel-Frequency-Perceptual-GAN-Refinement) in our

experiments. According to parameter settings in [13] and the codes provided by the authors of [6], we retrained the DAGAN by ourselves.

The architecture of the generator is illustrated in Fig. S3. It adopted the basic U-Net type structure, which contains 8 convolutional layers and 8 deconvolutional layers. All of them are followed by batch normalization layers to accelerate training convergence and overcome overfitting. The leaky ReLU layers were adopted as the activation function with a slope equal to 0.2 when the input is less than 0. Additionally, skip connections are employed to concentrate on encoder and decoder features to gain reconstruction details and promote the information flow. The hyperbolic tangent function was applied as the activate function for the output of the last convolutional layer. Then a global skip connection, adding the input data and the output of the hyperbolic tangent function together, is then clipped by a ramp function to scale the output of the generator to the range  $[-1, 1]$ . The global skip connection can accelerate the training convergence and improve the performance of the network. More parameter settings can be found in Fig. S3. For more detailed information on the DAGAN network, please refer to [13].

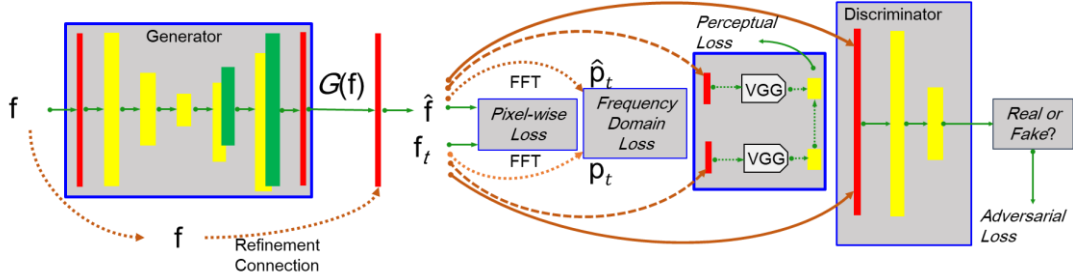


Fig. S3. The architecture of the generator in DAGAN.

**B.3. Training Parameters.** The loss function of DAGAN is formulated as follows:

$$L_{DAGAN} = \sigma_1 L_{Img} + \sigma_2 L_{frq} + \sigma_3 L_{VGG} + \sigma_4 L_D \quad s.t. \sigma_1, \sigma_2, \sigma_3, \sigma_4 > 0, \quad (S.1.1)$$

where  $L_{Img}$  computes the Euclidean distance in image domain between the reconstructed image and the ground truth image, and  $L_{frq}$  accounts for the  $\ell_2$  distance in the k-space between the generated image and the reference image. To constraint the similarity loss  $L_{VGG}$  in feature space, the trained VGG-16 was used to optimize the  $\ell_2$  distance between different features, which are outputs based on the reconstructed image and the reference image respectively, which is the same as [20]. In particular, the feature maps generated of the conv4 layer in VGG-16 area were used to calculate  $L_{VGG}$ . Last,  $L_D$  is the adversarial loss using a cross entropy to make the generated image more realistic.  $\sigma_1, \sigma_2, \sigma_3, \sigma_4$  are the hyper-parameters to balance different constraint terms. According to [13], they were set to 15, 0.1, 0.0025 and 1, respectively. The generator and the discriminator were optimized jointly using the Adam algorithm [21] with  $\beta_1 = 0.5$  and  $\beta_2 = 0.999$ . Specifically, the learning rate was initially set to 0.0001, it was decreased half every 5 epochs, and the batch size is 25. To prevent overfitting, an early stopping strategy was adopted via measuring the loss  $L_{frq}$  and

validation set, and the early stopping number was set to 10.

**B.4. Training Data.** The datasets for training the DAGAN network were provided by the MICCAI 2013 Grand Challenge and are publicly available in <https://my.vanderbilt.edu/masi/workshops/>. More details about the training datasets are given in <https://github.com/tensorlayer/DAGAN>. Specifically, to exclude the negative influence on the DAGAN network, all the images, where more than threshold  $T$  of the image are the background, were dropped. In our experiments,  $T$  was set to 90%. After data preprocessing, there are 15912 images for training and 4977 images for testing. All the images are T1-weighted brain MR images. Again, the data augmentation was applied to eliminate overfitting, including image flipping, rotation, shifting and so on [13].

In the experiments, DAGAN is to recover images from 10% subsampling rate using 2D Gaussian mask and the radial mask of a 20% subsampling rate respectively. Two models of the DAGAN network were trained for these two subsampling masks. Particularly, it took about 4.5 hours to train images reconstructed from the Gaussian mask, and 14.4 hours to train images reconstructed from the radial mask. All the codes were implemented with TensorLayer and Tensorflow frameworks [13].

**B.5. Testing Data.** To test the robustness of DAGAN in terms of small structural changes, adversarial attacks and noise, the symbols “HELLO NATURE” and “CAN YOU SEE IT” were embedded in two different original images, which are denoted as Cases M1 and M2. Specifically, the image with the symbol “CAN YOU SEE IT” was provided by the authors of [6] (download in <https://github.com/vegarant/Invfool>). The original image with the symbol “HELLO NATURE” was produced (downloaded from <https://github.com/tensorlayer/DAGAN>), and denoted as Case M2 in this study. In Cases M1 and M2, there are two test images used to demonstrate the instability of the DAGAN network with respect to small structural changes. Next, to explore the performance of the DAGAN network in terms of adversarial attacks and small structural changes, the tiny perturbations derived from [6] were added into Cases M1 and M2 to generate Cases M3 and M4. Last, to test the DAGAN network in terms of anti-noising, the noise was superimposed to Cases M1 and M2 to obtain Cases M5 and M6. In our ablation study of ACID, we randomly selected one original image as M7 from the DAGAN test dataset (<https://github.com/tensorlayer/DAGAN>). Furthermore, Cases M8 and M9 were generated by applying the radial mask of a 20% subsampling rate on the M1 and M2 images, which were used to compare the performances of ACID and the classic Alternating Direction Method of Multipliers (ADMM)-net [22]. Regarding the stability of ACID, the tiny perturbation from ACID were added into M7, M1 and M2, and then the images with tiny perturbation were marked as M10, M11 and M12. The tiny perturbations from M11 and M12 are greater than the perturbations within M3 and M4 in terms of the  $L_2$ -norm. Except for M8 and M9, all the rest of the images were recovered from the k-space data collected

at a 10% subsampling rate using the Gaussian mask. All the images from the references of M1-M12 are shown in Fig. S4.

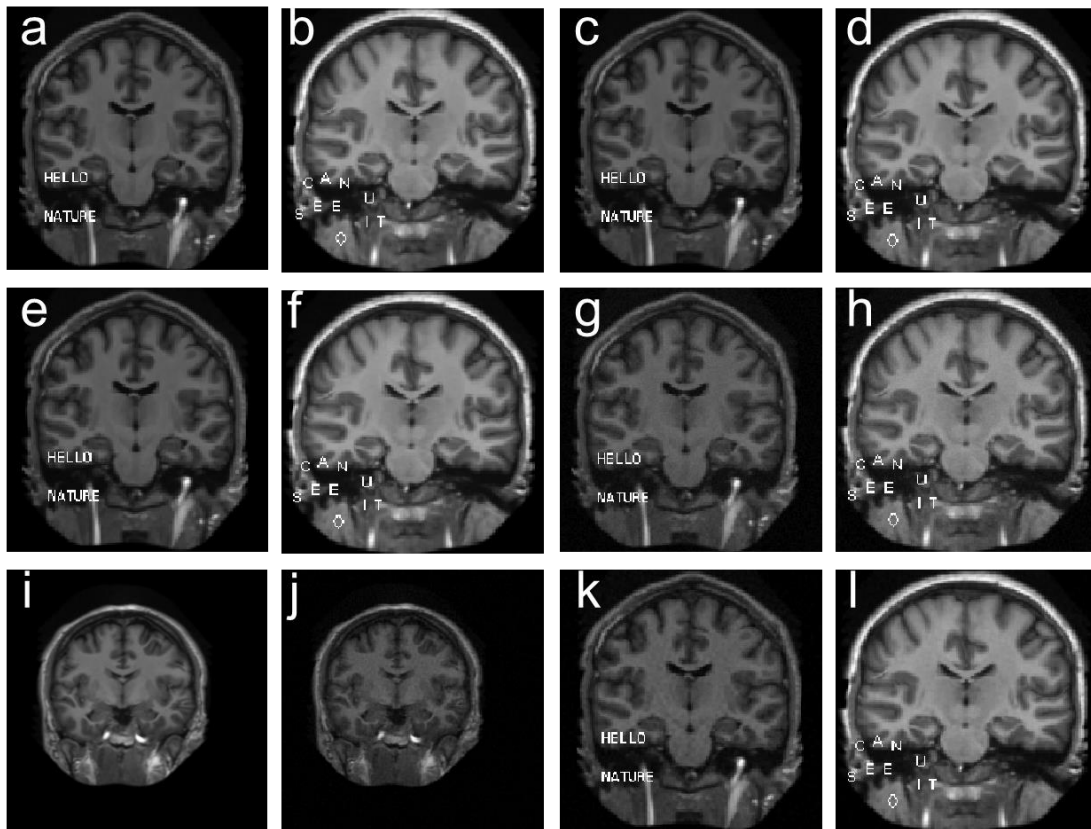


Fig. S4. Test images for showing the instability of neural networks. **a-l** represent the M1-M12 cases respectively.

## C. AUTOMAP Network

**C.1. Overall.** Proposed as a framework for image reconstruction, automated transform by manifold approximation (AUTOMAP) transfers sensor data to a high-quality reconstructed image with a mapping function between the sensor and the image domain [23]. The AUTOMAP demonstrated its advantages in various magnetic resonance imaging acquisition modes using the same architecture and hyperparameters. In this study, the AUTOMAP neural network was tested on the single-coil MRI with subsampled data. The trained AUTOMAP used in our experiments is provided by [6]. The architecture, training details, and test data of AUTOMAP are in the following sub-sections.

**C.2. Network Architecture.** The AUTOMAP [23] presents a framework for image reconstruction by translating sensor-domain signals into the image domain directly via domain-transform manifold learning. For MRI reconstruction, four subsampling strategies were applied to assess the performance of the AUTOMAP, which are Radon projection, spiral non-Cartesian Fourier, under-sampled Cartesian Fourier, and misaligned Fourier.

The AUTOMAP network takes a vectorized measurement data as input which is sub-sampled from the full-sampled k-space data. First, we can obtain the complex k-space data using the discrete Fourier transform on the MR images. Then, the subsampled k-space data is generated via subsampling mask. Next, these measurement data are reshaped into vectors. Last, the vectorized measurement data are fed into the AUTOMAP network. In this paper, the images with the size of  $128 \times 128$  and 60% subsampling rate are tested for MRI reconstruction. There are two fully connected layers in the first AUTOMAP network, which have 25,000 and  $128^2$  nodes, respectively. The activate function of the first fully connected layer is the hyperbolic tangent function, and the output of the second fully connected layer then subtracts the mean value of itself. Next, it is reshaped into a feature map with the same size of the reconstructed image. Furthermore, two convolutional layers are applied to extract essential features from their input data. Each of them contains 64 filters with a size of  $5 \times 5$  and the stride of  $1 \times 1$ . The activation function of the first convolution layers is a hyperbolic tangent function and the other is rectified linear unit (ReLU). The last convolutional layer has one filter with the size of  $7 \times 7$  and a stride of  $1 \times 1$ . The output of the network is the corresponding reconstruction image.

**C.3. Training Parameters.** The whole optimization problem of the AUTOMAP is defined as follow:

$$L_{AUTOMAP} = L_{rec} + \lambda_1 L_{fea} . \quad (S.1.2)$$

The loss function of AUTOMAP  $L_{AUTOMAP}$  consists of two terms, i.e.,  $L_{rec}$  and  $L_{fea}$ .  $L_{rec}$  is employed to evaluate the Euclidean distance between the predicted image provided by the AUTOMAP network and the ground truth image.  $L_{fea}$  is  $\ell_1$ -norm to constraint the feature maps produced by the activation function of the second convolutional layer.  $\lambda_1 > 0$  is to balance the two terms. The total loss function is optimized by the RMSProp algorithm with momentum 0 and decay 0.9 [23]. The learning rate is 0.00002 and the batch size is 100. The network is trained and stopped after 100 epochs.

**C.4. Training Data.** Selected in the MGH-USC HCP public dataset (<http://www.humanconnectomeproject.org/data/>) [24], there are 50,000 images from 131 subjects in total. Specifically, the training images are  $128 \times 128$  matrices, which were subsampled from the central part cropped from the original image. Meanwhile, all the training datasets were scaled to a given range. In the Fourier space, the subsampled measurement data was produced by a Poisson-disk mask of a 60% subsampling rate.

To improve the generalization of the AUTOMAP network, the data augmentation strategy was applied. 1.0% multiplicative noise was added to the input to promote manifold learning during the course of network training, and it is beneficial for the trained network learning robust representations from corrupted inputs. Actually, the specific additional noise distribution of the corruption process was not subject to the additive Gaussian noise during the

process of evaluation. The corresponding training datasets with the size of  $128 \times 128$  are cropped from original MR images by using four types of reflections. All the related codes were implemented in the TensorFlow framework with Python [6]. The trained weights were provided by the authors of [6].

**C.5. Testing Data.** To validate the instability of the AUTOMAP network, the symbol “♡” was added to the original MR image, which was also provided by the author [6]. This simple symbol was used to simulate small structural changes in the patient and then test the instability of the AUTOMAP network reconstruction. All the test data were downloaded from [6]. There are six test images for AUTOMAP [6], and the sixth image was selected as our test data, as shown in Fig. S5. The related reconstruction results are in the main body of the paper.

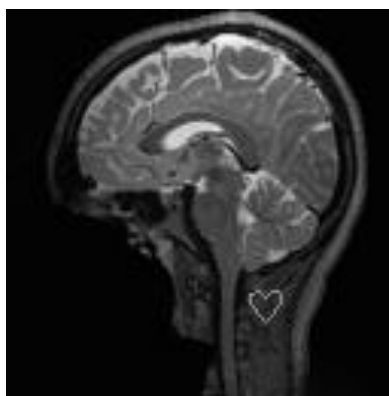


Fig. S5. Test image with a structural change for evaluation of the AUTOMAP stability.

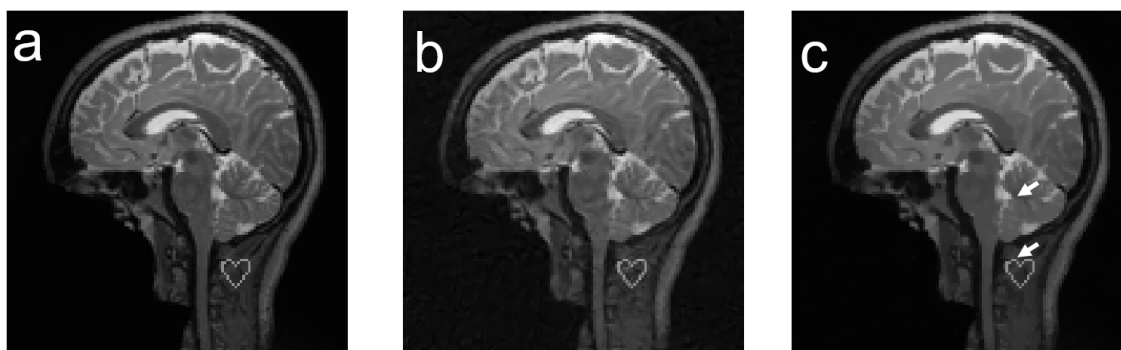


Fig. S6. ACID deep reconstruction with the embedded AUTOMAP network. **a** represents the original brain phantom, **b** and **c** represent the reconstructed results by AUTOMAP and ACID respectively.

**C.6. Reconstruction Results.** To demonstrate the advantages of ACID, a typical reconstruction network, AUTOMAP, was picked up as an example, and the reconstruction results are in Fig. S6. As shown in Fig. S6, ACID produced the image quality significantly better than that with AUTOMAP. PSNR was improved by ACID up to 36.0 dB, well above 27.8 dB of AUTOMAP. Also, SSIM of ACID reached 0.97 while the counterpart of AUTOMAP is only 0.73. It further demonstrates that ACID achieves better image quality than AUTOMAP.

## D. ADMM-net

**D.1 Overall.** Inspired by the traditional Alternating Direction Method of Multipliers (ADMM) iterative optimization algorithm for CS-based MRI [25], the ADMM-net defined over a data flow graph was first proposed in [22]. Regarding the training procedure, the network parameters (e.g. image shrinkage functions, transforms) are trained into an end-to-end architecture using the L-BFGS algorithm [26]. Regarding the testing step, it needs a similar computational overhead with the ADMM. However, there are no optimization parameters to be chosen in ADMM-net since these parameters are automatically learned during the training step. The superior experiments on MRI image reconstruction demonstrate the advantages over fast MRI imaging and higher reconstructed image quality. In this study, the ADMM-net is tested on the single-coil MRI with 20% subsampling and the trained weights are provided by the authors of [22]. The architecture, training parameters and test data of ADMM-net are summarized in the following sections. The workflow of ADMM-net is given in Fig. S7.

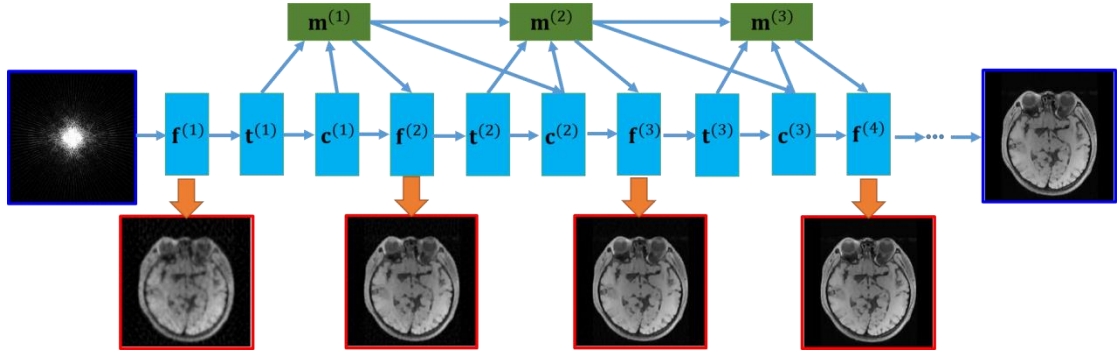


Fig. S7. The flowchart of the ADMM-net.  $f^{(k)}$ ,  $c^{(k)}$ ,  $t^{(k)}$  and  $m^{(k)}$  represent the construction layer, convolution layer, nonlinear transform layer, and multiplier update layer in the  $k$ -th stage.

**D.2. Network Architecture.** ADMM-net [22] is a classical unrolled iterative optimization algorithm for MRI reconstruction. Different from the traditional compressed sensing (CS) based methods [27] and data-driven based methods, ADMM-net can be trained end-to-end by incorporating a physic-guided model, and it achieves excellent performance in MR imaging with much less computational cost. The ADMM-net is derived from the ADMM algorithm via solving the sub-problem with deep learning networks. The CS-MRI model can be described as:

$$\operatorname{argmin}_{\mathbf{f}} \frac{1}{2} \|\mathbf{A}\mathbf{f} - \mathbf{p}^{(0)}\|_F^2 + \sum_{l=1}^L \lambda_l g(D_l(\mathbf{f})) \quad (\text{S.1.3})$$

where  $\mathbf{f} \in \mathcal{C}^N$  is the MR image to be reconstructed,  $\mathbf{p}^{(0)} \in \mathcal{C}^H$  denotes the under-sampled measurement data,  $\mathbf{A}$  is the Fourier translation based system matrix with an under-sampled mask,  $D_l$  represents the transform operation,  $g$  is the regularization function, and  $\lambda_l$  is the regularization parameter. By introducing  $t_l = D_l(\mathbf{f})$ ,  $l = 1, \dots, L$ , Eq. (S.1.3) is converted into the following

constraint optimization problem:

$$\operatorname{argmin}_{\mathbf{f}, \{t_l\}_{l=1}^L} \frac{1}{2} \|\mathbf{A}\mathbf{f} - \mathbf{p}^{(0)}\|_F^2 + \sum_{l=1}^L \lambda_l g(t_l), \quad t_l = D_l(\mathbf{f}), l = 1, \dots, L. \quad (\text{S.1.4})$$

Eq. (S.1.4) is a constraint programming procedure and it can be further converted into the following unconstrained problem

$$\operatorname{argmin}_{\mathbf{f}, \{t_l\}_{l=1}^L, \{\alpha_l\}_{l=1}^L} \frac{1}{2} \|\mathbf{A}\mathbf{f} - \mathbf{p}^{(0)}\|_F^2 + \sum_{l=1}^L \lambda_l g(t_l) - \sum_{l=1}^L \langle t_l - D_l(\mathbf{f}), \alpha_l \rangle + \frac{1}{2} \sum_{l=1}^L \gamma_l \|t_l - D_l(\mathbf{f})\|_F^2, \quad (\text{S.1.5})$$

where  $\alpha_l$  ( $l = 1, \dots, L$ ) are Lagrange multipliers and  $\gamma_l$  ( $l = 1, \dots, L$ ) are the corresponding penalty parameters. Eq. (S.1.5) can be solved using the ADMM algorithm [28] as the following three sub-problems:

$$\mathbf{f}^{(k+1)} = \operatorname{argmin}_{\mathbf{f}} \frac{1}{2} \|\mathbf{A}\mathbf{f} - \mathbf{p}^{(0)}\|_F^2 - \sum_{l=1}^L \langle t_l^{(k)} - D_l(\mathbf{f}), \alpha_l^{(k)} \rangle + \frac{1}{2} \sum_{l=1}^L \gamma_l \|t_l^{(k)} - D_l(\mathbf{f})\|_F^2, \quad (\text{S.1.6})$$

$$t_l^{(k+1)} = \operatorname{argmin}_{\{t_l\}_{l=1}^L} \lambda_l g(t_l) - \langle t_l - D_l(\mathbf{f}^{(k+1)}), \alpha_l \rangle + \frac{1}{2} \gamma_l \|t_l - D_l(\mathbf{f}^{(k+1)})\|_F^2, \quad l = 1, \dots, L, \quad (\text{S.1.7})$$

$$\alpha_l^{(k+1)} = \alpha_l^{(k)} + t_l^{(k+1)} - D_l(\mathbf{f}^{(k+1)}), \quad l = 1, \dots, L. \quad (\text{S.1.8})$$

Finally, these three sub-problems can be updated iteratively using deep neural blocks. Regarding the ADMM-net, the above optimization with one separate variable update can be generalized as four type layers: reconstruction layer ( $\mathbf{f}^{(k+1)}$ ), convolutional layer ( $\{D_l(\mathbf{f}^{(k+1)})\}_{l=1}^L$ ), non-linear layer ( $\{t_l^{(k+1)}\}_{l=1}^L$ ), and multiplier update layer ( $\{\alpha_l^{(k+1)}\}_{l=1}^L$ ). More details related to the construction and organization of the layers in ADMM-net can be referred to [22]. The ADMM-net takes the sub-sampled k-space data as the input and finally generates the reconstructed image through the iterative process.

**D.3. Training Parameters.** The ADMM-net adopts the normalized mean square error (NMSE) as the loss function to optimize the neural network. The image reconstructed from fully-sampled k-space data as the reference image and the corresponding under-sampling data in the k-space as the input. The loss function is defined as

$$L_{NMSE} = \frac{1}{N_1} \sum_{n_1=1}^{N_1} \frac{\sqrt{\|\hat{\mathbf{f}}_{n_1}(\theta) - \mathbf{f}_{n_1}\|_F^2}}{\sqrt{\|\mathbf{f}_{n_1}\|_F^2}}, \quad (\text{S.1.9})$$

where  $\hat{\mathbf{f}}_{n_1}$  and  $\mathbf{f}_{n_1}$  are the generated image from ADMM-net and the reference image (as the label), respectively.  $N_1$  is the number of training samples.  $\theta$  denote parameters needed to be optimized in ADMM-net. The L-BFGS algorithm is used to minimize the loss function  $L_{NMSE}$ .

**D.4. Training Data.** The ADMM-net is trained with brain and chest MR image datasets (<https://my.vanderbilt.edu/masi/workshops/>). For each dataset, 100 images were randomly selected for training and 50 images for testing. In our experiments, all the under-sampled k-space data were generated with the radial mask of a 20% subsampling rate, as shown in Fig. S8. All the codes are in MATLAB with Intel core i7-4790k CPU, and the training and testing datasets were downloaded from <https://github.com/yangyan92/Deep-ADMM-Net>.

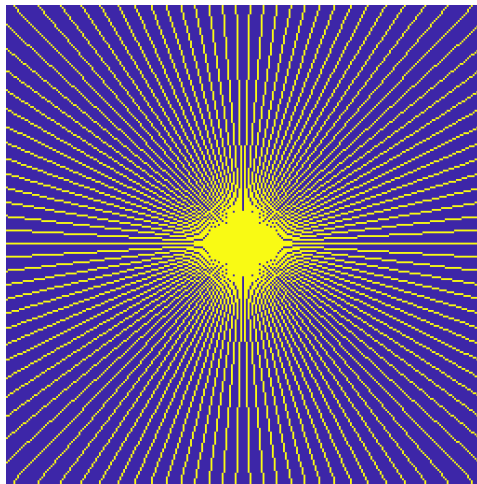


Fig. S8. Radial sampling mask of a 20% subsampling rate.

**D.5. Testing Data.** To validate the performance of ADMM-net about small structural changes, the same images as those in Fig. 2 in the main text of the paper with the symbols “CAN YOU SEE IT” and “HELLO NATURE” were employed with the radial mask of a 20% subsampling rate.

## II. CS Based Reconstruction Methods

### A. CS-inspired Reconstruction

**A.1. Overall.** To demonstrate the advantages of our ACID in terms of stability against the benchmark compressed sensing-based methods [29-32], the related experiments are performed, and the reconstruction results are provided using the established methods [33-35]. Since the total variation minimization (individual or combination) is popular in the image reconstruction field with consideration of sparsity prior, it is respectively chosen for CT and MRI image reconstruction in this study. The specific details are given in the following sub-sections.

**A.2. X-ray CT Reconstruction.** The re-weighting technique [36] combining both shearlets and TV in [37] and [38] was proposed to validate the stability in [6]. In this study, it served as a state-of-the-art CS-based comparison method

for CT. The details can be found in [38] and [6]. Here we only provide a brief summary as follows.

The mathematical model for this method is formulated as

$$\underset{\mathbf{f}}{\operatorname{argmin}} \frac{\omega}{2} \|\mathbf{A}\mathbf{f} - \mathbf{p}\|_F^2 + \sum_{j=1}^J \vartheta_j \|W_j \psi_j \mathbf{f}\|_1 + \operatorname{TGV}_\varrho(\mathbf{f}), \quad (\text{S.2.1})$$

where  $\vartheta_j$  represents the  $j$ -th balance factor,  $W_j$  is a diagonal matrix, and  $\psi_j$  represents the  $j$ -th subband from the corresponding shearlet transformation. The  $\operatorname{TGV}_\varrho(\mathbf{f})$  stands for the total generalized variation with the parameter  $\varrho$ .  $\operatorname{TGV}_\varrho(\mathbf{f})$  is combined with the components from first and second orders of total variation of the reconstructed image. Furthermore, the parameters  $\varrho$  is introduced to balance these two terms.  $\omega > 0$  is to balance data fidelity and regularization of sparsity prior.

To solve the optimization problem Eq. (S.2.1),  $\mathbf{d} = \psi' \mathbf{f}$  is introduced to represent the matrix format of  $\sum_{j=1}^J \psi_j \mathbf{f}$  and (S.2.1) is split into three sub-problems:

$$\{\mathbf{f}^{(k+1)}, \mathbf{d}^{(k+1)}\} = \underset{\mathbf{f}, \mathbf{d}}{\operatorname{argmin}} \frac{\omega}{2} \|\mathbf{A}\mathbf{f} - \mathbf{p}\|_F^2 + \|\mathbf{W}\mathbf{d}\|_1 + \frac{\omega_1}{2} \|\mathbf{d} - \psi' \mathbf{f} - \mathbf{b}^{(k)}\|_F^2 + \operatorname{TGV}_\varrho(\mathbf{f}), \quad (\text{S.2.2})$$

$$\mathbf{b}^{(k+1)} = \mathbf{b}^{(k)} + \psi' \mathbf{f}^{(k+1)} - \mathbf{d}^{(k+1)}, \quad (\text{S.2.3})$$

$$\mathbf{p}^{(k+1)} = \mathbf{p}^{(k)} + \mathbf{p} - \mathbf{A}\mathbf{f}^{(k+1)}. \quad (\text{S.2.4})$$

where  $W$  is the matrix format of  $\vartheta_j W_j$ . In Eqs. (S.2.2)-(S.2.4), the four variables are updated iteratively. First, the minimization problem Eq. (S.2.2) is optimized utilizing the multiple non-linear block Gauss-Seidel iterations [39]. Compared with the original re-weighting strategy in [36], the weights in  $W$  are not only updated after convergence to the solution of Eq. (S.2.2), but also the update weights are put into the following split process. This unique weight updating strategy is further described in [6]. In this work, the same strategy and the configuration in [6] were used (including the parameters, the number of iterations, etc.). Note that the number of iterations and the regularization parameters can be further optimized.

**A.3. MRI Reconstruction.** By extending the iteratively regularized Gauss–Newton method (IRGN) with variational penalties [40, 41], the total generalized variation (TGV) based IRGN (IRGN-TGV) was proposed in [42], and better reconstruction quality was achieved by combining estimation of image and coil sensitivities with TGV regularization. Indeed, the IRGN-TGV had superior noise suppression because of the TGV regularization. In addition, the IRGN-TGV approach can remove sampling artifacts arising from pseudorandom and radial sampling patterns. In this study, it was employed as a state-of-the-art to perform CS-based MRI experiments. Here we also only give a brief summary of this method.

Mathematically, MRI is a typical inverse problem with the sampling operator  $\mathbf{A}$  and the correspondingly k-space data  $\mathbf{p}$  from the receivers. Besides,

the spin density is given as  $\mathbf{h}$ , and  $\mathbf{c}$  represents the unknown set of coil sensitivities. For the current iteration index  $k$  with the given  $\mathbf{f}^{(k)} := (\mathbf{h}^{(k)}, \mathbf{c}^{(k)})$ , the solution  $\Delta\mathbf{f} := (\Delta\mathbf{h}, \Delta\mathbf{c})$  is sought to minimize the following objective function:

$$\underset{\Delta\mathbf{f}}{\operatorname{argmin}} \frac{1}{2} \|\mathbf{A}'(\mathbf{f}^{(k)})\Delta\mathbf{f} + \mathbf{A}(\mathbf{f}^{(k)}) - \mathbf{y}\|_F^2 + \frac{\alpha_k}{2} \|W_1(\mathbf{c}^{(k)} + \Delta\mathbf{c})\|_1 + \rho_k R(\mathbf{h}^{(k)} + \Delta\mathbf{h}). \quad (\text{S.2.5})$$

Given  $\alpha_k > 0$ ,  $\rho_k > 0$ , we have  $\mathbf{f}^{(k+1)} := \mathbf{f}^{(k)} + \Delta\mathbf{f}$ ,  $\alpha_{k+1} = q_a \alpha_k$  and  $\rho_{k+1} = q_b \rho_k$  and  $0 < q_a, q_b < 1$ .  $\mathbf{A}'(\mathbf{f}^{(k)})$  represents the derivative of  $\mathbf{A}(\mathbf{f}^{(k)})$  with respect to  $\mathbf{f}^{(k)}$ . The term  $W_1(\mathbf{c}^{(k)} + \Delta\mathbf{c})$  represents the penalty on the Fourier coefficients, and  $R$  is a regularization term. In the original IRGN method, the conventional  $L^2$  was considered. Since the TV regularization can introduce stair-casing artifacts and reduce the image quality if the penalty parameter is too large, the authors in [42] considered the second-order TGV (total generalization variation, TGV), which is a generalized TV. Compared with the conventional TV, the TGV avoids the stair-casing in regions of smooth signal changes, and improves the image quality [31, 43]. Therefore, the authors of [42] employed TGV in IRGN and then generated IRGN-TGV for MRI. More details are in [31] and the corresponding code can be downloaded from [https://www.tugraz.at/fileadmin/user\\_upload/Institute/IMT/files/misc/irgntv.zip](https://www.tugraz.at/fileadmin/user_upload/Institute/IMT/files/misc/irgntv.zip). The parameters can be further tuned, depending on experimental designs [31].

## B. Dictionary Learning Based Reconstruction

**B.1. Overall.** As a successful example, the dictionary learning-based methods were developed for tomographic reconstruction, including MRI [44-46], Optical Coherence Tomography [47-50] and CT [34, 51-53]. Dictionary learning based reconstruction methods explored the intrinsic properties using the trained dictionary with initial reconstruction results. The reconstruction process is usually divided into the two steps: dictionary learning and image reconstruction. Without loss of generality, we compare the dictionary learning-based reconstruction method with our proposed ACID for CT and MRI.

**B.2. Dictionary Learning Model.** A number of image patches  $\mathbf{f}_{i_d} \in \mathcal{R}^{S \times S}$ ,  $i_d = 1, \dots, I_d$ , are extracted from the training datasets  $\mathbf{f}$ , and  $s$  represents the size of image patches. The set of  $\mathbf{f}_{i_d}$ ,  $i_d = 1, \dots, I_d$  are employed to train the global dictionary  $\mathbf{D}_{ic} \in \mathcal{R}^{S \times T_d}$ , where  $S = s \times s$  and  $T_d$  is the number of atoms. The aim of dictionary learning is to search representation coefficients with sparse-level space constrained by  $\mathbf{q} \in \mathcal{R}^{T_d \times I_d}$  based on the dictionary  $\mathbf{D}_{ic}$ . It can be explained by solving the following optimization expression:

$$\{\mathbf{D}_{ic}^*, \mathbf{q}^*\} = \underset{\mathbf{D}_{ic}, \mathbf{q}}{\operatorname{argmin}} \frac{1}{2} \sum_{i_d=1}^{I_d} \|\mathbf{f}_{i_d} - \mathbf{D}_{ic} \mathbf{q}_{i_d}\|_2^2 \quad \text{s.t.} \quad \|\mathbf{q}_{i_d}\|_0 \leq L_{dl}, \quad (\text{S.2.6})$$

where  $L_{dl}$  is the sparsity level of dictionary learning,  $\|\cdot\|_0$  represents the quasi- $l_0$  norm,  $\mathbf{q}_{i_d} \in \mathcal{R}^{T_d \times 1}$  represents sparse representation coefficients for the  $i_d$ -th image patch. Eq. (S.2.6) is a constrained problem, and it is equivalent to the following unconstrained problem under a certain condition:

$$\{\mathbf{D}_{ic}^*, \mathbf{q}^*\} = \underset{\mathbf{D}_{ic}, \mathbf{q}}{\operatorname{argmin}} \left( \sum_{i_d=1}^{I_d} \left( \frac{1}{2} \|\mathbf{f}_{i_d} - \mathbf{D}_{ic} \mathbf{q}_{i_d}\|_2^2 + h_{i_d} \|\mathbf{q}_{i_d}\|_0 \right) \right), \quad (\text{S.2.7})$$

where  $h_{i_d}$  represents a Lagrange multiplier, which needs to be optimized.

Furthermore, Eq. (S.2.7) can be solved by an alternating minimization scheme. First, we need to update  $\mathbf{q}_{i_d}$  with a fixed dictionary  $\mathbf{D}_{ic}$ ,

$$\mathbf{q}^* = \operatorname{argmin}_{\mathbf{q}} \sum_{i_d=1}^{I_d} \left( \frac{1}{2} \|\mathbf{f}_{i_d} - \mathbf{D}_{ic} \mathbf{q}_{i_d}\|_2^2 + h_{i_d} \|\mathbf{q}_{i_d}\|_0 \right). \quad (\text{S.2.8})$$

Eq. (S.2.8) can be solved using the matching pursuit (MP)[54] or orthogonal matching pursuit (OMP) algorithm [55]. Then, we can update the dictionary with a fixed sparse representation coefficients  $\mathbf{q}$ . Many methods can be employed to train the dictionary  $\mathbf{D}_{ic}$ , such as K-SVD [56], discriminate K-SVD [57], coupled dictionary training [58], online learning technique [59] and online robust learning [60]. In this study, the K-SVD was employed.

**B.3. Dictionary Learning Based CT Reconstruction.** The conventional dictionary learning was first employed to magnetic resonance (MR) reconstruction from under-sampled k-space data [44]. Then, the dictionary learning was utilized to low-dose CT imaging in our previous work [34], few-view CT reconstruction [29] and material decomposition [61]. In this study, we only consider the dictionary learning-based sparse data CT reconstruction. The mathematical model of dictionary learning-based CT reconstruction can be written as follows:

$$\operatorname{argmin}_{\mathbf{f}, \mathbf{q}} \frac{1}{2} \|\mathbf{p}^{(0)} - \mathbf{A}\mathbf{f}\|_2^2 + \varsigma \sum_{i_d=1}^{I_d} \left( \frac{1}{2} \|\wp_{i_d} \mathbf{f} - \mathbf{D}_{ic} \mathbf{q}_{i_d}\|_2^2 + h_{i_d} \|\mathbf{q}_{i_d}\|_0 \right), \quad (\text{S.2.9})$$

where  $\varsigma > 0$  represents the regularization penalty parameter.  $\wp_{i_d}$  is an operator to extract  $i_d$ -th image patch from  $\mathbf{f}$ . Regarding the optimization of Eq. (S.2.9), there are many strategies to reach such a goal. Here, the split-Bregman method is used to obtain its solution. First, we introduce a new variable  $\mathbf{b}$  to replace  $\mathbf{f}$  and Eq. (S.2.9) can be converted into the following constraint programming problem

$$\operatorname{argmin}_{\mathbf{f}, \mathbf{q}} \frac{1}{2} \|\mathbf{p}^{(0)} - \mathbf{A}\mathbf{f}\|_2^2 + \varsigma \sum_{i_d=1}^{I_d} \left( \frac{1}{2} \|\wp_{i_d} \mathbf{b} - \mathbf{D}_{ic} \mathbf{q}_{i_d}\|_2^2 + h_{i_d} \|\mathbf{q}_{i_d}\|_0 \right), \text{ s. t. }, \mathbf{f} = \mathbf{b}. \quad (\text{S.2.10})$$

To optimize Eq. (S.2.10), it can be further converted into

$$\operatorname{argmin}_{\mathbf{f}, \mathbf{b}, \mathbf{q}, \boldsymbol{\chi}} \frac{1}{2} \|\mathbf{p}^{(0)} - \mathbf{A}\mathbf{f}\|_2^2 + \varsigma \sum_{i_d=1}^{I_d} \left( \frac{1}{2} \|\wp_{i_d} \mathbf{b} - \mathbf{D}_{ic} \mathbf{q}_{i_d}\|_2^2 + h_{i_d} \|\mathbf{q}_{i_d}\|_0 \right) + \frac{\varsigma_1}{2} \|\mathbf{f} - \mathbf{b} - \boldsymbol{\chi}\|_2^2, \quad (\text{S.2.11})$$

where  $\varsigma_1 > 0$  represents the coupling factor, and  $\boldsymbol{\chi}$  is the error feedback. In Eq. (S.2.11), there are four variables  $\mathbf{f}$ ,  $\mathbf{b}$ ,  $\mathbf{q}$  and  $\boldsymbol{\chi}$ . It can be split into the following three sub-problems:

$$\operatorname{argmin}_{\mathbf{f}} \frac{1}{2} \|\mathbf{p}^{(0)} - \mathbf{A}\mathbf{f}\|_2^2 + \frac{\varsigma_1}{2} \|\mathbf{f} - \mathbf{b}^{(k)} - \boldsymbol{\chi}^{(k)}\|_2^2, \quad (\text{S.2.12})$$

$$\operatorname{argmin}_{\mathbf{b}, \mathbf{q}} \sum_{i_d=1}^{I_d} \left( \frac{1}{2} \|\wp_{i_d} \mathbf{b} - \mathbf{D}_{ic} \mathbf{q}_{i_d}\|_2^2 + h_{i_d} \|\mathbf{q}_{i_d}\|_0 \right) + \frac{\varsigma_1}{2} \|\mathbf{f}^{(k+1)} - \mathbf{b} - \boldsymbol{\chi}^{(k)}\|_2^2, \quad (\text{S.2.13})$$

$$\boldsymbol{\chi}^{(k+1)} = \boldsymbol{\chi}^{(k)} - \tau_d (\mathbf{f}^{(k+1)} - \mathbf{b}^{(k+1)}), \quad (\text{S.2.14})$$

where  $\tau_d > 0$  represents the step length and it was set to 1 in this study. Regarding Eq. (S.2.12), it is solved by using the separable surrogate method [62]

$$\mathbf{f}_{j_1 j_2}^{(k+1)} = \mathbf{f}_{j_1 j_2}^{(k)} - \frac{[\mathbf{A}^T (\mathbf{A}\mathbf{f}^{(k)} - \mathbf{p}^{(0)})]_{j_1 j_2} + \varsigma_1 [\mathbf{f}^{(k)} - \mathbf{b}^{(k)} - \boldsymbol{\chi}^{(k)}]_{j_1 j_2}}{[\mathbf{A}^T \mathbf{A} + \varsigma_1]_{j_1 j_2}}, \quad (\text{S.2.15})$$

where  $[\cdot]_{j_1 j_2}$  represents the  $(j_1, j_2)^{th}$  pixel in the matrix. In practice, Eq. (S.2.15)

was performed using two steps:

$$\mathbf{f}_{j_1 j_2}^{(k+\frac{1}{2})} = \mathbf{f}_{j_1 j_2}^{(k)} - \frac{[\mathbf{A}^T(\mathbf{A}\mathbf{f}^{(k)} - \mathbf{p}^{(0)})]_{j_1 j_2}}{[\mathbf{A}^T\mathbf{A} + \varsigma_1]_{j_1 j_2}}, \quad (\text{S.2.16})$$

and

$$\mathbf{f}_{j_1 j_2}^{(k+1)} = \mathbf{f}_{j_1 j_2}^{(k+\frac{1}{2})} - \frac{\varsigma_1[\mathbf{f}^{(k)} - \mathbf{b}^{(k)} - \boldsymbol{\chi}^{(k)}]_{j_1 j_2}}{[\mathbf{A}^T\mathbf{A} + \varsigma_1]_{j_1 j_2}}. \quad (\text{S.2.17})$$

In fact, the number of iterations for  $\mathbf{f}_{j_1 j_2}^{(k+\frac{1}{2})}$  in Eq. (S.2.16) needs to be set to a good number (it was set as 10 in this study), and then  $\mathbf{f}_{j_1 j_2}^{(k+1)}$  is updated. Since  $\varsigma_1$  is specific to scanning geometry, it is normalized into a new parameter  $\gamma_1$  so that  $\varsigma_1 = \gamma_1 \|\mathbf{A}^T\mathbf{A}\|$ ; that is, we only need to select a geometrically-invariant  $\gamma_1$ . Regarding the optimization of Eq. (S.2.13), it is a typical dictionary learning-based signal recovery problem, and there are a large number of algorithms to solve this problem [56, 58]. To control the image recovery via dictionary learning, the parameters of sparsity level  $L_{dl}$  and the precision level  $\zeta$  should be chosen; for more details, see our previous studies [29, 34, 63].

**B.4. Dictionary Learning Based MRI Reconstruction.** The conventional dictionary learning methods are common for magnetic resonance (MR) reconstruction [44, 64-66]. In this study, the dictionary learning-based MRI (DLMRI) in [44] was employed to highlight the advantages of the ACID with built-in DAGAN and TV. Regarding the reconstruction process of DLMRI, it is similar to the process for CT reconstruction. It is also divided into the two steps: dictionary learning and image updating. Regarding the dictionary learning step, both MRI and CT are the same except that training images are different. Again, the dictionary used in CT reconstruction was trained from FBP results or updated results within the iteration process. In contrast, the dictionary utilized in MRI was trained from the inverse Fourier transform results. Regarding the image updating step, it is not necessary to update the image based on the fast Fourier transform. More details can be found in [44].

**B.5. Experimental Results.** To validate the outperformance of ACID in comparison with the dictionary learning-based CT reconstruction method (DLCT), we repeated the experiments design for the Cases C1 and C2. Here, we adopt the FBP method to reconstruct images. Then, the FBP results were employed to train the dictionaries. In this study, only  $10^4$  image patches were extracted from FBP images to train the dictionary by the K-SVD algorithm. The size of extracted image patches was set to  $6 \times 6$ . The dictionary  $\mathbf{D}_{ic}$  is overcomplete, and it can benefit the sparsity level enforcement. The number of atoms was set as 512. The sparsity level  $L_{dl}$  in the dictionary training can be set empirically, and it was chosen as 6. The number of iterations for the training dictionary was set to 100.

Note that the total variation is still treated as the compressed sensing-based sparsity for the built-in component in the ACID. Here, the parameters of  $\gamma_1$ ,  $L_{dl}$  and  $\zeta$  in DLCT were set to 0.22, 8 and 0.06, respectively. The number of outer iterations was set to 200. The implementation environment for training and reconstruction is the same as Ell-50. Specifically, the computational costs of dictionary training and reconstruction consume 139 and 561 seconds. However, the whole ACID with the built-in Ell-50 consumes about 70.5 seconds. In other words, the ACID is remarkably faster than the DLCT method.

The reconstruction results from DLCT and ACID with C1 and C2 are in Fig. S9. It is observed that DLCT provides higher image quality than that obtained by the CS method. However, it is still worse than those obtained by the ACID. Besides, the proposed ACID method obtains better image edges and avoids the blurred artifacts compared with the DLCT method. Especially, the insert texts in DLCT results (i.e., “CAN U SEE IT” and “A BIRD?”) are very blurry, and they are failed to be discriminated. These texts are clearly observed in ACID results. Regarding small features (i.e., the symbol “♡”), they are totally missing in the DLCT result. However, they were still recovered by the ACID. In terms of quantitative assessment, our proposed ACID obtained the best results remarkably. More details for codes and test data are on <https://zenodo.org/record/4540511>.

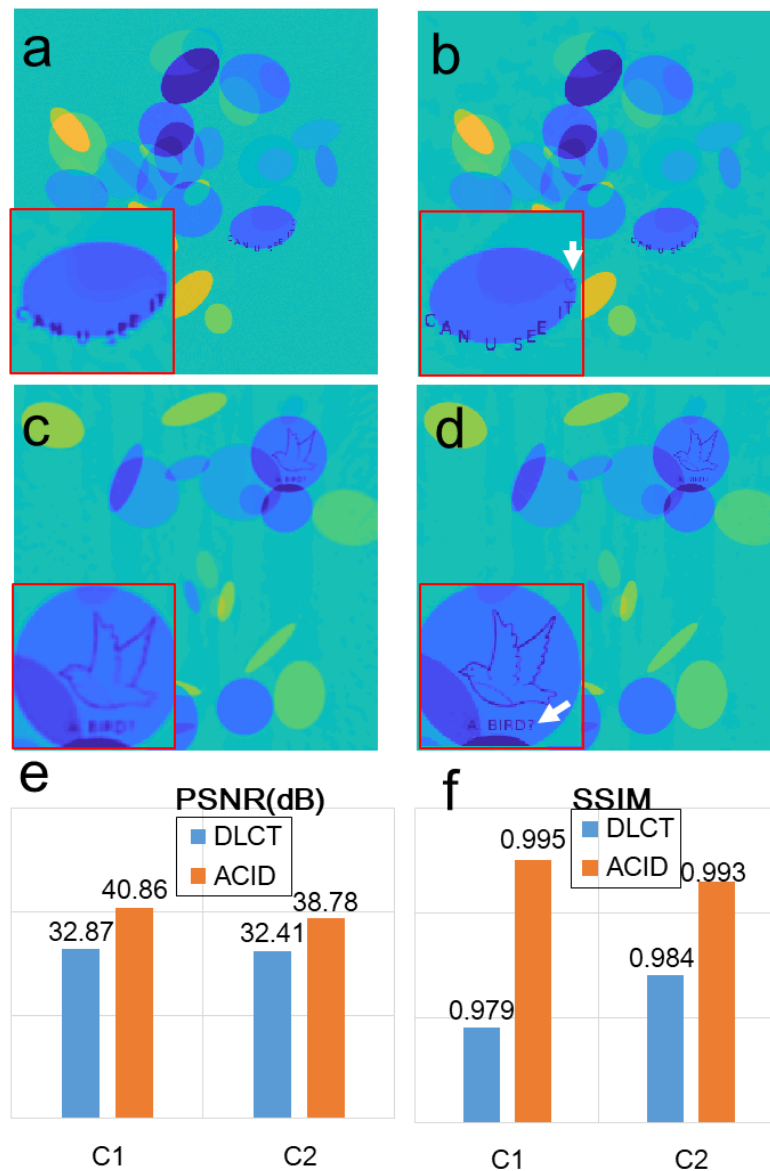


Fig. S9. Comparison study on the DLCT and ACID methods. **a** and **c**, **b** and **d** are reconstructed results from DLCT and ACID, respectively. **e** and **f** represent the quantitative results in terms of PSNR and SSIM.

To show the advantages of ACID with the built-in DAGAN, the reconstruction results in the M2 case from ACID and DLMRI are given in Fig. S10. The DLMRI obtained higher image quality than that obtained by the conventional CS method in the main text. However, it is still worse than those obtained by the ACID. Besides, the proposed ACID method obtained better image edges and avoided blurry artifacts compared with the DLMRI method. Especially, the insert texts in DLCT results (i.e., “CAN U SEE IT”) is very blurry, and they could not be discriminated. These texts are clearly observed in the ACID results. Small symbol was totally blurred in DLMRI result, which was still recovered by ACID. In terms of quantitative assessment, our proposed ACID obtained better results than those achieved by DLMRI method. The MATLAB code of the MRIDL method can be downloaded from <http://www.ifp.illinois.edu/~yoram/DLMRI-Lab/DLMRI.html>. The reconstruction parameters within DLMRI were optimized. Regarding the computational cost, DLMRI took 606.3 seconds, which is higher than that of CS reconstruction methods in the main text (i.e., 127.8 seconds). Our proposed ACID only took 9.2 seconds.

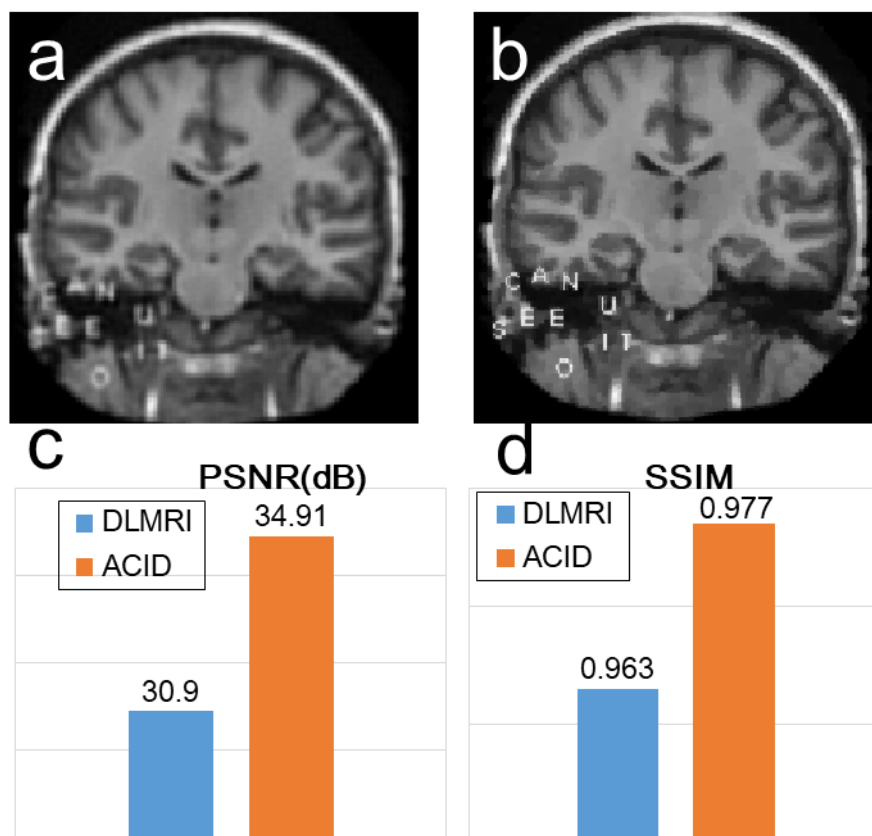


Fig. S10. Comparison study on the DLMRI and ACID methods. **a** and **b** are the reconstructed results from DLCT and ACID respectively. **c** and **d** represent the quantitative results in terms of PSNR and SSIM.

### III. ACID Architecture & Adversarial Attacks

#### A. ACID Implementation

For an implementation of the whole ACID system, it is considered as an iterative framework and listed in Algorithm 1. In the whole ACID framework, we need to have input data  $\mathbf{p}^{(0)}$ , a neural network  $\Phi$  and a system matrix  $\mathbf{A}$ . Then, we should specify the stopping condition; i.e., the maximum number of iterations  $K$ . Finally, the parameters  $\xi$ ,  $\lambda$  and  $\mu$  should be given to control the iterative process and the regularization strength, all of which can be empirically picked up. In fact, the parameter  $\mu$  is always set to 0 in this study. When  $k=1$ , we need to compute  $\Phi(\mathbf{p}^{(0)})$  and then normalize  $\Phi(\mathbf{p}^{(0)})$ . The goal of the normalization operator is to facilitate the adjustment of the regularization parameters for different applications. Then, we obtain the update  $\mathbf{b}^{(1)}$  using Eq. (17) in the main body of this paper. Next,  $\mathbf{f}^{(1)}$  is updated by de-normalizing  $\mathbf{b}^{(1)}$ . When  $1 < k < K+1$ , we need to compute the residual data by  $\mathbf{p}^{(k+1)} = \frac{\lambda(\mathbf{p}^{(0)} - \mathbf{A}\mathbf{f}^{(k)})}{1 + \lambda + \mu}$ . Since the residual data is not in the dynamic range of the original data, the residual data should be normalized into the original range to make sure the efficiency of the neural network (Line #9 in Algorithm 1). After the neural network predicts a residual image, the de-normalization operator should be applied on the prediction to ensure the consistency of the reconstruction results. Then,  $\mathbf{f}^{(k)} + \frac{1 + \mu\rho}{\lambda\rho} \Phi(\mathbf{p}^{(k+1)})$  is normalized and fed to the compressed sensing based regularization module to encourage image sparsity. Finally, we obtain the update image  $\mathbf{f}^{(k+1)}$  after the de-normalization. More details on our codes and other materials can be found on the public link: <https://zenodo.org/record/4540511>.

Algorithm 1. Pseudocode of the ACID workflow.

---

Input: Data  $\mathbf{p}^{(0)}$ , neural network  $\Phi$ , system matrix  $\mathbf{A}$ , maximum number of iterations  $K$ , auxiliary parameters  $\xi, \lambda, \mu = 0$ , and  $k=1$ ;

1. If  $k < K+1$  do
2.   if  $k=1$  do
3.     Computing  $\Phi(\mathbf{p}^{(0)})$ ;
4.     Normalizing the  $\Phi(\mathbf{p}^{(0)})$ ;
5.     Updating  $\mathbf{b}^{(1)}$  using Eq. (17) where the normalized  $\Phi(\mathbf{p}^{(0)})$  is treated as the input;
6.     Updating  $\mathbf{f}^{(1)}$  by de-normalizing  $\mathbf{b}^{(1)}$ ;
7.   else do
8.     Computing residual data using  $\mathbf{p}^{(k+1)} = \frac{\lambda(\mathbf{p}^{(0)} - \mathbf{A}\mathbf{f}^{(k)})}{1 + \lambda + \mu}$ ;
9.     Normalizing the residual data  $\mathbf{p}^{(k+1)}$  into the input range of neural network;
10.    Inputting the normalized data into the neural network  $\Phi$  and obtaining  $\Phi(\mathbf{p}^{(k+1)})$ ;
11.    De-normalizing  $\Phi(\mathbf{p}^{(k+1)})$ ;
12.    Normalizing  $\mathbf{f}^{(k)} + \frac{1 + \mu\rho}{\lambda\rho} \Phi(\mathbf{p}^{(k+1)})$
13.    Updating  $\mathbf{b}^{(k+1)}$  utilizing Eq. (17);
14.    Updating  $\mathbf{f}^{(k+1)}$  by de-normalizing  $\mathbf{b}^{(k+1)}$ ;
15.   end
16. end

---

---

17. return  $\mathbf{f}^{(K)}$

Output: Reconstructed image  $\mathbf{f}^{(K)}$

---

## B. Adversarial Attacks

**B.1. Attacking Model.** In the image reconstruction field, the continuous imaging system [67, 68] can be discretized into a linear model

$$\mathbf{p} = \mathbf{A}\mathbf{f}, \quad \mathbf{A} \in \mathbb{R}^{m \times N}, \quad (\text{S.3.1})$$

where  $\mathbf{p}$  represents collected data,  $m$  and  $N$  defines the size of the system matrix  $\mathbf{A}$ . The aim of image reconstruction is to reconstruct  $\mathbf{f}$  from  $\mathbf{p}$  for a given system matrix  $\mathbf{A}$ .  $\mathbf{A}$  is the Fourier transform for MRI and the Radon transform for CT [69].

To assess the stability of image reconstruction, it is necessary to compute a tiny perturbation or adversarial attack [6, 70, 71]. In this context, the researchers [6] first computed a tiny perturbation for the following model (S.3.1):

$$\text{Reconstruct } \mathbf{f} \text{ from } \mathbf{p} = \mathbf{A}\mathbf{f}, \quad \mathbf{A} \in \mathbb{R}^{m \times N}. \quad (\text{S.3.2})$$

For a well-trained neural network  $\Phi: \mathbb{R}^m \rightarrow \mathbb{R}^N$  to solve Eq. (S.3.2), similar to the adversarial attack in image classification [72], we compute the instabilities by formulating the following problem based on [6]

$$\hat{\mathbf{e}}(\mathbf{f}) \in \underset{\mathbf{e}}{\text{argmin}} \|\mathbf{e}\|, \quad \text{s.t. } \|\Phi(\mathbf{p} + \mathbf{A}\mathbf{e}) - \Phi(\mathbf{p})\| \geq \epsilon. \quad (\text{S.3.3})$$

With Eq. (S.3.3),  $\mathbf{p} = \mathbf{A}\mathbf{f}$  cannot always be true when  $\epsilon > 0$ . One can consider the constrained Lasso variant of (S.3.3) as follows:

$$\hat{\mathbf{e}}(\mathbf{f}) \in \underset{\mathbf{e}}{\text{argmax}} \|\Phi(\mathbf{p} + \mathbf{A}\mathbf{e}) - \Phi(\mathbf{p})\|, \quad \text{s.t. } \|\mathbf{e}\| \leq \sigma \quad (\text{S.3.4})$$

There is no infeasibility issue for Eq. (S.3.4). An unconstrained Lasso inspired version of Eq. (S.3.4) is given by

$$\mathbf{e}^*(\mathbf{p}) \in \underset{\mathbf{e}}{\text{argmax}} \frac{1}{2} \|\Phi(\mathbf{p} + \mathbf{A}\mathbf{e}) - \Phi(\mathbf{p})\|_2^2 - \frac{\gamma}{2} \|\mathbf{e}\|_2^2. \quad (\text{S.3.5})$$

With  $\Phi(\mathbf{p}) = l(\mathbf{f})$ , Eq. (S.3.5) is further converted to

$$\mathbf{e}^*(\mathbf{p}) \in \underset{\mathbf{e}}{\text{argmax}} \frac{1}{2} \|\Phi(\mathbf{p} + \mathbf{A}\mathbf{e}) - l(\mathbf{f})\|_2^2 - \frac{\gamma}{2} \|\mathbf{e}\|_2^2, \quad (\text{S.3.6})$$

where  $l(\mathbf{f}) = \mathbf{f}$  for image-domain post-processing [73-75] and  $l(\mathbf{f}) = \Phi(\mathbf{A}\mathbf{f})$  with the end-to-end network (such as AUTOMAP [23] and iRadonMap [76]). Note that Eq. (S.3.6) works in the image domain to find perturbations. One generates a reconstructed image using an easy way and then compares the original image with a perturbed one to determine whether the perturbed image is acceptable/unacceptable. Now, we describe the details on how to generate perturbations for a single neural network and the whole ACID system, respectively.

## B.2. Stability with Respect to Tiny Perturbation to a Selected Network.

Since the neural network  $\Phi: \mathbb{R}^m \rightarrow \mathbb{R}^N$  is a non-linear function. It is difficult to

reach for a global maximum for Eq. (S.3.6). Here, we use the same strategy in [6] to search for tiny perturbations. In other words, our goal is to reach the local maxima of Eq. (S.3.6) using a gradient search method. Especially, one defines the following objective function:

$$D_p^l(\mathbf{e}) = \frac{1}{2} \|\Phi(\mathbf{p} + \mathbf{A}\mathbf{e}) - l(\mathbf{f})\|_2^2 - \frac{\gamma}{2} \|\mathbf{e}\|_2^2, \quad (\text{S.3.7})$$

Regarding the optimization of Eq.(S.3.7), the gradient ascent search is a very common method [77]. For an iterative solution to (S.3.7), except the weighting factor  $\gamma$ , there are two parameters (i.e.,  $\tau$  and  $\vartheta$ ) to be chosen, which control the perturbation  $\mathbf{e}$ . Algorithm 2 summarized the flowchart to generate tiny perturbations for a single neural network with a random initialization  $\mathbf{e}_0$ , where  $t_1$  represents a scaling factor to control the range of an input image. The gradient of  $D_p^l(\mathbf{e})$  with respect to  $\mathbf{e}$  can be given as

$$\nabla_{\mathbf{e}} D_p^l(\mathbf{e}) = \mathbf{A}^T \nabla_{\mathbf{u}_1} z(\mathbf{u}_1) - \gamma \mathbf{e}, \quad z(\mathbf{u}_1) := \frac{1}{2} \|\Phi(\mathbf{u}_1) - l(\mathbf{f})\|_2^2, \quad (\text{S.3.8})$$

where  $\mathbf{u}_1 = \mathbf{p} + \mathbf{A}\mathbf{e}$ ,  $\nabla_{\mathbf{u}_1} z(\mathbf{u}_1)$  can be implemented as a backpropagation method, and  $\mathbf{A}^T$  represents the transpose of  $\mathbf{A}$ .

For generating such tiny perturbations via gradient ascent search, the learning rate ( $\vartheta > 0$ ) needs to be optimized. In this study, we search for tiny perturbations guided by the experimental results in [6]. Note that Algorithm 2 needs to be modified slightly for CT reconstruction due to the adjoint operator corresponding to a discretization of the filtered backprojection (FBP) method, and more details on the experiments generating tiny perturbations for X-ray CT are given in [6]. The discretization of FBP in our study was done using MATLAB R2017b.

---

Algorithm 2 Searching tiny perturbation in inverse problems.

---

Input: Image  $\mathbf{f}$ , neural network  $\Phi$ , system matrix  $\mathbf{A}$ , maximum number of iterations  $K_1$   
Initialization:  $\mathbf{p} \leftarrow \mathbf{A}\mathbf{f}$ ,  $\mathbf{v}^{(0)} \leftarrow \mathbf{0}$ ,  $i \leftarrow 0$ ,  $\gamma, \tau > 0$  and  $\vartheta > 0$ ,  $\mathbf{e}_0$ ,  $D_p^l(\mathbf{e})$  is defined by Eq. (S.3.7)  
while  $i \leq K_1$  do  
     $\mathbf{v}^{(i+1)} \leftarrow \tau \mathbf{v}^{(i)} + \vartheta \nabla_{\mathbf{e}} D_p^l(\mathbf{e}^{(i)})$   
     $\mathbf{e}^{(i+1)} = \mathbf{e}^{(i)} + \mathbf{v}^{(i+1)}$   
     $i = i + 1$   
return  $\mathbf{e}^{(K_1)}$   
Output: Perturbation  $\mathbf{e}^{(K_1)}$

---

**B.3. Stability with Respect to Tiny Perturbation to Our ACID.** The iterative process of ACID is to find the optimized solution in the intersection of in the intersection of (a) the space of data-driven priors, (b) the space of sparse images, and (c) the space of solutions satisfying the measurement, as shown in Fig. S11. With a tiny perturbation to our proposed ACID workflow, the feed-forward propagation of the perturbation is illustrated in Fig. S12. Specifically, the formula of Eq. (S.3.7) is converted to

$$D_{\mathbf{p}^{(0)}}^l(\mathbf{e}) = \frac{1}{2} \|\hat{\mathbf{f}}(\mathbf{p}, \mathbf{p}^{(0)}) - l(\mathbf{f})\|_2^2 - \frac{\gamma}{2} \|\mathbf{e}\|_2^2, \quad (\text{S.3.9})$$

where  $\hat{f}$  is different from  $f$  as computed by the neural network and stabilized in the ACID framework.  $\hat{f}(\mathbf{p}, \mathbf{p}^{(0)})$  is the solution minimizing the following objective function (for more details, please see Section IV in this **SI**):

$$\operatorname{argmin}_{\mathbf{p}, \mathbf{f}} \frac{1}{2} \|\Phi(\mathbf{A}\mathbf{f} + \mathbf{p}) - \mathbf{f}\|_2^2 + \frac{\lambda}{2} \|\mathbf{p}^{(0)} - \mathbf{A}\mathbf{f} - \mathbf{p}\|_2^2 + \frac{\mu}{2} \|\mathbf{p}\|_2^2 + \xi \|\mathbf{H}\mathbf{f}\|_1. \quad (\text{S.3.10})$$

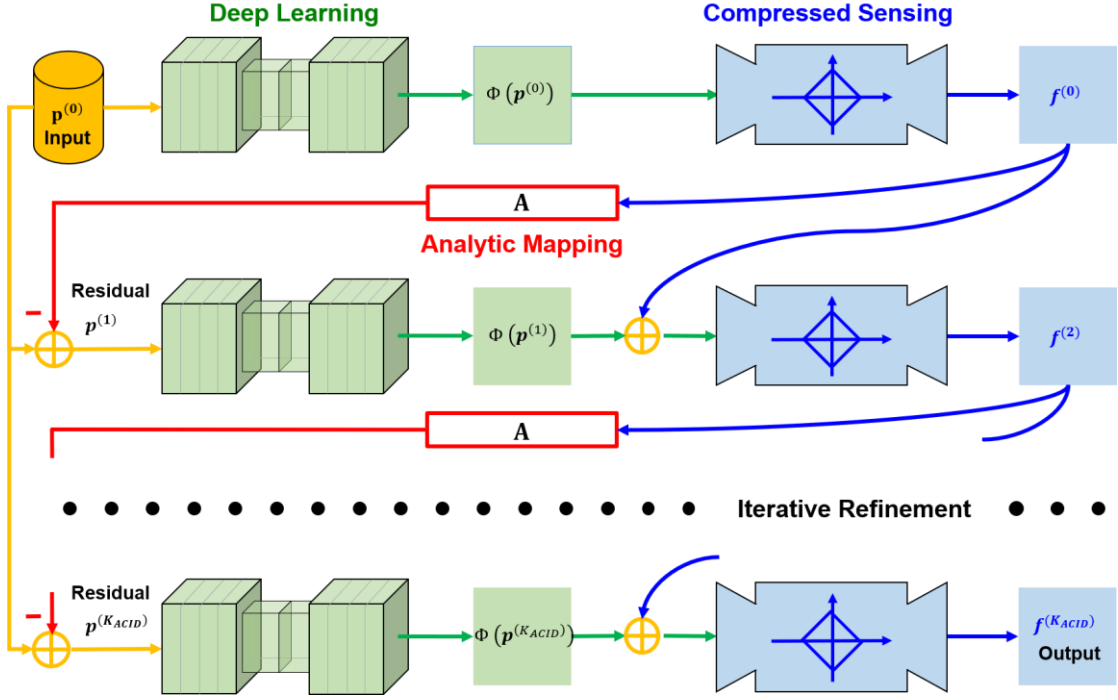


Fig. S11. ACID architecture for stabilizing deep tomographic image reconstruction. ACID consists of the following components: deep reconstruction, compressed sensing-based sparsity promotion, analytic mapping and iterative refinement.  $\mathbf{p}^{(0)}$  is original tomographic data, and  $\mathbf{p}^{(k_{ACID})}$ ,  $k_{ACID}=1, 2, 3, \dots, K_{ACID}$ , represents an estimated residual dataset in the  $k_{ACID}$ <sup>th</sup> iteration between  $\mathbf{p}^{(0)}$  and the currently reconstructed counterpart.  $\Phi(\mathbf{p}^{(k_{ACID})})$  is an output of the deep reconstruction module, and  $\mathbf{f}^{(k_{ACID})}$  represents the image after compressed sensing-based regularization.

For the optimization problem Eq. (S.3.10), we now compute a tiny perturbation via gradient ascent search. Specifically, we compute

$$D_{\mathbf{p}^{(0)} + \mathbf{A}\mathbf{e}}^l(\mathbf{e}) = \frac{1}{2} \|\hat{\mathbf{f}}(\mathbf{p}, \mathbf{p}^{(0)} + \mathbf{A}\mathbf{e}) - \mathbf{f}\|_2^2 - \frac{\gamma}{2} \|\mathbf{e}\|_2^2. \quad (\text{S.3.11})$$

The backpropagation process for ACID is shown in Fig. S14. More clearly, we define the cost function of ACID as

$$L_c = \frac{1}{2} \|\mathbf{f}_e - \mathbf{f}\|_2^2 - \frac{\gamma}{2} \|\mathbf{e}\|_2^2, \quad (\text{S.3.12})$$

where  $\mathbf{e}$  is the perturbation,  $\mathbf{f}_e = \hat{\mathbf{f}}(\mathbf{p}, \mathbf{p}^{(0)} + \mathbf{A}\mathbf{e})$  is the output of the ACID system with the perturbation  $\mathbf{e}$ , and  $\mathbf{f}$  is the corresponding output without  $\mathbf{e}$ . To find an effective  $\mathbf{e}$ , we need to compute the gradient  $dL_c/d\mathbf{e}$ , and then refine the perturbation  $\mathbf{e}$  using a gradient ascent algorithm. For clarity, the iteration

index for ACID is changed to  $k_{ACID}$  ( $k_{ACID} = 0, \dots, K_{ACID}$ ) in this subsection. In Fig. S13, there are two branches contributing to  $f^{(k_{ACID})}$  ( $k_{ACID} = 1, \dots, K_{ACID} - 1$ ); i.e., Branches 1 and 2. To compute the gradient  $dL_c/de$ , we take both branches into account.

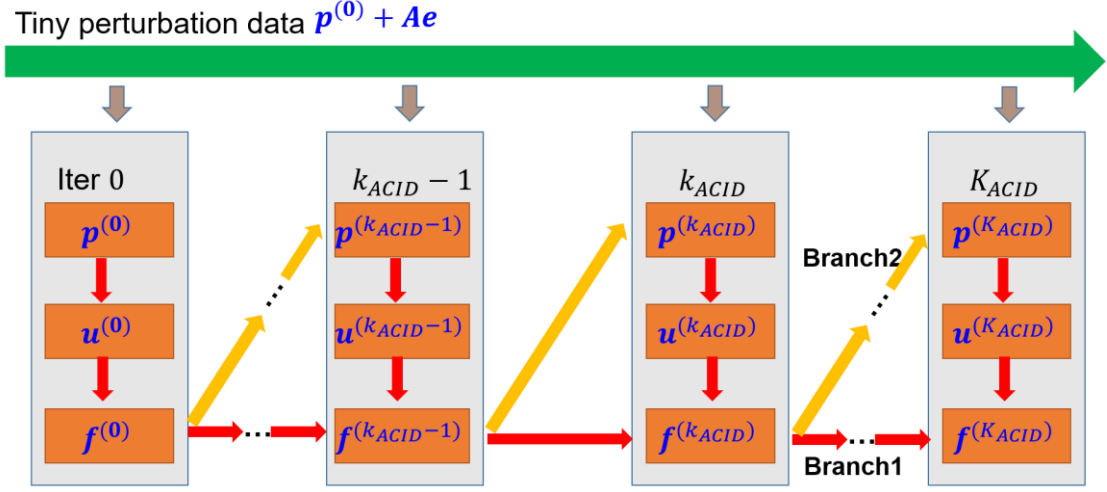


Fig. S12. Feed-forward propagation of adversarial data in the ACID framework.

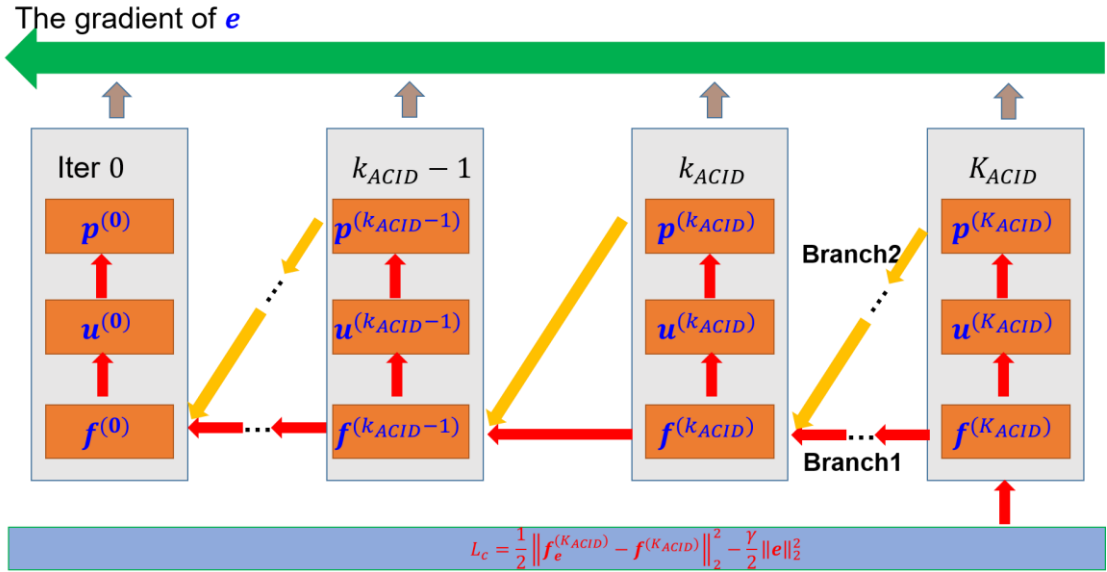


Fig. S13. Backpropagation process of ACID.

Because  $dL_{ACID}/de$  with the loss function  $L_{ACID} = \frac{1}{2} \|f_e - f\|_2^2$  is complicated, we cannot directly compute the gradient of  $L_c$ . Fortunately,  $dL_c/de$  can be solved using the backpropagation algorithm [78, 79], which is commonly used in deep learning [80, 81]. Then,  $dL_c/de$  can be split as

$$\frac{dL_c}{de} = \frac{d(\frac{1}{2} \|f_e - f\|_2^2)}{de} - \gamma e = \frac{d(L_{ACID})}{de} - \gamma e, \quad (\text{S.3.13})$$

Now, let us start the backpropagation process for ACID, as shown in Fig. S13. First, we can decompose the ACID system into the three modules keyed to  $p$ ,

$\mathbf{u}$  and  $\mathbf{f}$  respectively, where  $\mathbf{u} = \Phi(\mathbf{p})$ , and the whole procedure is shown in Fig. S14. The input and the output of  $\mathbf{p}$ ,  $\mathbf{u}$  and  $\mathbf{f}$  are denoted as  $\mathbf{p}_i, \mathbf{u}_i, \mathbf{f}_i, \mathbf{p}_o, \mathbf{u}_o$  and  $\mathbf{f}_o$ , respectively. Also, the gradient of  $\mathbf{p}$ ,  $\mathbf{u}$  and  $\mathbf{f}$  can be denoted as  $\frac{d\mathbf{p}_o}{d\mathbf{p}_i}, \frac{d\mathbf{u}_o}{d\mathbf{u}_i}$  and  $\frac{d\mathbf{f}_o}{d\mathbf{f}_i}$ , respectively.

Following the same steps as that in Algorithm 2, we will use the gradient ascent method to iteratively compute adversarial attacks for the whole ACID system, and the target to be attacked will be changed from a single unstable neural network to our whole ACID workflow. There are two iterative loops: the outer loop is for gradient ascent search, and the inner loop is for ACID feedforward and backpropagation. The stopping criteria for finding an adversarial attack for the whole ACID include (a) the number of iterations reaches the maximum number of iterations for computing an adversarial attack (AA) denoted as  $K_{AA}$ ; or (b) the noise strength of the adversarial attack is greater than that used in attacking the single neural network recorded in our study in terms of the L<sub>2</sub>-norm. As mentioned above, the maximum number of iterations of the inner loop is  $K_{ACID}$  for the ACID feedforward process. Because each whole inner loop can be considered as an intermediate node, we can use the idea of backpropagation to search for a desirable perturbation. To find a tiny perturbation for the whole ACID, the procedure is summarized in Algorithm 3. To generate such tiny perturbations for ACID using the gradient ascent approach, the learning rate ( $\vartheta > 0$ ) needs to be optimized in experiments, and  $\mathbf{e}_0$  is initialed to random noise. More details can be found in <https://zenodo.org/record/4540511>.

Algorithm 3: Adversarial attacking approach for ACID.

---

Input: Image  $\mathbf{f}$ , neural network  $\Phi$ , system matrix  $\mathbf{A}$ , maximum number of iterations  $K_{AA}$ ;  
 Initialization:  $\mathbf{p} \leftarrow \mathbf{A}\mathbf{f}$ ,  $k_{AA} \leftarrow 0$ ,  $\gamma > 0$  and  $\vartheta > 0$ ,  $\mathbf{e}_0, D_{\mathbf{p}^{(0)}}^l(\mathbf{e})$  is defined by Eq. (S.3.9);  
 while the stopping criteria are not satisfied

$$\mathbf{e}^{(k_{AA}+1)} = \mathbf{e}^{(k_{AA})} + \vartheta \nabla_{\mathbf{e}} D_{\mathbf{p}^{(1)+\mathbf{A}\mathbf{e}}}^l(\mathbf{e}^{(k_{AA})});$$

$$k_{aa} = k_{aa} + 1;$$

return  $\mathbf{e}^{(k_{AA})}$ ;

Output: Perturbation  $\mathbf{e}^{(k_{AA})}$ .

---

For the Algorithm 3, the key is to compute  $\nabla_{\mathbf{e}} D_{\mathbf{p}^{(1)+\mathbf{A}\mathbf{e}}}^l(\mathbf{e}^{(k_{AA})})$  using the backpropagation method. In fact, such a gradient computation could be divided into the following three stages, *i.e.*, initial stage, intermediate stage and final stage.

**Initial Stage (1):** The inner iteration index reaches its maximum value, that is  $k_{ACID} = K_{ACID}$ . Without causing any confusion, here we omit the index  $k_{AA}$ , and simply write  $\mathbf{e}^{(k_{AA})}$  as  $\mathbf{e}$ . To enable the backpropagation, we perform the following tasks.

**(1.a)** Compute  $\frac{d(L_{ACID})}{d(\mathbf{f}_e^{(K_{ACID})})}$ . By definition,  $\mathbf{f}_e^{(K_{ACID})} = \mathbf{f}_o^{(K_{ACID})}$ , we have

$$\frac{d(L_{ACID})}{d(\mathbf{f}_e^{(K_{ACID})})} = \frac{d(L_{ACID})}{d(\mathbf{f}_o^{(K_{ACID})})} = \mathbf{f}_e^{(K_{ACID})} - \mathbf{f}^{(K_{ACID})}. \quad (\text{S.3.14})$$

**(1.b)** Compute  $\frac{d(L_{ACID})}{\mathbf{f}_i^{(K_{ACID})}}$ . Since the module  $\mathbf{f}$  is complicated, we compute the gradient pixel by pixel:

$$\frac{d(L_{ACID})}{d(\mathbf{f}_i^{(K_{ACID})}(j_1, j_2))} = \sum_{s_2=1}^{J_2} \sum_{s_1=1}^{J_1} \frac{d(L_{ACID})}{d(\mathbf{f}_o^{(K_{ACID})}(s_1, s_2))} \times \frac{d(\mathbf{f}_o^{(K_{ACID})}(s_1, s_2))}{d(\mathbf{f}_i^{(K_{ACID})}(j_1, j_2))}, \quad (\text{S.3.15})$$

where the gradient  $\frac{d(\mathbf{f}_o^{(K_{ACID})}(s_1, s_2))}{d(\mathbf{f}_i^{(K_{ACID})}(j_1, j_2))}$  is provided by  $\frac{d(\mathbf{f}_o^{(K_{ACID})})}{d(\mathbf{f}_i^{(K_{ACID})})}$ ,  $s_1, s_2$  and  $j_1, j_2$  are

the pixel indices,  $s_1 = 1, \dots, J_1$ ,  $j_1 = 1, \dots, J_1$ ,  $s_2 = 1, \dots, J_2$ ,  $j_2 = 1, \dots, J_2$ , and  $J_1$  and  $J_2$  are the height and width of the reconstructed image.

**(1.c)** By definition, we have

$$\mathbf{f}_i^{(K_{ACID})} = \mathbf{u}_o^{(K_{ACID})} + \mathbf{f}_o^{(K_{ACID}-1)}, \quad (\text{S.3.16})$$

Therefore,

$$\begin{cases} \frac{d(L_{ACID})}{d(\mathbf{u}_o^{(K_{ACID})})} = \frac{d(L_{ACID})}{d(\mathbf{f}_i^{(K_{ACID})})} \\ \frac{d(L_{ACID})}{d(\mathbf{f}_o^{(K_{ACID}-1)})} \Big|_{\text{Branch}=1} = \frac{d(L_{ACID})}{d(\mathbf{f}_i^{(K_{ACID})})} \end{cases}. \quad (\text{S.3.17})$$

**(1.d)** Compute the change in the loss of ACID with respect to  $\mathbf{u}_i^{(K_{ACID})}(j_1, j_2)$ ,

i.e.,  $\frac{d(L_{ACID})}{d(\mathbf{u}_i^{(K_{ACID})}(j_1, j_2))}$ . Using the chain rule, we have

$$\frac{d(L_{ACID})}{d(\mathbf{u}_i^{(K_{ACID})}(j_1, j_2))} = \sum_{s_2=1}^{J_2} \sum_{s_1=1}^{J_1} \frac{d(L_{ACID})}{d(\mathbf{u}_o^{(K_{ACID})}(s_1, s_2))} \cdot \frac{d(\mathbf{u}_o^{(K_{ACID})}(s_1, s_2))}{d(\mathbf{u}_i^{(K_{ACID})}(j_1, j_2))}. \quad (\text{S.3.18})$$

It can be simplified as

$$\frac{d(L_{ACID})}{d(\mathbf{u}_i^{(K_{ACID})})} = \frac{d(L_{ACID})}{d(\mathbf{p}_o^{(K_{ACID})})}. \quad (\text{S.3.19})$$

**(1.e)** Because  $\mathbf{p}_o^{(K_{ACID})} = \mathbf{A}^* \left( \frac{\lambda(\mathbf{A}(\mathbf{f} + \mathbf{e}) - \mathbf{A}\mathbf{f}_o^{(K_{ACID}-1)})}{1 + \lambda + \mu} \right)$ , we have

$$\frac{d(L_{ACID})}{d\mathbf{e}} \Big|_{\text{Iteration}=K_{ACID}} = \frac{\lambda}{1 + \lambda + \mu} (\mathbf{A}^* \mathbf{A} \frac{d(L_{ACID})}{d\mathbf{p}_o^{(K_{ACID})}}), \quad (\text{S.3.20})$$

and

$$\frac{d(L_{ACID})}{d(\mathbf{f}_o^{(k_{ACID}-1)})} \Big|_{Branch=2} = \frac{-\lambda}{1+\lambda+\mu} (\mathbf{A}^* \mathbf{A} \frac{d(L_{ACID})}{d(\mathbf{p}_o^{(k_{ACID})})}). \quad (\text{S.3.21})$$

**(1.f)** Combining Eqs. (S.3.7) and (S.3.10), we obtain

$$\frac{dL_{ACID}}{d(\mathbf{f}_o^{(k_{ACID}-1)})} = \frac{dL_{ACID}}{d(\mathbf{f}_o^{(k_{ACID}-1)})} \Big|_{Branch=1} + \frac{dL_{ACID}}{d(\mathbf{f}_o^{(k_{ACID}-1)})} \Big|_{Branch=2}. \quad (\text{S.3.22})$$

**Intermediate Stage (2):** For the iteration index  $0 < k_{ACID} < K_{ACID}$ , we perform the following tasks:

**(2.a)**  $\frac{d(L_{ACID})}{d(\mathbf{f}_o^{(k_{ACID})})}$  has been obtained in the previous stage. According to  $\mathbf{f}_i^{(k_{ACID})} =$

$\mathbf{u}_o^{(k_{ACID})} + \mathbf{f}_o^{(k_{ACID}-1)}$ , and we compute

$$\frac{d(L_{ACID})}{d(\mathbf{f}_i^{(k_{ACID})}(j_1, j_2))} = \sum_{s_2=1}^{J_2} \sum_{s_1=1}^{J_1} \frac{d(L_{ACID})}{d(\mathbf{f}_o^{(k_{ACID})}(s_1, s_2))} \cdot \frac{d(\mathbf{f}_o^{(k_{ACID})}(s_1, s_2))}{d(\mathbf{f}_i^{(k_{ACID})}(j_1, j_2))}. \quad (\text{S.3.23})$$

Then, we have

$$\frac{d(L_{ACID})}{d(\mathbf{f}_i^{(k_{ACID})}(j_1, j_2))} = \frac{d(L_{ACID})}{d(\mathbf{f}_o^{(k_{ACID}-1)}(j_1, j_2))} \Big|_{Branch=1} = \frac{d(L_{ACID})}{d(\mathbf{u}_o^{(k_{ACID})}((j_1, j_2)))}. \quad (\text{S.3.24})$$

**(2.b)** Compute  $\frac{d(L_{ACID})}{d(\mathbf{u}_i^{(k_{ACID})}(j_1, j_2))}$  as follows:

$$\frac{d(L_{ACID})}{d(\mathbf{u}_i^{(k_{ACID})}(j_1, j_2))} = \sum_{s_2=1}^{J_2} \sum_{s_1=1}^{J_1} \frac{d(L_{ACID})}{d(\mathbf{u}_o^{(k_{ACID})}(s_1, s_2))} \cdot \frac{d(\mathbf{u}_o^{(k_{ACID})}(s_1, s_2))}{d(\mathbf{u}_i^{(k_{ACID})}(j_1, j_2))}. \quad (\text{S.3.25})$$

Since  $\mathbf{u}_i^{(k_{ACID})} = \mathbf{p}_o^{(k_{ACID})}$ , we have

$$\frac{d(L_{ACID})}{d(\mathbf{p}_o^{(k_{ACID})})} = \frac{d(L_{ACID})}{d(\mathbf{u}_i^{(k_{ACID})})}. \quad (\text{S.3.26})$$

**(2.c)** With the definition of  $\mathbf{p}_o^{(k_{ACID})}$ ,  $\frac{d(L_{ACID})}{de}$  in the  $k_{ACID}$ <sup>th</sup> iteration is computed as

$$\frac{d(L_{ACID})}{de} \Big|_{Iteration=k_{ACID}} = \frac{\lambda}{1+\lambda+\mu} \left( \mathbf{A}^* \mathbf{A} \frac{d(L_{ACID})}{d(\mathbf{p}_o^{(k_{ACID})})} \right). \quad (\text{S.3.27})$$

That is,

$$\frac{d(L_{ACID})}{d(\mathbf{f}_o^{(k_{ACID}-1)})} \Big|_{Branch=2} = \frac{-\lambda}{1+\lambda+\mu} (\mathbf{A}^* \mathbf{A} \frac{d(L_{ACID})}{d(\mathbf{p}_o^{(k_{ACID})})}). \quad (\text{S.3.28})$$

**(2.e)** Finally, we have

$$\frac{d(L_{ACID})}{d(\mathbf{f}_o^{(k_{ACID}-1)})} = \frac{d(L_{ACID})}{d(\mathbf{f}_o^{(k_{ACID}-1)})} \Big|_{Branch=1} + \frac{d(L_{ACID})}{d(\mathbf{f}_o^{(k_{ACID}-1)})} \Big|_{Branch=2}. \quad (\text{S.3.29})$$

**Final Stage (3):** In this stage (i.e., the inner iteration equal to 0,  $k_{ACID} = 0$ ). We need to finish the following tasks:

(3.a)  $\frac{d(L_{ACID})}{d(\mathbf{f}_o^{(k_{ACID})})}$  has been obtained from the previous iteration, and

$\frac{d(L_{ACID})}{d(\mathbf{f}_i^{(k_{ACID})}(j_1, j_2))}$  is computed as

$$\frac{d(L_{ACID})}{d(\mathbf{f}_i^{(k_{ACID})}(j_1, j_2))} = \sum_{s_2=1}^{J_2} \sum_{s_1=1}^{J_1} \frac{d(L_{ACID})}{d(\mathbf{f}_o^{(k_{ACID})}(s_1, s_2))} \cdot \frac{d(\mathbf{f}_o^{(k_{ACID})}(s_1, s_2))}{d(\mathbf{f}_i^{(k_{ACID})}(j_1, j_2))}. \quad (\text{S.3.30})$$

Furthermore,

$$\frac{d(L_{ACID})}{d(\mathbf{u}_o^{(k_{ACID})}((j_1, j_2)))} = \frac{d(L_{ACID})}{d(\mathbf{f}_i^{(k_{ACID})}(j_1, j_2))}. \quad (\text{S.3.31})$$

(3.b) When  $k_{ACID} = 0$ , since  $\mathbf{p}_0 = \mathbf{A}^*(\mathbf{A}(\mathbf{f} + \mathbf{e}))$ , we have

$$\frac{d(L_{ACID})}{d\mathbf{e}} \Big|_{\text{Iteration}=0} = \mathbf{A}^* \mathbf{A} \frac{d(L_{ACID})}{d(\mathbf{p}_0)}. \quad (\text{S.3.32})$$

Finally, we compute  $\frac{d(L_C)}{d\mathbf{e}}$  as follows:

$$\frac{d(L_C)}{d\mathbf{e}} = \frac{d(L_{ACID})}{d\mathbf{e}} - \gamma \mathbf{e} = \sum_{k_{ACID}=0}^{K_{ACID}} \frac{d(L_{ACID})}{d\mathbf{e}} \Big|_{\text{Iteration}=k_{ACID}} - \gamma \mathbf{e}. \quad (\text{S.3.33})$$

**Gradient with the  $\mathbf{u}$  module:** The input and the output of the  $\mathbf{u}^{(k_{ACID})}$  module are  $\mathbf{u}_i^{(k_{ACID})}$  and  $\mathbf{u}_o^{(k_{ACID})}$  respectively.  $\mathbf{u}_o^{(k_{ACID})}$  is computed with  $\mathbf{u}_o^{(k_{ACID})} = \Phi(\mathbf{u}_i^{(k_{ACID})})$ , where  $\Phi$  is a well-trained neural network. Note that, for a deep

neural network, such as AUTOMAP,  $\mathbf{p}_o^{(k_{ACID})} = \mathbf{u}_i^{(k_{ACID})} = \mathbf{u}_o^{(k_{ACID})} \cdot \frac{d(\mathbf{u}_o^{(k_{ACID})})}{d(\mathbf{u}_i^{(k_{ACID})})}$

can be obtained directly with the deep-learning-based framework; e.g., TensorFlow (<https://www.tensorflow.org/>) or PyTorch (<https://pytorch.org/>). In the CT case, the E11-50 network was used on the MATLAB platform, and we need to modify the loss function of FBPCConvNet so that we can search for the adversarial attack to the whole ACID workflow. More details can be found on the shared link <https://zenodo.org/record/4540511>.

**Gradient with the  $\mathbf{f}$  module:** The input and the output of the  $\mathbf{f}$  module are  $\mathbf{f}_i^{(k_{ACID})}$  and  $\mathbf{f}_o^{(k_{ACID})}$ . According to the analysis in the main text, we can compute

$\mathbf{f}_o^{(k_{ACID})}$  by minimizing the following objective function:

$$\begin{aligned} \mathbf{f}_o^{(k_{ACID})} &= \underset{\mathbf{f}}{\operatorname{argmin}} \frac{1}{2} \left\| \mathbf{f} - \mathbf{f}_o^{(k_{ACID}-1)} - \frac{1+\mu\rho}{\lambda\rho} \mathbf{u}_o^{(k_{ACID})} \right\|_2^2 + \frac{\xi}{\lambda\rho} \|\mathbf{H}\mathbf{f}\|_1, \\ \text{s. t. } \mathbf{f}_i^{(k_{ACID})} &= \mathbf{f}_o^{(k_{ACID}-1)} + \frac{1+\mu\rho}{\lambda\rho} \mathbf{u}_o^{(k_{ACID})}, \end{aligned} \quad (\text{S.3.34})$$

Let  $\bar{\mathbf{f}} = \mathbf{H}\mathbf{f}$ , Eq. (S.3.34) can be converted to the following problem:

$$\mathbf{f}_o^{(k_{ACID})} = \underset{\mathbf{f}}{\operatorname{argmin}} \frac{1}{2} \left\| \mathbf{H}^* \bar{\mathbf{f}} - \mathbf{f}_o^{(k_{ACID}-1)} - \frac{1+\mu\rho}{\lambda\rho} \mathbf{u}_o^{(k_{ACID})} \right\|_2^2 + \frac{\xi}{\lambda\rho} \|\bar{\mathbf{f}}\|_1, \quad (\text{S.3.35})$$

where  $\mathbf{H}^*$  satisfies  $\mathbf{H}^* \mathbf{H} = \mathbf{I}$ . Thus,  $\mathbf{f}_o^{(k_{ACID})} = \mathbf{H}^* S_{\frac{\xi}{\lambda\rho}} \left( \mathbf{H} \left( \mathbf{f}_o^{(k_{ACID}-1)} + \frac{1+\mu\rho}{\lambda\rho} \mathbf{u}_o^{(k_{ACID})} \right) \right)$ , where  $S_\xi$  represents the soft thresholding operator [82], which can be written as

$$S_\xi(x) = \begin{cases} 0, & |x| < \xi \\ x - \operatorname{sgn}(x)\xi & \text{otherwise} \end{cases}, \quad (\text{S.3.36})$$

Then, we can obtain  $\frac{d(\mathbf{f}_o^{(k_{ACID})})}{d(\mathbf{f}_i^{(k_{ACID})})}$  using the chain rule after combining Eqs. (S.3.35) and (S.3.36).

## IV. Theoretical Analyses on the ACID Workflow

### A. Theoretical Background

The vulnerability of neural networks has been demonstrated with adversarial attacks in all major deep learning tasks, from misclassification examples to deep reconstruction instabilities. In their landmark paper, Antun et al. showed that deep reconstruction is unstable due to lack of kernel awareness but sparsity-promoting reconstruction does not have such a problem [6]. To address these instabilities, we design an Analytic, Compressive Iterative Deep (ACID) network. The key idea behind ACID is to combine data-driven priors and sparsity constraints to outperform either simple-minded deep reconstruction networks or established compressed sensing based reconstruction methods. In our study, we have not only experimentally shown the merits of ACID but also theoretically analyzed the rationale of ACID in terms of its converging behavior and solution characteristics. In the following, we put our analysis on ACID in the perspective of others' analyses on general computational optimization in general and existing representative image reconstruction networks in particular.

*There are profound results in non-computability in the field of computer science.* Computational optimization is important not only in the field of computer science but also to our real-world applications, from linear programming to deep learning. The theoretical research on this theme can be traced back to Turing's ground-breaking paper on machine intelligence and Smale's list of problems for the 21st century. Specifically, Smale's 9<sup>th</sup> problem is that *"Is there a polynomial time algorithm over the real numbers which*

*decides the feasibility of the linear system of inequalities  $Ax \geq y$ ?" [83]. In practice,  $A$  and  $y$  can only be approximately obtained, and an extended (precision-limited) version of Smale's 9th problem is critically important. Recently, Bastounis, Hansen and Vlačić [84] made remarkable progress in settling this theoretical issue. Their theory bears a major implication for Smale's 18<sup>th</sup> problem about the boundary of artificial intelligence (AI), i.e., deep learning as the current mainstream of AI. They show that it is in general non-computable to construct a neural network via loss minimization and apply it to testing data, and such a neural network is generally unstable. For example, there are in principle many classification problems for which "one may have 100% success rate on arbitrarily large training and validation data sets, and yet there are uncountably many points arbitrarily close to the training data for which the trained network will fail."*

*Tomographic reconstruction is an important type of computational optimization problems, and, interestingly enough, deep networks for image reconstruction can and cannot be computed under different conditions.* In the context of these inverse problems, the article by Antun et al. reported instabilities of deep reconstruction networks [6] due to the lack of kernel awareness [85]. Then, a comprehensive follow-up analysis by Antun, Colbrook, and Hansen [86] established the boundary of deep learning inspired tomographic reconstruction, which helps address Smale's 18<sup>th</sup> problem. Among their contributions, the following three points are clearly made on (1) existence, (2) non-existence, and (3) the conditional existence of desirable networks. That is, while the existence of neural networks is proved in the literature for an excellent functional representation, the non-existence is proved of any algorithm that trains or computes such a neural network in a general setting. However, the conditional existence is also proved of such an algorithm to compute an accurate and stable network that solves meaningful inverse problems such as Fourier imaging from sparse data. Specifically, the existence of a network for a universal representation is well known (Theorem 2.1 in [86]), but how to train a network to achieve an accurate and stable approximation is a different issue. It has been shown that a counterexample can always be found in a general setting so that the accuracy and robustness of a network cannot be simultaneously obtained (Theorem 2.2 in [86]). On the other hand, under certain conditions, such as sparsity in levels, an accurate and stable network can be indeed obtained (Theorems 5.5 and 5.10 in [86]), with the FIRENET network as a good example [86]. At the core of the construction of FIRENET is the kernel awareness. Clearly, training the network defined in Subsection 5.1 in [86] cannot obtain kernel awareness and is subject to the phase transition of solutions to the inverse problems. In other words, if the difference between the two images lies close to the null space of the measurement matrix and is bounded from below, the Lipschitz constant of the inverse mapping can be very large, yielding a poor imaging performance. Fortunately, an algorithm can be used to utilize sparsity in levels and find a stable and accurate neural network

(Theorems 5.5 and 5.10 in [86], with uniform recovery guarantees, geometric convergence, bounds on the number of samples and the number of layers of a network for a pre-specified accuracy).

*In addition to the excellent work by Antun et al., active research efforts have been going on to develop deep networks for accurate and stable deep tomographic reconstruction.* Representative results include the LEARN (“*Learned Experts’ Assessment-based Reconstruction Network*”) network [87], ItNet network [88], Momentum-Net [89], null space network [90], as well as deep equilibrium networks [91].

In [87], an iterative reconstruction algorithm in the CS framework was unrolled and trained in the end-to-end fashion. The experimental results from the resultant LEARN network on the Mayo Clinic low-dose CT dataset are competitive with representative methods in terms of artifact reduction, feature preservation, and computational speed. In [88], an iterative deep-learning-based reconstruction network was designed to solve underdetermined inverse problems accurately and stably (ItNet shown in Fig. 1 in [88]). In comparison with total-variation minimization, their results reveal that standard end-to-end network architectures are not only resilient against statistical noise but also against adversarial perturbations. In [89], another iterative neural network, referred to as Momentum-Net, was prototyped by combining data-driven regression and model-based image reconstruction (MBIR). Momentum-Net is convergent under reasonable conditions (quadratic majorization via M-Lipschitz continuous gradients). Their results show that Momentum-Net outperformed MBIR and several other networks, but the effect of adversarial attacks on Momentum-Net was not evaluated. In [90], a null space network was studied to offer a theoretical justification to deep learning-based tomographic reconstruction via so-called  $\Phi$ -regularization. The convergence of the overall reconstruction workflow is proved, assuming a Lipschitz continuity and preserving the data consistency (illustrated in Fig. 1 in [90]). In [91], the deep equilibrium models were adapted to find the fixed point with guaranteed convergence under the  $\varepsilon$ - Lipschitz continuity. Subsequently, the trade-off can be made between reconstruction quality and computational cost.

*In connection with the above results, our ACID network has significant merits and unique features.* First, ACID is dedicated to overcoming the instabilities of neural networks in the same settings using the same datasets as that described in [6]. As a result, we have made a solid step forward along the direction of stabilizing deep reconstruction networks, showing that accurate and stable deep reconstruction is feasible, and remains an exciting research opportunity. Second, the ACID network is the first prototype that combines an established sparsity-oriented algorithm, a data-driven direct reconstruction network, and an iterative data fidelity enforcement (for example, LEARN [87] ignores data consistency; ItNet network [88] lacks kernel awareness, Momentum-Net [89] misses a learned mapping from data to images, null space

network [90] uses no sparsity, and deep equilibrium networks [91] focuses only on the fixed point that does not imply image sparsity nor data fidelity). Third, the converging behavior and solution characteristics of ACID have been analyzed under a reasonable assumption. The assumption is called the bounded error norm, which is a special case of a Lipschitz continuity. The Lipschitz continuity we used in our convergence analysis, which is practically interpreted as the Bounded Error Norm (BEN) property and experimentally verified in our study, is consistent with the previous studies on non-convex optimization such as in the aforementioned network convergence analyses in [89-91]. Furthermore, note that we do not request the measurement matrix must satisfy a compressed sensing condition such as the restricted isometry property. This means that a standard sparsity-promotion algorithm may not give a unique solution. In this case, ACID promises to outperform the sparsity-minimization reconstruction alone, because data-prior plays a significant role to fill in the gap in deep reconstruction. Last but not the least, in addition to an accurate reconstruction performance, ACID has stability in the two related aspects: (a) ACID can stabilize an unstable deep reconstruction network (by putting it in the ACID framework), and (b) ACID as a whole is resilient against adversarial attacks. Both the aspects of the ACID stability have been systematically shown in our studies.

## B. Bounded Error Norm (BEN) Property

Our analysis requires the following bounded error norm (BEN) property of a reconstruction neural network. If a reconstruction network satisfies the BEN property, we call it a well-designed and well-trained reconstruction network, or a proper network.

**Definition:** A reconstruction network has the BEN property if the ratio is less than  $(1 - \sigma)$  between the  $L_2$  norm of the reconstruction error and the norm of the corresponding ground truth with  $0 < \sigma < 1$ .

For an  $s$ -sparse image  $\mathbf{f}$ , the BEN property implies that  $\Phi(\mathbf{A}\mathbf{f}) = \mathbf{f} + \mathbf{f}^{ob} + \mathbf{f}^{nl}$  where the second and third terms are observable and null-space components, and  $\|\mathbf{f}^{ob} + \mathbf{f}^{nl}\| \leq (1 - \sigma)\|\mathbf{f}\|$ .

**Remark 1:** In the literature of deep imaging, including the paper on instabilities of deep reconstruction [6], a reconstruction network, even if it is unstable, will still produce an output not too far from the ground truth in the sense of the BEN property. The involved errors of types I and II have significant clinical impacts but the norm of these errors in combination is assumed to be small relative to that of the underlying image. This is how a proper reconstruction network is defined and commonly expected in practice. For example, the most popular loss function of a reconstruction network is in the  $L_2$  norm so that a reconstructed image should be close to the ground truth in the sense of the  $L_2$

norm without an adversarial attack. Furthermore, if the strength of adversarial attacks is in a reasonable range, the BEN property is assumed to be valid as the condition for our convergence analysis below.

**Remark 2:** For deep reconstruction in the supervised mode, a training dataset is typically in the format of  $(\mathbf{p}(i), \mathbf{f}(i))$ ,  $i = 1, 2, \dots, I_{trn}$ . We assume that the imaging model is linear, and we can augment the training dataset to  $(\alpha \mathbf{p}(i), \alpha \mathbf{f}(i))$ ,  $i = 1, 2, \dots, I_{trn}$ , where  $\alpha$  is any constant within a reasonable range. With the augmented data, the network will map input of a small norm to an output of a proportionally small norm. Alternatively, we can include the normalization layer(s) in the reconstruction network so that the network performance is insensitive to the magnitude of data/images.

**Remark 3:** Our assumption of the BEN property is similar to the requirement for CS theory in terms of RIP/rNSP so that data can be analyzed to extract sufficient information for image recovery. If the requirement is not met, the theoretical arguments below will not work.

For our theoretical analysis, we have assumed the BEN property of the reconstruction network, and thus avoided directly handling of the non-convex optimization of the network. As a result, even if the network is not optimized, the convergence is guaranteed, as long as the relative error of reconstruction results and ground truth is under control (less than 100%) in terms of the  $L_2$  norm, which is a global measure and a quite mild condition in practice. On the other hand, it is underlined that if the network is indeed optimized or nearly optimized, the iterative process will converges rapidly. We have shown that this ratio (RA) is substantially less than 1 even in the worst case in the [6].

Specifically, all the experimental results with perturbations were further repeated in the CT and MRI cases reported in [6]. Then, the RAs were computed using different reconstruction networks with different perturbations. It is found that all RAs in CT and MRI experiments are substantially less than 1. As shown in Table S1 and Figs. S14-17, the AUTOMAP seems more sensitive to the perturbations; i.e., small perturbations causes large changes in the sense of the  $L_2$ -norm. Clearly, BEN property is satisfied in this instability study.

Table S1. RAs(%) associated with different reconstruction networks.

Methods	$r_1$	$r_2$	$r_3$	$r_4$
Med-50	2.90	x	x	x
AUTOMAP	10.39	23.09	47.85	85.86
Deep MRI	2.73	8.03	13.28	x
MRI-VN	3.53	x	x	x

It is easy to observe that the perturbed images contain artifacts; for example, the MED-50, AUTOMAP and MRI-VN results. In these cases, the sparsity of reconstructed images were corrupted. Besides, the feed forward estimation of reconstruction results is usually not consistent with original measurement.

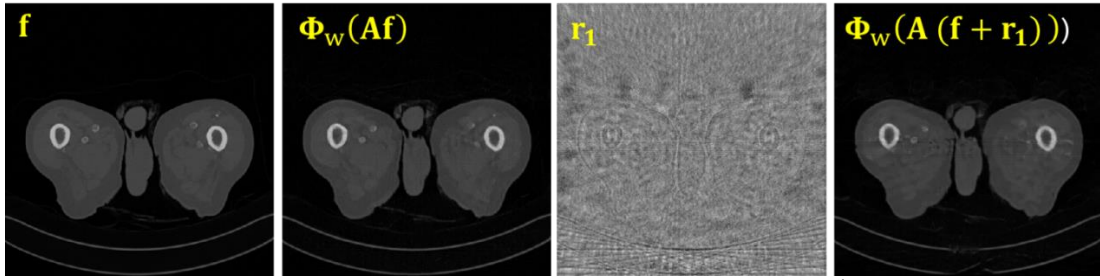


Fig. S14. Reconstruction results using MED-50[1] from [6]. The 1<sup>st</sup>- 4<sup>th</sup> images represent the original, MED-50 without perturbation, perturbation, and perturbed MED-50 results respectively.

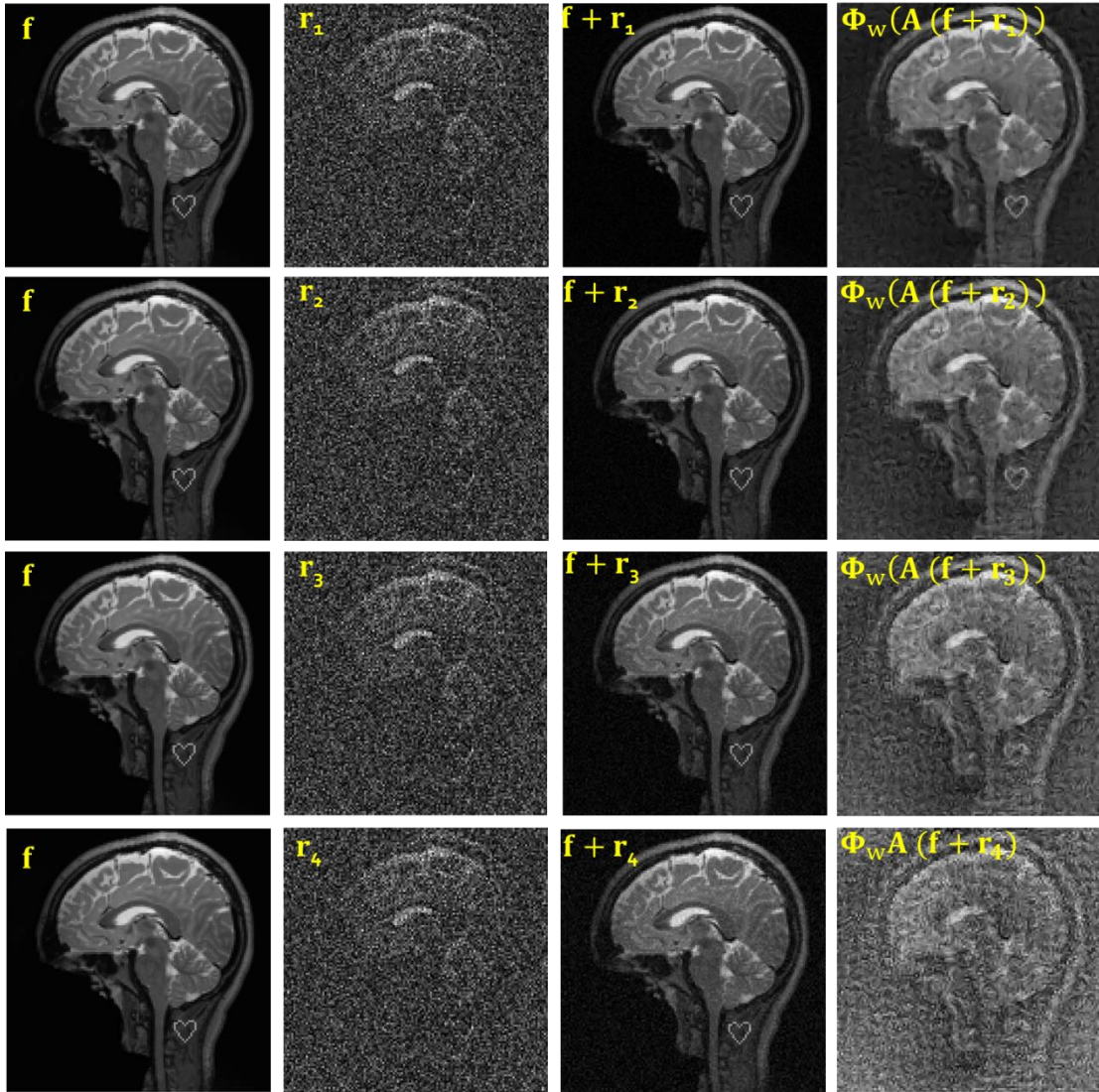


Fig. S15. Reconstruction results using AUTOMAP[23] from [6]. The 1<sup>st</sup>-4<sup>th</sup> columns represent the original, perturbation, original plus perturbation, and perturbed AUTOMAP images respectively. The 1<sup>st</sup> -4<sup>th</sup> rows represent different strengths of perturbation, where  $\|r_1\|_F^2 < \|r_2\|_F^2 < \|r_3\|_F^2 < \|r_4\|_F^2$ .

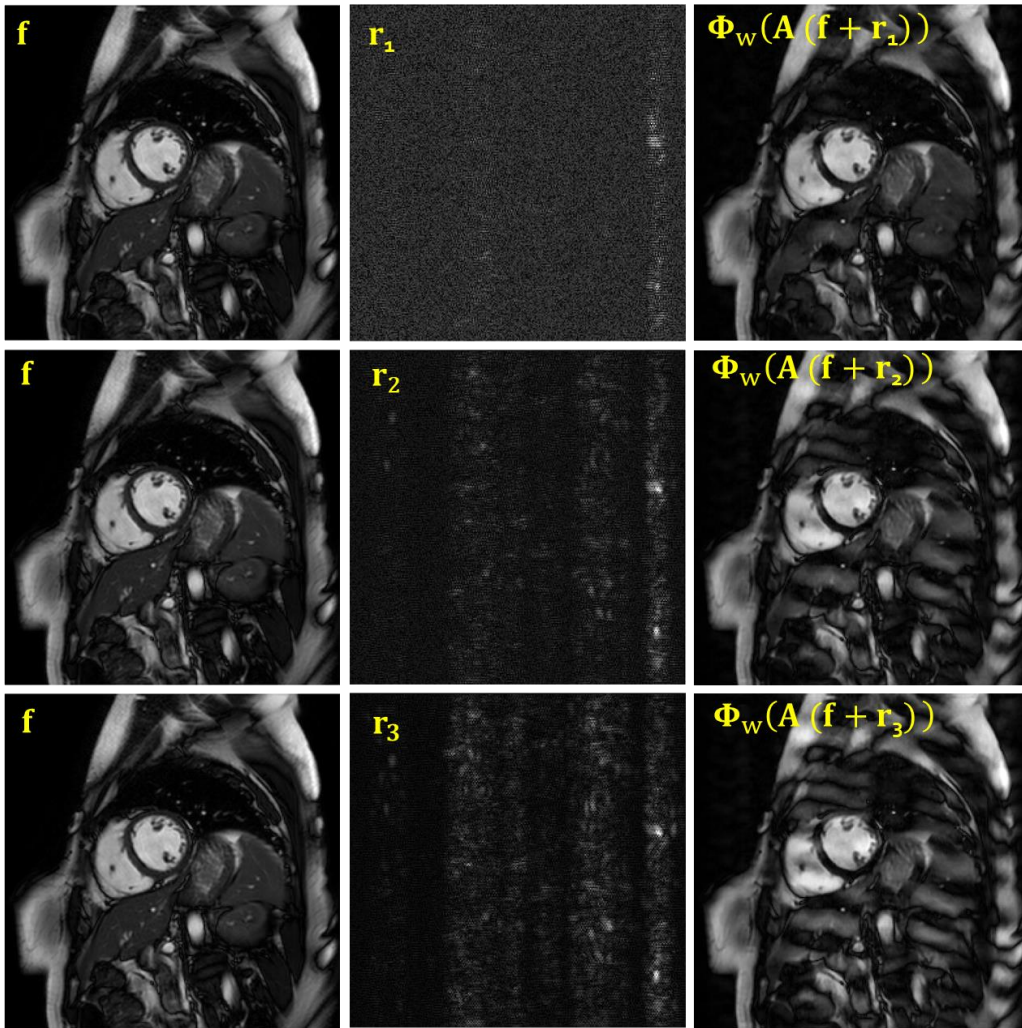


Fig. S16. Reconstruction results using Deep MRI (DM) [92]. These results were adapted from [6]. The 1<sup>st</sup>-3<sup>rd</sup> columns represent the original, perturbation, and perturbed DM results respectively. The 1<sup>st</sup>-3<sup>rd</sup> rows present different strengths of perturbation, where  $\|r_1\|_F^2 < \|r_2\|_F^2 < \|r_3\|_F^2$ .

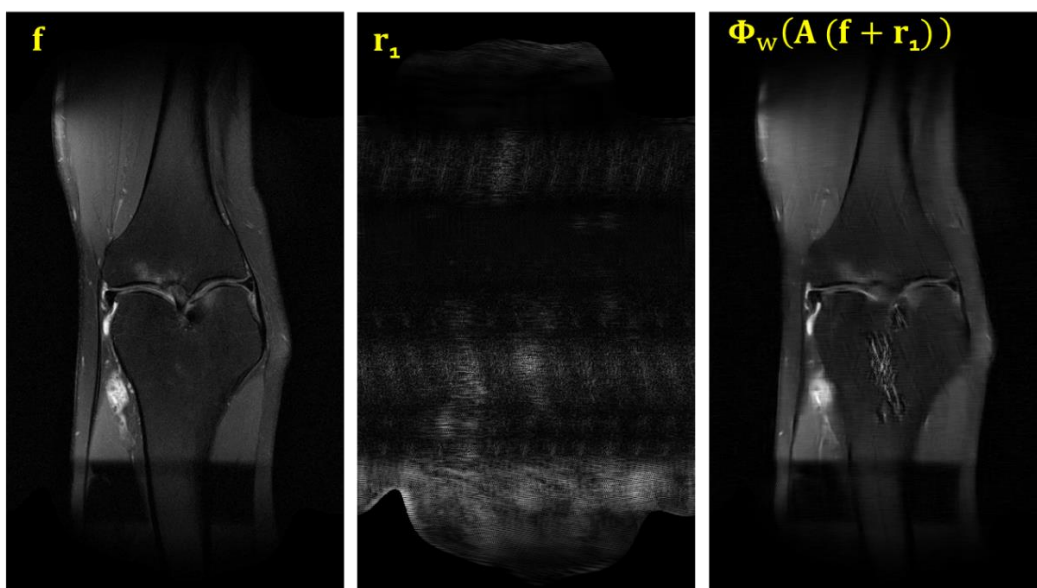


Fig. S17. Reconstruction results using MRI-VN [93] from [6]. The 1<sup>st</sup>-3<sup>rd</sup> images represent the original, perturbation, and perturbed MRI-VN results respectively.

Searching a proper feasible solution within the space of sparse solution is central to the traditional iteration reconstruction. Furthermore, the ACID searches for a reconstruction good in the three aspects: low-dimensional sparsity, big data prior, and iterative calibration to eliminate unexplained residual data. When the final image satisfies all these three constraints, it will be our best possible solution.

### C. Convergence Analysis

Now, let us analyze the convergence of our ACID scheme. Let us denote  $M_1 = \frac{\lambda}{1+\lambda+\mu}$  and  $M_2 = \frac{1+\mu\rho}{\lambda\rho}$ . Furthermore, we assume that  $M_1M_2 = \frac{\lambda}{1+\lambda+\mu} \frac{1+\mu\rho}{\lambda\rho} = 1$  which can be implemented by adjusting  $\lambda$  to satisfy  $\lambda = \frac{1}{\rho} - 1$ , and  $\rho$  is a constant depending on the measurement matrix  $\mathbf{A}$ . Eq. (20) in the main text can be simplified to our heuristically-designed ACID iteration:

$$\begin{cases} \mathbf{p}^{(k+1)} = M_1(\mathbf{p}^{(0)} - \mathbf{A}\mathbf{f}^{(k)}) \\ \mathbf{f}^{(k+1)} = \mathbf{H}^* \mathcal{S}_\varepsilon \left( \mathbf{H}(\mathbf{f}^{(k)} + M_2\Phi(\mathbf{p}^{(k+1)})) \right) \end{cases} \quad (\text{S.4.1})$$

Let us analyze the convergence of our ACID network as follows. Because the input to the neural network is  $\mathbf{p}^{(0)} - \mathbf{e}$  in our objective function Eq. (1) in the main text, we initially assume that the noise is  $\mathbf{e} = 0$  and  $\mathbf{p}^{(0)} = \mathbf{A}\mathbf{f}^*$ , where  $\mathbf{f}^*$  is the ground truth. Assuming an initial image  $\Phi(\mathbf{p}^{(0)}) = \mathbf{f}^* + \mathbf{f}^{(ob,0)} + \mathbf{f}^{(nl,0)}$ . By the BEN property, we have

$$\|\mathbf{f}^{(ob,0)} + \mathbf{f}^{(nl,0)}\| < (1 - \sigma)\|\mathbf{f}^*\|. \quad (\text{S.4.2})$$

Since  $\mathbf{H}\mathbf{f}^{(ob,0)}$  and  $\mathbf{H}\mathbf{f}^{(nl,0)}$  are orthogonal, we have

$$\begin{aligned} \|\mathbf{f}^{(ob,0)} + \mathbf{f}^{(nl,0)}\| &= \|\mathbf{H}\mathbf{f}^{(ob,0)} + \mathbf{H}\mathbf{f}^{(nl,0)}\| \\ &= \|\mathbf{H}\mathbf{f}^{(ob,0)}\| + \|\mathbf{H}\mathbf{f}^{(nl,0)}\| \\ &= \|\mathbf{f}^{(ob,0)}\| + \|\mathbf{f}^{(nl,0)}\|. \end{aligned} \quad (\text{S.4.3})$$

This implies that

$$\|\mathbf{f}^{(ob,0)}\| < (1 - \sigma)\|\mathbf{f}^*\|. \quad (\text{S.4.4})$$

Since  $\mathbf{f}^{(0)}$  is the output of the soft-thresholding filtering, it can be expressed as

$$\mathbf{f}^{(0)} = \Phi(\mathbf{p}^{(0)}) - \mathbf{H}^* \bar{\mathbf{f}}^{(e,0)}, \quad (\text{S.4.5})$$

where  $\bar{\mathbf{f}}^{(e,0)}$  is a noise background in the transform domain. If we denote  $\bar{f}_n^{(e,0)}$  as the  $n^{\text{th}}$  component of  $\bar{\mathbf{f}}^{(e,0)}$ , there will be  $|\bar{f}_n^{(e,0)}| \leq \varepsilon$ , which is a noise floor.

Without loss of generality, in the transform domain we assume the first  $s$  components span the  $s$ -sparse space of  $\mathbf{H}\mathbf{f}^*$ . Because only the first  $s$  components of  $\bar{\mathbf{f}}^{(e,0)}$  is observable, let us decompose  $\bar{\mathbf{f}}^{(e,0)}$  into two parts  $(\bar{\mathbf{f}}^{(e,0)})_{n \leq s}$  and  $(\bar{\mathbf{f}}^{(e,0)})_{n > s}$ , where  $(\bar{\mathbf{f}}^{(e,0)})_{n \leq s}$  is observable and  $(\bar{\mathbf{f}}^{(e,0)})_{n > s}$  is in the null space of  $\mathbf{A}$ . Then, (S.4.5) can be rewritten as

$$\mathbf{f}^{(0)} = \mathbf{f}^* + \mathbf{f}^{(ob,0)} - \mathbf{H}^* (\bar{\mathbf{f}}^{(e,0)})_{n \leq s} + \mathbf{g}^{(nl,0)}, \quad (\text{S.4.6})$$

where  $\mathbf{g}^{(nl,0)} = \mathbf{f}^{(nl,0)} - \mathbf{H}^* (\bar{\mathbf{f}}^{(e,0)})_{n > s}$  is in the null space of  $\mathbf{A}$ .

**For the case  $k = 0$ :**

From (S.4.1) and (S.4.6), we have

$$\mathbf{p}^{(1)} = M_1(\mathbf{p}^{(0)} - \mathbf{A}\mathbf{f}^{(0)}) = -M_1\mathbf{A}\mathbf{f}^{(ob,0)} + M_1\mathbf{A}\mathbf{H}^*(\bar{\mathbf{f}}^{(e,0)})_{n \leq S}, \quad (\text{S.4.7})$$

$$\Phi(\mathbf{p}^{(1)}) = -M_1\mathbf{f}^{(ob,0)} + M_1\mathbf{H}^*(\bar{\mathbf{f}}^{(e,0)})_{n \leq S} + \mathbf{f}^{(ob,1)} + \mathbf{f}^{(nl,1)}, \quad (\text{S.4.8})$$

$$\|\mathbf{f}^{(ob,1)}\| < (1 - \sigma) \left\| M_1\mathbf{f}^{(ob,0)} - M_1\mathbf{H}^*(\bar{\mathbf{f}}^{(e,0)})_{n \leq S} \right\|, \quad (\text{S.4.9})$$

$$\begin{aligned} \mathbf{f}^{(1)} &= \mathbf{f}^{(0)} + M_2\Phi(\mathbf{p}^{(1)}) - \mathbf{H}^*\bar{\mathbf{f}}^{(e,1)} \\ &= \mathbf{f}^* + M_2\mathbf{f}^{(ob,1)} - \mathbf{H}^*(\bar{\mathbf{f}}^{(e,1)})_{n \leq S} + \mathbf{g}^{(nl,1)}, \end{aligned} \quad (\text{S.4.10})$$

where  $\mathbf{g}^{(nl,1)} = \mathbf{g}^{(nl,0)} + M_2(\mathbf{f}^{(nl,1)}) - \mathbf{H}^*(\bar{\mathbf{f}}^{(e,1)})_{n > S}$  is the null space of  $\mathbf{A}$ .

**For the case  $k = 1$ :**

From (S.4.1) and (S.4.10), we have

$$\mathbf{p}^{(2)} = M_1(\mathbf{p}^{(0)} - \mathbf{A}\mathbf{f}^{(1)}) = -\mathbf{A}\mathbf{f}^{(ob,1)} + M_1\mathbf{A}\mathbf{H}^*(\bar{\mathbf{f}}^{(e,1)})_{n \leq S}, \quad (\text{S.4.11})$$

$$\Phi(\mathbf{p}^{(2)}) = -\mathbf{f}^{(ob,1)} + M_1\mathbf{H}^*(\bar{\mathbf{f}}^{(e,1)})_{n \leq S} + \mathbf{f}^{(ob,2)} + \mathbf{f}^{(nl,2)}, \quad (\text{S.4.12})$$

$$\|\mathbf{f}^{(ob,2)}\| < (1 - \sigma) \left\| -\mathbf{f}^{(ob,1)} + M_1\mathbf{H}^*(\bar{\mathbf{f}}^{(e,1)})_{n \leq S} \right\|, \quad (\text{S.4.13})$$

$$\mathbf{f}^{(2)} = \mathbf{f}^* + M_2\mathbf{f}^{(ob,2)} - \mathbf{H}^*(\bar{\mathbf{f}}^{(e,2)})_{n \leq S} + \mathbf{g}^{(nl,2)}, \quad (\text{S.4.14})$$

with  $\mathbf{g}^{(nl,2)} = \mathbf{g}^{(nl,1)} + M_2\mathbf{f}^{(nl,2)} - \mathbf{H}^*(\bar{\mathbf{f}}^{(e,2)})_{n > S}$ .

If we continue the above procedure, it is easy to obtain that

$$\mathbf{p}^{(k+1)} = -\mathbf{A}\mathbf{f}^{(ob,k)} + M_1\mathbf{A}\mathbf{H}^*(\bar{\mathbf{f}}^{(e,k)})_{n \leq S}. \quad (\text{S.4.15})$$

$$\|\mathbf{f}^{(ob,k+1)}\| < (1 - \sigma) \left\| -\mathbf{f}^{(ob,k)} + M_1\mathbf{H}^*(\bar{\mathbf{f}}^{(e,k)})_{n \leq S} \right\|. \quad (\text{S.4.16})$$

Because each component of  $(\bar{\mathbf{f}}^{(e,k)})_{n \leq S}$  is bounded by  $\varepsilon$ , we have

$$\left\| \mathbf{H}^*(\bar{\mathbf{f}}^{(e,k)})_{n \leq S} \right\| = \left\| (\bar{\mathbf{f}}^{(e,k)})_{n \leq S} \right\| \leq \varepsilon\sqrt{S}. \quad (\text{S.4.17})$$

(S.4.16) implies that

$$\begin{aligned} \|\mathbf{f}^{(ob,k+1)}\| &< (1 - \sigma) \left( \|\mathbf{f}^{(ob,k)}\| + \left\| M_1\mathbf{H}^*(\bar{\mathbf{f}}^{(e,k)})_{n \leq S} \right\| \right) \\ &\leq (1 - \sigma) \left( \|\mathbf{f}^{(ob,k)}\| + \varepsilon M_1\sqrt{S} \right). \end{aligned} \quad (\text{S.4.18})$$

When  $\|\mathbf{f}^{(ob,k)}\|$  satisfies the condition

$$\begin{aligned} (1 - \sigma) \left( \|\mathbf{f}^{(ob,k)}\| + \varepsilon M_1\sqrt{S} \right) &< \|\mathbf{f}^{(ob,k)}\|, \\ \|\mathbf{f}^{(ob,k)}\| &\geq \frac{(1 - \sigma)}{\sigma} \varepsilon M_1\sqrt{S}, \end{aligned} \quad (\text{S.4.19})$$

we have that

$$\|\mathbf{f}^{(ob,k+1)}\| < \|\mathbf{f}^{(ob,k)}\|. \quad (\text{S.4.20})$$

That is,  $\|\mathbf{f}^{(ob,k)}\|$  will converge under the condition (S.4.19). Without loss of generality, we assume that  $\|\mathbf{f}^{(ob,k_c-1)}\| \geq \frac{(1 - \sigma)}{\sigma} \varepsilon M_1\sqrt{S}$  and  $\|\mathbf{f}^{(ob,k_c)}\| < \frac{(1 - \sigma)}{\sigma} \varepsilon M_1\sqrt{S}$ .

Next, let us analyze the case  $\|\mathbf{f}^{(ob,k)}\| < \frac{(1 - \sigma)}{\sigma} \varepsilon M_1\sqrt{S}$  for  $k \geq k_c$ , which can be considered as the case that the signal is weak relative to the noise level characterized by  $\frac{(1 - \sigma)}{\sigma} \varepsilon M_1\sqrt{S}$ . From (S.4.18), we obtain that

$$\|\mathbf{f}^{(ob,k_c+1)}\| \leq (1 - \sigma) \left( \|\mathbf{f}^{(ob,k_c)}\| + \varepsilon M_1\sqrt{S} \right) \leq \frac{(1 - \sigma)}{\sigma} \varepsilon M_1\sqrt{S}. \quad (\text{S.4.21})$$

In fact, (S.4.21) only provides the supremum of  $\|\mathbf{f}^{(ob,k_c+1)}\|$ , and we can model  $\|\mathbf{f}^{(ob,k_c+1)}\|$  as a random variable in the range of  $\left[ 0, \frac{(1 - \sigma)}{\sigma} \varepsilon M_1\sqrt{S} \right]$ . Without loss of generality, we assume that  $\|\mathbf{f}^{(ob,k_c+1)}\|$  obeys a uniform distribution, and for other distributions we can perform a similar analysis and obtain the same result. By denoting the expectation of  $\|\mathbf{f}^{(ob,k_c+1)}\|$  as  $E(\mathbf{f}^{ob}, k_c + 1)$ , we have

$E(\mathbf{f}^{ob}, k_c + 1) = \frac{1}{2} \frac{(1-\sigma)}{\sigma} \varepsilon M_1 \sqrt{s}$ . In the same principle, we can treat  $\|\mathbf{f}^{(ob, k_c + k + 1)}\|$  as a random variable uniformly distributed in the range of  $[0, \|\mathbf{f}^{(ob, k_c + k)}\| + \varepsilon M_1 \sqrt{s}]$ . From (S.4.18), we have

$$E(\mathbf{f}^{ob}, k_c + k + 1) = \frac{1}{2} (1 - \sigma) (E(\mathbf{f}^{ob}, k_c + k) + \varepsilon M_1 \sqrt{s}). \quad (\text{S.4.22})$$

That is,

$$E(\mathbf{f}^{ob}, k_c + k + 1) = \left( \frac{1}{\sigma} \left( \frac{1-\sigma}{2} \right)^{k+1} + \frac{1-\sigma}{1+\sigma} \left( 1 - \left( \frac{1-\sigma}{2} \right)^k \right) \right) \varepsilon M_1 \sqrt{s}. \quad (\text{S.4.23})$$

When  $k \rightarrow \infty$ , Eq.(S.4.23) shows that  $E(\mathbf{f}^{ob}, k_c + k)$  will approach to  $\frac{1-\sigma}{1+\sigma} \varepsilon M_1 \sqrt{s}$ . Because  $\|\mathbf{f}^{(ob, k_c + k)}\|$  is uniformly distributed between 0 and its maximum, we have  $\|\mathbf{f}^{(ob, k_c + k)}\| \leq 2 E(\mathbf{f}^{ob}, k_c + k) = \frac{2(1-\sigma)}{1+\sigma} \varepsilon M_1 \sqrt{s}$ , which is a noise-induced uncertainty range of the imaging system. In other words, the ACID algorithm will converge to a solution in the intersection of the space constrained by measured data, the space of sparse solutions, and the space of deep priors.

## References

1. Jin, K.H., et al., *Deep convolutional neural network for inverse problems in imaging*. IEEE Transactions on Image Processing, 2017. **26**(9): p. 4509-4522.
2. He, K., et al. *Deep residual learning for image recognition*. in *Proceedings of the IEEE conference on computer vision and pattern recognition*. 2016.
3. Ronneberger, O., P. Fischer, and T. Brox. *U-net: Convolutional networks for biomedical image segmentation*. in *International Conference on Medical image computing and computer-assisted intervention*. 2015. Springer.
4. Vedaldi, A. and K. Lenc. *Matconvnet: Convolutional neural networks for matlab*. in *Proceedings of the 23rd ACM international conference on Multimedia*. 2015.
5. Pascanu, R., T. Mikolov, and Y. Bengio. *On the difficulty of training recurrent neural networks*. in *International conference on machine learning*. 2013.
6. Antun, V., et al., *On instabilities of deep learning in image reconstruction and the potential costs of AI*. Proceedings of the National Academy of Sciences, 2020.
7. Yu, H., S. Zhao, and G. Wang, *A differentiable Shepp–Logan phantom and its applications in exact cone-beam CT*. Physics in Medicine & Biology, 2005. **50**(23): p. 5583.
8. Averbuch, A., I. Sedelnikov, and Y. Shkolnisky, *CT reconstruction from parallel and fan-beam projections by a 2-D discrete Radon transform*. IEEE Transactions on Image Processing, 2011. **21**(2): p. 733-741.
9. Zhang, Z., et al., *A sparse-view CT reconstruction method based on combination of DenseNet and deconvolution*. IEEE transactions on medical imaging, 2018. **37**(6): p. 1407-1417.
10. Zang, G., et al. *Super-resolution and sparse view CT reconstruction*. in *Proceedings of the European Conference on Computer Vision (ECCV)*. 2018.
11. Hu, D., et al., *Hybrid-Domain Neural Network Processing for Sparse-View CT Reconstruction*. IEEE Transactions on Radiation and Plasma Medical Sciences, 2020. **5**(1): p. 88-98.
12. Gottschling, N.M., et al., *The troublesome kernel: why deep learning for inverse problems is typically unstable*. arXiv preprint arXiv:2001.01258, 2020.

13. Yang, G., et al., *DAGAN: Deep de-aliasing generative adversarial networks for fast compressed sensing MRI reconstruction*. IEEE transactions on medical imaging, 2017. **37**(6): p. 1310-1321.
14. Hwang, H., H.Z.U. Rehman, and S. Lee, *3D U-Net for skull stripping in brain MRI*. Applied Sciences, 2019. **9**(3): p. 569.
15. Dolz, J., C. Desrosiers, and I.B. Ayed. *IVD-Net: Intervertebral disc localization and segmentation in MRI with a multi-modal UNet*. in *International Workshop and Challenge on Computational Methods and Clinical Applications for Spine Imaging*. 2018. Springer.
16. Kermi, A., I. Mahmoudi, and M.T. Khadir. *Deep convolutional neural networks using U-Net for automatic brain tumor segmentation in multimodal MRI volumes*. in *International MICCAI Brainlesion Workshop*. 2018. Springer.
17. Zhao, J., M. Mathieu, and Y. LeCun, *Energy-based generative adversarial network*. arXiv preprint arXiv:1609.03126, 2016.
18. You, C., et al., *CT super-resolution GAN constrained by the identical, residual, and cycle learning ensemble (GAN-CIRCLE)*. IEEE transactions on medical imaging, 2019. **39**(1): p. 188-203.
19. Wang, G., et al., *Image reconstruction is a new frontier of machine learning*. IEEE transactions on medical imaging, 2018. **37**(6): p. 1289-1296.
20. Yang, Q., et al., *Low-dose CT image denoising using a generative adversarial network with Wasserstein distance and perceptual loss*. IEEE transactions on medical imaging, 2018. **37**(6): p. 1348-1357.
21. Kingma, D.P. and J. Ba, *Adam: A method for stochastic optimization*. arXiv preprint arXiv:1412.6980, 2014.
22. Sun, J., H. Li, and Z. Xu. *Deep ADMM-Net for compressive sensing MRI*. in *Advances in neural information processing systems*. 2016.
23. Zhu, B., et al., *Image reconstruction by domain-transform manifold learning*. Nature, 2018. **555**(7697): p. 487-492.
24. Wang, G., *A Perspective on Deep Imaging*. IEEE Access, 2016. **4**: p. 8914-8924.
25. Liu, J., A. Lefebvre, and M. Nadar, *Alternating direction of multipliers method for parallel MRI reconstruction*. 2014, Google Patents.
26. Lustig, M., et al., *Compressed sensing MRI*. IEEE signal processing magazine, 2008. **25**(2): p. 72-82.
27. Haldar, J.P., D. Hernando, and Z.-P. Liang, *Compressed-sensing MRI with random encoding*. IEEE transactions on Medical Imaging, 2010. **30**(4): p. 893-903.
28. Shi, W., et al., *On the linear convergence of the ADMM in decentralized consensus optimization*. IEEE Transactions on Signal Processing, 2014. **62**(7): p. 1750-1761.
29. Xu, M., et al., *Limited angle X ray CT Reconstruction using Image Gradient  $\ell_0$  norm with Dictionary Learning*. IEEE Transactions on Radiation and Plasma Medical Sciences, 2020.
30. Ma, S., et al. *An efficient algorithm for compressed MR imaging using total variation and wavelets*. in *2008 IEEE Conference on Computer Vision and Pattern Recognition*. 2008. IEEE.
31. Knoll, F., et al., *Second order total generalized variation (TGV) for MRI*. Magnetic resonance in medicine, 2011. **65**(2): p. 480-491.
32. Knoll, F., et al., *Joint MR-PET reconstruction using a multi-channel image regularizer*. IEEE transactions on medical imaging, 2016. **36**(1): p. 1-16.
33. Yu, H., et al., *Compressive Sensing–Based Interior Tomography: Preliminary Clinical Application*. Journal of computer assisted tomography, 2011. **35**(6): p. 762.

34. Xu, Q., et al., *Low-dose X-ray CT reconstruction via dictionary learning*. IEEE transactions on medical imaging, 2012. **31**(9): p. 1682-1697.
35. Wu, W., et al., *Low-dose spectral CT reconstruction using image gradient  $\ell_0$ -norm and tensor dictionary*. Applied Mathematical Modelling, 2018. **63**: p. 538-557.
36. Candes, E.J., M.B. Wakin, and S.P. Boyd, *Enhancing sparsity by reweighted  $\ell_1$  minimization*. Journal of Fourier analysis and applications, 2008. **14**(5-6): p. 877-905.
37. Ma, J., et al., *Shearlet-based compressed sensing for fast 3D cardiac MR imaging using iterative reweighting*. Physics in Medicine & Biology, 2018. **63**(23): p. 235004.
38. Ma, J. and M. März, *A multilevel based reweighting algorithm with joint regularizers for sparse recovery*. arXiv preprint arXiv:1604.06941, 2016.
39. Yoon, S. and A. Jameson, *Lower-upper symmetric-Gauss-Seidel method for the Euler and Navier-Stokes equations*. AIAA journal, 1988. **26**(9): p. 1025-1026.
40. Block, K.T., M. Uecker, and J. Frahm, *Undersampled radial MRI with multiple coils. Iterative image reconstruction using a total variation constraint*. Magnetic Resonance in Medicine: An Official Journal of the International Society for Magnetic Resonance in Medicine, 2007. **57**(6): p. 1086-1098.
41. Ehrhardt, M.J. and M.M. Betcke, *Multicontrast MRI reconstruction with structure-guided total variation*. SIAM Journal on Imaging Sciences, 2016. **9**(3): p. 1084-1106.
42. Knoll, F., et al., *Parallel imaging with nonlinear reconstruction using variational penalties*. Magnetic resonance in medicine, 2012. **67**(1): p. 34-41.
43. Bredies, K., K. Kunisch, and T. Pock, *Total generalized variation*. SIAM Journal on Imaging Sciences, 2010. **3**(3): p. 492-526.
44. Ravishankar, S. and Y. Bresler, *MR image reconstruction from highly undersampled k-space data by dictionary learning*. IEEE transactions on medical imaging, 2010. **30**(5): p. 1028-1041.
45. Caballero, J., et al., *Dictionary learning and time sparsity for dynamic MR data reconstruction*. IEEE transactions on medical imaging, 2014. **33**(4): p. 979-994.
46. Zhan, Z., et al., *Fast multiclass dictionaries learning with geometrical directions in MRI reconstruction*. IEEE Transactions on biomedical engineering, 2015. **63**(9): p. 1850-1861.
47. Fang, L., et al., *Fast acquisition and reconstruction of optical coherence tomography images via sparse representation*. IEEE transactions on medical imaging, 2013. **32**(11): p. 2034-2049.
48. Esmaeili, M., et al., *Speckle noise reduction in optical coherence tomography using two-dimensional curvelet-based dictionary learning*. Journal of medical signals and sensors, 2017. **7**(2): p. 86.
49. Albarrak, A., F. Coenen, and Y. Zheng, *Volumetric image classification using homogeneous decomposition and dictionary learning: a study using retinal optical coherence tomography for detecting age-related macular degeneration*. Computerized Medical Imaging and Graphics, 2017. **55**: p. 113-123.
50. Fang, L., et al., *Segmentation based sparse reconstruction of optical coherence tomography images*. IEEE transactions on medical imaging, 2016. **36**(2): p. 407-421.
51. Chen, Y., et al., *Artifact suppressed dictionary learning for low-dose CT image processing*. IEEE transactions on medical imaging, 2014. **33**(12): p. 2271-2292.
52. Fang, R., T. Chen, and P.C. Sanelli, *Towards robust deconvolution of low-dose perfusion CT: Sparse perfusion deconvolution using online dictionary learning*. Medical image analysis, 2013. **17**(4): p. 417-428.

53. Tan, S., et al., *Tensor-based dictionary learning for dynamic tomographic reconstruction*. Physics in Medicine & Biology, 2015. **60**(7): p. 2803.
54. Mallat, S.G. and Z. Zhang, *Matching pursuits with time-frequency dictionaries*. IEEE Transactions on signal processing, 1993. **41**(12): p. 3397-3415.
55. Chen, S., S.A. Billings, and W. Luo, *Orthogonal least squares methods and their application to non-linear system identification*. International Journal of control, 1989. **50**(5): p. 1873-1896.
56. Aharon, M., M. Elad, and A. Bruckstein, *K-SVD: An algorithm for designing overcomplete dictionaries for sparse representation*. IEEE Transactions on signal processing, 2006. **54**(11): p. 4311-4322.
57. Zhang, Q. and B. Li. *Discriminative K-SVD for dictionary learning in face recognition*. in *2010 IEEE computer society conference on computer vision and pattern recognition*. 2010. IEEE.
58. Yang, J., et al., *Coupled dictionary training for image super-resolution*. IEEE transactions on image processing, 2012. **21**(8): p. 3467-3478.
59. Mairal, J., et al., *Online learning for matrix factorization and sparse coding*. Journal of Machine Learning Research, 2010. **11**(1).
60. Lu, C., J. Shi, and J. Jia. *Online robust dictionary learning*. in *Proceedings of the IEEE Conference on Computer Vision and Pattern Recognition*. 2013.
61. Wu, W., et al., *Dictionary learning based image-domain material decomposition for spectral CT*. Physics in Medicine & Biology, 2020. **65**(24): p. 245006.
62. Elbakri, I.A. and J.A. Fessler, *Statistical image reconstruction for polyenergetic X-ray computed tomography*. IEEE transactions on medical imaging, 2002. **21**(2): p. 89-99.
63. Zhang, Y., et al., *Tensor-based dictionary learning for spectral CT reconstruction*. IEEE transactions on medical imaging, 2016. **36**(1): p. 142-154.
64. Merlet, S., E. Caruyer, and R. Deriche. *Parametric dictionary learning for modeling EAP and ODF in diffusion MRI*. in *International Conference on Medical Image Computing and Computer-Assisted Intervention*. 2012. Springer.
65. Lei, Y., et al., *Magnetic resonance imaging-based pseudo computed tomography using anatomic signature and joint dictionary learning*. Journal of Medical Imaging, 2018. **5**(3): p. 034001.
66. Lingala, S.G. and M. Jacob, *Blind compressive sensing dynamic MRI*. IEEE transactions on medical imaging, 2013. **32**(6): p. 1132-1145.
67. Liu, J., et al., *3D feature constrained reconstruction for low-dose CT imaging*. IEEE Transactions on Circuits and Systems for Video Technology, 2016. **28**(5): p. 1232-1247.
68. Valkonen, T., K. Bredies, and F. Knoll, *Total generalized variation in diffusion tensor imaging*. SIAM Journal on Imaging Sciences, 2013. **6**(1): p. 487-525.
69. Wang, G., J.C. Ye, and B. De Man, *Deep learning for tomographic image reconstruction*. Nature Machine Intelligence, 2020. **2**(12): p. 737-748.
70. Kurakin, A., I. Goodfellow, and S. Bengio, *Adversarial examples in the physical world*. arXiv preprint arXiv:1607.02533, 2016.
71. Finlayson, S.G., et al., *Adversarial attacks on medical machine learning*. Science, 2019. **363**(6433): p. 1287-1289.
72. Fawzi, A., S.-M. Moosavi-Dezfooli, and P. Frossard, *The robustness of deep networks: A geometrical perspective*. IEEE Signal Processing Magazine, 2017. **34**(6): p. 50-62.
73. Kang, E., J. Min, and J.C. Ye, *A deep convolutional neural network using directional wavelets for*

- low-dose X-ray CT reconstruction*. Medical physics, 2017. **44**(10): p. e360-e375.
74. Wu, D., et al., *Iterative low-dose CT reconstruction with priors trained by artificial neural network*. IEEE transactions on medical imaging, 2017. **36**(12): p. 2479-2486.
  75. Hyun, C.M., et al., *Deep learning for undersampled MRI reconstruction*. Physics in Medicine & Biology, 2018. **63**(13): p. 135007.
  76. He, J., Y. Wang, and J. Ma, *Radon inversion via deep learning*. IEEE Transactions on Medical Imaging, 2020. **39**(6): p. 2076-2087.
  77. Zinkevich, M. *Online convex programming and generalized infinitesimal gradient ascent*. in *Proceedings of the 20th international conference on machine learning (icml-03)*. 2003.
  78. Leung, H. and S. Haykin, *The complex backpropagation algorithm*. IEEE Transactions on signal processing, 1991. **39**(9): p. 2101-2104.
  79. Chauvin, Y. and D.E. Rumelhart, *Backpropagation: theory, architectures, and applications*. 1995: Psychology press.
  80. Ganin, Y. and V. Lempitsky. *Unsupervised domain adaptation by backpropagation*. in *International conference on machine learning*. 2015. PMLR.
  81. LeCun, Y., Y. Bengio, and G. Hinton, *Deep learning*. nature, 2015. **521**(7553): p. 436-444.
  82. Donoho, D.L., *De-noising by soft-thresholding*. IEEE transactions on information theory, 1995. **41**(3): p. 613-627.
  83. Smale, S., *Mathematical problems for the next century*. The mathematical intelligencer, 1998. **20**(2): p. 7-15.
  84. Bastounis, A., A.C. Hansen, and V. Vlacic. *The extended Smale's 9th problem - On computational barriers and paradoxes in estimation, regularisation, computer-assisted proofs and learning*. 2021; Available from: <https://www.mins.ee.ethz.ch/pubs/files/smales9th.pdf>.
  85. Gottschling, N.M., et al., *The troublesome kernel: why deep learning for inverse problems is typically unstable*. arXiv preprint arXiv:2012.01258, 2020.
  86. Antun, V., M.J. Colbrook, and A.C. Hansen, *Can stable and accurate neural networks be computed?--On the barriers of deep learning and Smale's 18th problem*. arXiv preprint arXiv:2101.08286, 2021.
  87. Chen, H., et al., *LEARN: Learned experts' assessment-based reconstruction network for sparse-data CT*. IEEE transactions on medical imaging, 2018. **37**(6): p. 1333-1347.
  88. Genzel, M., J. Macdonald, and M. März, *Solving Inverse Problems With Deep Neural Networks--Robustness Included?* arXiv preprint arXiv:2011.04268, 2020.
  89. Chun, I.Y., et al., *Momentum-Net: Fast and convergent iterative neural network for inverse problems*. IEEE Transactions on Pattern Analysis and Machine Intelligence, 2020.
  90. Schwab, J., S. Antholzer, and M. Haltmeier, *Deep null space learning for inverse problems: convergence analysis and rates*. Inverse Problems, 2019. **35**: p. 025008 (13 pages).
  91. Gilton, D., G. Ongie, and R. Willett, *Deep Equilibrium Architectures for Inverse Problems in Imaging*. <https://arxiv.org/abs/2102.07944>, 2021.
  92. Schlemper, J., et al. *A deep cascade of convolutional neural networks for MR image reconstruction*. in *International conference on information processing in medical imaging*. 2017. Springer.
  93. Hammernik, K., et al., *Learning a variational network for reconstruction of accelerated MRI data*. Magnetic resonance in medicine, 2018. **79**(6): p. 3055-3071.